

N O T I C E

THIS DOCUMENT HAS BEEN REPRODUCED FROM
MICROFICHE. ALTHOUGH IT IS RECOGNIZED THAT
CERTAIN PORTIONS ARE ILLEGIBLE, IT IS BEING RELEASED
IN THE INTEREST OF MAKING AVAILABLE AS MUCH
INFORMATION AS POSSIBLE

NSG-3150

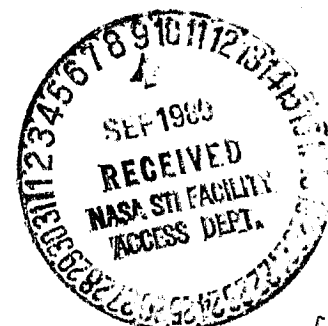
Analysis of Differential and
Active Charging Phenomena on ATS-5 and ATS-6

R. C. Olsen and E. C. Whipple

(NASA-CR-163433) ANALYSIS OF DIFFERENTIAL
AND ACTIVE CHARGING PHENOMENA ON ATS-5 AND
ATS-6 Final Report, May 1977 - Dec. 1979
(California Univ., San Diego, La Jolla.)
154 p HC A08/MF A01

NSG-29-19

UNCLAS
CSCL 23B G3/18 28445



Analysis of Differential and
Active Charging Phenomena on ATS-5 and ATS-6

R. C. Olsen and E. C. Whipple
Center for Astrophysics and Space Sciences - C-011
University of California, San Diego
La Jolla, California 92093

July 1980

Final Report for Period May 1977 - Dec. 1979
Grant NSG-3150

Prepared for
Lewis Research Center
Cleveland, Ohio 44135

TECHNICAL REPORT STANDARD TITLE PAGE

1. Report No. CASS - 80-1	2. Government Accession No.	3. Recipient's Catalog No.	
4. Title and Subtitle Analysis of Differential and Active Charging Phenomena on ATS-5 and ATS-6		5. Report Date July 30, 1980	
		6. Performing Organization Code 410	
7. Author(s) R. C. Olsen and E. C. Whipple, Jr.		8. Performing Organization Report No. UCSD- CASS - 80-1	
9. Performing Organization Name and Address University of California, San Diego La Jolla, California 92093		10. Work Unit No.	
		11. Contract or Grant No. NAS G-3150	
12. Sponsoring Agency Name and Address Lewis Research Center 2100 Brookpark Rd. Cleveland, Ohio 44135 ATTN: Carolyn K. Purvis		13. Type of Report and Period Covered Final, May 1, 1977 to Dec. 30, 1979	
		14. Sponsoring Agency Code	
15. Supplementary Notes			
16. Abstract See page iii.			
17. Key Words (Selected by Author(s)) Spacecraft charging Differential charging Ion engine operation Electron emission		18. Distribution Statement	
19. Security Classif. (of this report) Unclassified	20. Security Classif. (of this page) Unclassified	21. No. of Pages 153	22. Price*

*For sale by the Clearinghouse for Federal Scientific and Technical Information, Springfield, Virginia 22151.

ABSTRACT

The results of NASA Grant NSG-3150 are presented in the following document. This study of spacecraft charging concentrated on the differential charging and artificial particle emission experiments on ATS-5 and ATS-6. It was found that differential charging of spacecraft surfaces generated large electrostatic barriers to spacecraft generated electrons, from photoemission, secondary emission, and thermal emitters. Electron emission experiments on ATS-5 in eclipse charging environments showed that the electron emitter could partially or totally discharge the satellite, but the mainframe recharged negatively in a few 10's of seconds. This latter phenomena was explained as the result of differential charging of the insulating surfaces on the spacecraft, and the creation of an electrostatic barrier by this differential charge. The time dependence of the charging behavior was explained by the relatively large capacitance for differential charging in comparison to the small spacecraft to space capacitance. The large dish antenna on ATS-6 was identified as the source of the electrostatic barrier around the Environmental Measurements Experiment package. One small source of accelerated electrons was identified on the EME package, the University of Minnesota rotating detector. A daylight charging event on ATS-6 was shown to have a charging behavior suggesting the dominance of differential charging on the absolute potential of the mainframe. Ion engine operations and plasma emission experiments on ATS-6 were shown to be an effective means of controlling the spacecraft potential in eclipse and sunlight. Ion fluxes from the neutralizer and engine served to discharge differentially charged surfaces, eliminating barrier effects around the detectors, and improving the quality of the particle data.

TABLE OF CONTENTS

	PAGE
1. INTRODUCTION	1
1. BACKGROUND	1
2. THE ATS-5 AND ATS-6 EXPERIMENTS	3
3. AREAS OF ANALYSIS	3
2. POTENTIAL MODIFICATION BY ELECTRON EMISSION ON ATS-5	5
1. INTRODUCTION	5
2. SATELLITE AND INSTRUMENTATION	5
3. ECLIPSE DATA; 10-16-69	6
4. OPERATIONS OF THE FILAMENT EMITTER	6
5. SUMMARY OF EMITTER OPERATIONS	7
6. CHARGING MODELS	8
1. ONE DIMENSIONAL CURRENT MODEL	8
1. INTRODUCTION	8
2. AMBIENT FLUXES	9
3. SECONDARY YIELDS	10
4. NET CURRENTS IN MAXWELLIAN ENVIRONMENTS	12
5. MODEL CALIBRATION	13
6. RESULTS FOR ELECTRON EMITTER CURRENT MEASUREMENT MODELING	14
2. THREE-DIMENSIONAL, TIME DEPENDENT MODELING	14
1. INTRODUCTION TO NASCAP	15
2. ATS-5 MODEL OBJECT	15
3. POTENTIAL CONTOURS AND BARRIER EXISTENCE	15
4. NASCAP TIME STEPPING	16
7. SUMMARY AND CONCLUSION	17
8. APPENDIX: DETECTOR EFFICIENCY CALIBRATION	18
3. DIFFERENTIAL CHARGING EFFECTS ON ATS-6	20
1. INTRODUCTION AND HISTORY	20
2. SPACECRAFT AND INSTRUMENTS	20
3. DATA-BARRIER EFFECTS	21
1. JULY 17, 1974	21
2. JULY 22, 1974	23
4. DATA SUMMARY	25
5. BARRIER MODELS	25
1. MONOPOLE PLUS DIPOLE MODEL	26
2. NASCAP	27
3. TIME DEVELOPMENT	28
6. DATA-ACCELERATED FLUXES	29
1. SEPTEMBER 5, 1974	29
2. AUGUST 24, 1974	30
7. SUMMARY	32

	PAGE
4. ION ENGINE OPERATIONS	33
1. INTRODUCTION	33
2. ION ENGINE DESCRIPTION	33
3. JULY 18, 1974 - ION ENGINE #2	34
4. OCTOBER 19, 1974 - ION ENGINE #1	36
1. OCTOBER 19 to 23, 1974	39
5. I.E. #2 NEUTRALIZER OPERATIONS	40
1. JULY 20, 1974	40
2. JULY 21, 1974	43
6. ECLIPSE OPERATIONS	44
1. OCTOBER 14, 1976	44
2. SEPTEMBER 3, 1976	34
3. APRIL 7, 1977	36
7. SUMMARY	47
5. BIBLIOGRAPHY	48
6. APPENDIX: WARM IONS AT MIDNIGHT	51
7. FIGURES	55

INTRODUCTION

The purpose of this report is to describe the work that has been done under NASA Grant NSG-3150. The objective of the grant was the analysis of the interaction of spacecraft and artificially injected particles with the aim of understanding active control systems for spacecraft charging. The analysis is concerned with data obtained from experiments performed on the ATS-5 and ATS-6 spacecraft at geosynchronous orbit. A large amount of data have been obtained primarily from the UCSD particle detectors during these experiments, with additional data coming from the ion and electron beam experiments themselves. These experiments were performed under NASA contract #5-23481 supported by Lewis Research Center and the Goddard Space Flight Center. A detailed listing of the data and descriptions of the experiments is available in the final report for that contract, entitled "Active Experiments in Modifying Spacecraft Potential: Results from ATS-5 and ATS-6" (Olsen and Whipple, 1979).

In this introduction we give some of the background for this investigation and provide brief descriptions of the ATS-5 and ATS-6 spacecraft and instrumentation. More detailed descriptions of the experiments are given in the pertinent sections where the experimental results are discussed.

1.0 BACKGROUND

DeForest (1972) was the first to report large (i.e. kilovolt) electrostatic potentials on spacecraft. He found that ATS-5 charged negatively to several kilovolts as the spacecraft entered the earth's shadow during times of magnetic activity when the magnetospheric plasma at geosynchronous altitude was very energetic. DeForest showed that the spacecraft potential could be understood in terms of a current balance to the spacecraft, with the predominant charging current consisting of the energetic plasma electrons. An equilibrium was reached when the plasma electron current was balanced by the incoming plasma ion current and outgoing secondary electrons caused by the primary particle impacts. Large potentials were seen mainly in the earth's shadow because in sunlight photoemission usually provided a sufficiently large flux of outgoing electrons to counteract the effect of the incoming plasma electrons. However, charging was seen to occur in energetic environments even in sunlight, although the magnitude of the potentials are not as large as in the earth's shadow.

At about the same period of time several synchronous satellites experienced spurious switching activity (Lovell et al, 1976). McPherson and Schober (1976) analyzed the dependence of some of these spacecraft anomalies on position of the spacecraft in their orbits and found that there was a marked correlation of the frequency of such anomalies with local time. The dependence was such that the events occurred predomi-

nantly between midnight and dawn in satellite local time. Their investigation included five different satellite systems involving 19 different flights. All the vehicles exhibited some type of behavior which was unexplained but which showed a dependence on geophysical parameters. Reasoner et al (1975) performed a similar analysis of spacecraft charging events on the ATS-6 spacecraft by examining the dependence of charging events on satellite local time. The study was restricted to sunlight charging events during a period of 40 contiguous days from June 15 to July 24, 1974. They found that the occurrence probability was a maximum during the local midnight-to-dawn region and was very similar to the local time distribution of geosynchronous spacecraft anomalies. The inference from these studies was that spacecraft charging was playing an important role in the observed spacecraft anomalies.

The mechanism for the spacecraft anomalies was postulated to be disruption of sensitive electronic circuits by electrostatic discharges. It was realized that insulating materials or isolated conducting materials on the shaded part of a spacecraft would charge differently than materials on the sunlit side so that differential potentials could develop on a spacecraft surface. Large electric fields between adjacent materials could lead to breakdown and discharges. Electron data from the ATS-6 satellite was analyzed to show that there was an electrostatic barrier in the vicinity of the spacecraft (Whipple, 1976a), which was returning photoelectrons and secondary electrons back to the spacecraft even though the spacecraft potential was itself negative. It was argued that the potential barrier was too large to be explained as a space charge effect, and that it was more likely caused by differential charging on the spacecraft surfaces (Whipple, 1976b).

In 1975 a joint research program between the U. S. Air Force and NASA was established to investigate spacecraft charging (Lovell et al, 1975). The overall objective of the investigation was to provide the design criteria, techniques and test methods to ensure control of absolute and differential charging of spacecraft surfaces. The accomplishment of this objective was to involve the following elements:

1. Definition and modeling of the environment.
2. Establishment of ground facilities for simulation of charging processes and development of test techniques.
3. Development of an analytical charging model of a spacecraft.
4. Development of new and modified surface materials for spacecraft.
5. Evaluation of active control techniques for minimizing spacecraft surface charging.
6. Carrying out flight experiments, particularly the SCATHA spacecraft.
7. Development of design criteria and test specifications.

The work described in this report falls under item 5: the evaluation of active control techniques for minimizing spacecraft surface charging.

2.0 THE ATS-5 AND ATS-6 EXPERIMENTS

The ATS-5 spacecraft was launched into a geosynchronous orbit in August, 1969 and has been stationed near 105 west longitude since September, 1969. The satellite spins with a period of 0.79 seconds. The spin axis is parallel to the earth's rotation axis. The spacecraft is cylindrical in shape with a length and diameter of about 1 meter (see Figure 1). It has no extended booms or other appendages. It carries two small cesium thruster ion engines with filament neutralizers. The discharge experiments were carried out primarily with the neutralizers since the accidental spinup of the satellite made ordinary operation of the thrusters difficult. However, two thruster operations were performed, once in 1972 and once in 1973. In a brief non-neutralized operation of the thruster the spacecraft charged to the thruster accelerating potential of 3 keV (Whipple and Olsen, 1979). Experiments with the ATS-5 neutralizers were conducted during the eclipse seasons beginning in the fall of 1974, and extending through the spring eclipse season of 1978. There were a total of about 200 such days when experiments were conducted and data obtained.

In contrast to ATS-5, ATS-6 is a large multi-purpose satellite with extended solar array panels and a large parabolic transmitting antenna. It was launched in May 1974 into geosynchronous orbit. The spacecraft is three-axis stabilized (see Figure 20.). The ATS-6 satellite also carried two cesium ion thrusters, with the difference that the neutralizers on ATS-6 were small plasma emitters which discharged a low energy (1 to 10 eV) cesium plasma. Ion engine operations were performed on July 18, 1974 and during the period from October 19 to 23, 1974. Both ion engines failed in that they proved impossible to restart after their first operation. However, the neutralizers were still usable and a total of about 20 experiments were carried out, again primarily in the eclipse seasons, in 1976 and 1977. A complete list of the data obtained from both the ATS-5 and ATS-6 experiments is given in the report by Olsen and Whipple (1979).

3.0 AREAS OF ANALYSIS

The analysis performed on the ATS data set was divided into three sections:

1. Electron emission experiments on ATS-5.

2. Differential charging effects on ATS-6.

3. Ion engine and plasma emission experiments on ATS-6

Each topic is treated independently, though the ATS-6 ion engine analysis depends heavily on the results of the differential charging analysis. These sections are followed by a summary of the grant results, and an appendix with results from a study of the thermal ion population in the midnight sector. This last study was necessary to separate cesium fluxes (from the ion engine) and ambient ion fluxes in the particle data.

POTENTIAL MODIFICATION BY ELECTRON EMISSION ON ATS-5

1.0 INTRODUCTION

Data from the ATS-5 satellite showed the existence of large electrostatic potentials on satellites at geosynchronous altitude. DeForest (1972) both demonstrated the existence of high spacecraft charging and provided a one-dimensional current balance model to explain the phenomenon. In 1974, a program of operations was begun to study means of modifying spacecraft potentials. The filament neutralizers from the ion engines were used to emit thermal electrons in attempts to discharge ATS-5 in eclipse periods.

The program had mixed results. The large potentials were usually reduced in size, but the spacecraft was rarely totally discharged in this manner. Modeling of these operations was done with one-dimensional current balance models and the more sophisticated NASCAP program. It was found that the neutralizer filament emission was limited by a potential barrier developed by differential charging on the spacecraft surface.

This section repeats some of DeForest's results on absolute potential measurements and one dimensional current models (1972, 1973), shows data from three neutralizer operations, and gives models and analysis used to interpret the data.

2.0 SATELLITE AND INSTRUMENTATION

ATS-5 was launched into synchronous orbit on August 12, 1969. Its final orbit was at 105 W longitude, with a spin rate of about 100 rpm about a spin axis nominally parallel to the earth's axis. The spacecraft, illustrated in Figure 1, was cylindrical, with an exterior dominated by solar arrays. Cavities at the top and bottom contained a mixed assortment of insulators and conductors. The fiberglass belly band was the location of the majority of the instruments and experiments. These provided the majority of the conducting area on the spacecraft.

The UCSD plasma detectors were electrostatic analyzers for electrons and ions from 50 eV to 50 keV in 62 exponential steps, and had 12 % energy resolution. One energy scan requires approximately 20 seconds. One pair of detectors was aligned to the spin axis (nominally parallel to the magnetic field), with the other pair perpendicular to the spin axis and the magnetic field.

The ion engines were small cesium thrusters with filament neutralizers. The engines were only operated briefly, due to the spinup of the

spacecraft, but the filaments were unaffected by the spinup. The filaments, illustrated in Figure 2, can be seen to be near the outer edge of the thruster. A voltage drop of a few volts across the filament provided a small range of emitted energies in the eV region.

3.0 ECLIPSE DATA ; 10-16-69

A typical eclipse charging event is presented in Figure 3. Figure 3 shows the particle data in spectrogram form for October 16, 1969. Twenty four hours of data are shown for the perpendicular detector. The eclipse is between 06:20 and 07:20, and the spacecraft charges to -4200 V. Eclipse potentials fell between extremes of 0 and -10 kV, and this eclipse is typical of the average eclipse in an energetic environment.

In 1974, data from the ATS-6 satellite presented similar results. Stationed at 94 W longitude, the newer satellite encountered almost the same environment as ATS-5. Potential measurements made in eclipse on the two satellites were remarkably close when the environment was constant over that distance. Because of this, it was possible to use ATS-6 data during operations of the ATS-5 filaments as a control for comparison purposes.

4.0 OPERATIONS OF THE FILAMENT EMITTER

Data from a neutralizer operation on September 20, 1974 are presented in Figures 4 to 6. The ATS-5 data are presented in a two hour spectrogram covering the eclipse period, in Figure 4, the ATS-6 data in Figure 5. Figure 6 gives the potentials on both satellites during the operation. The spectrograms show an energetic but relatively constant environment in the midnight region. Strong electron fluxes are visible up to 20 keV. The large spacecraft potentials in eclipse are again shown by the absence of ions below the large charging peak. The ATS-6 potential wanders between -1 and -4 kV, as does the ATS-5 potential when the neutralizer is off. The ATS-5 eclipse period ran from 06:23 to 07:30, and ATS-6 was eclipsed from 05:37 to 06:42. The ATS-5 spectrogram shows the abrupt rise in potential caused by the neutralizer operation from 06:31:25 to 06:35:25. A later operation, from 07:05 to 07:09 also shows an abrupt rise in potential during the neutralizer operation, with variations in potential during the operation. Figure 6 presents a more detailed look at the first operation of the day. The potentials of the two spacecraft were determined by using the cutoff in the ion data due to the acceleration of low energy ions up to the spacecraft potential. The values would be subject to about +5% error due to the energy window width for an ideal detector. A missing data point, as is occasionally encountered on ATS-5, will result in a value which is about 10 to 20% too negative. ATS-5 responds immediately to the neu-

tralizer 'on' command, rising to near zero potential between two data points. There is a smooth drop in the potential following the initial discharge peak. The neutralizer 'off' command is followed by an immediate drop in potential to the equilibrium eclipse value.

Similar behavior is seen in Figure 7, where data from September 30, 1974 are presented. Again, the rapid discharge, and then recharging of the satellite is apparent. The variation in the charging rate after the initial discharge spike is again a common feature. The neutralizer is operated from 06:34:20 to 06:38:20. Initially, from 6:35 to 6:36, the potential changes by 450 volts. By 6:37, the rate of change is only 100 volts a minute. The question this raises is: will the spacecraft potential reach an equilibrium in a longer operation?

As longer operations were attempted, it was found that the charging rate slowed to near zero after several minutes. However, another time dependent effect became apparent. In some operations, there was a short but noticeable undershoot in the potential when the neutralizer was turned off; i.e. the potential became more negative than the normal equilibrium potential in eclipse would have been.

This effect can be seen in the data from March 28, 1978 in Figure 8. The dip visible at 04:41 is one of the most pronounced such events. Typically, the dip would only last through one or two energy scans, i.e. twenty to forty seconds. This dip in potential was at first thought to be an anomaly in the data, but repeated appearance of the phenomenon convinced us of its reality.

5.0 SUMMARY OF EMITTER OPERATIONS

Data from three of the 194 days of operations have been shown. The commonly seen features are the sharp rise in potential at the neutralizer "on" command, occasionally to above the -50 V limit of the particle data. This was followed by a rapid drop in spacecraft potential, a drop which slowed as the potential seemed to approach a new equilibrium. It was found that whenever the spacecraft had charged negatively in eclipse, operation of the filament could partially discharge the spacecraft, but the neutralizer was most effective at low or moderate potentials. Figure 9 shows the results of a comparison of the spacecraft potential with the neutralizer off, and then the equilibrium value with the neutralizer on for 70 cases. Black spots indicate multiple measurements at a given pair of potentials. Potentials for neutralizer off were taken as an average around the operation time, and potentials for neutralizer on were taken after the neutralizer had been on for 1 or 2 minutes. The neutralizer consistently causes the spacecraft to discharge, with relatively greater effects at lower equilibrium eclipse potentials.

6.0 CHARGING MODELS

The objective of our analysis of these events was to determine the currents necessary to discharge the satellite. This required us to model the equilibrium current balance to the spacecraft, in order to estimate the portions of the current balance that we could not directly measure. Once it became clear that there were time dependences in the data, a second goal was to understand the physical processes causing these variations. The first model to be developed is an extension of the one dimensional current balance model developed by DeForest (1972). This model is an equilibrium model, and does not attempt to describe time dependent changes. These latter effects were studied with NASCAP, a three dimensional, time dependent, charging analysis program.

6.1 ONE DIMENSIONAL CURRENT MODEL

6.1.1 INTRODUCTION -

A one dimensional current balance model was developed to model the equilibrium currents to the spacecraft. This was done in order to estimate the current emitted by the hot filament. The work followed the patterns established by Whipple (1965) and DeForest (1972). The UCSD detectors measure the ambient fluxes which reach the spacecraft. These fluxes can then be used to calculate the secondary electron fluxes caused by the ambient fluxes, and the net current to the spacecraft can then be found.

The important secondary emission processes are backscattering, true secondary emission, and secondary emission due to ion impact. Since the spacecraft materials were not well characterized for their secondary emission characteristics, nominal values for aluminum were used. When the ambient fluxes are summed with the secondary electron fluxes the following equation results:

$$\int dA [F_i - F_e + F_{sec} + F_{other}] = 0$$

The requirement that the fluxes sum to zero is an equilibrium requirement. A non-zero sum would be a net charging current to the spacecraft. Application of this equation required repeating the earlier work of DeForest, and extending that work by determining the amount of degradation in the spiraltron detectors as of 1974.

6.1.2 AMBIENT FLUXES

The ATS-5 detector measures the ambient fluxes from 50 eV to 50 keV. In the environments studied, this energy range provides the bulk of the current to the spacecraft from the ambient plasma. The ambient flux normal to the spacecraft surface at any time was obtained by summing over the energy channels. It was assumed that the environment was isotropic, and the total flux to the spacecraft was thus obtained.

6.1.3 SECONDARY YIELDS -

The modeling of the secondary emission processes followed the work of Whipple(1965) and Systems, Science and Software(S**3) (Mandell, et. al., 1978). The pertinent terms are 'true' secondaries, backscattering, and secondaries due to protons (or ions, abbreviated occasionally as SCDP). True secondaries are separated from backscattered particles by their emitted energy, with a breakpoint set at 50 ev. For the model to be generally applicable, we need to have general expressions for each of the scattering terms. These are described below.

A general form for true secondaries (not including backscatter) is attributed to Sternglass (1950).¹

where

$$Y = 7.4 * \delta_{\max} * (E / E_{\max}) * \exp(-2. * (E / E_{\max})^{.5})$$

E_{\max} = the energy where Y has its maximum

δ_{\max} = the secondary yield at E_{\max} .

The parameters for secondary emission from materials, which may be considered as surface or sensor materials on a satellite, are given in Table 2.

The yield curve for a typical case of $E_{\max}=400$ eV and $\delta_{\max}=1$ are shown in Figure 10, plotted against the ATS-5 detector channel number and energy. There is a distinct peak in the yield, in an energy range well covered by the UCSD detector.

¹ This formula may actually be in Sternglass, E. J., Westinghouse Research Lab, Scientific Paper No. 1772 (1954). The oldest references are Knott, 1972; and Grard, 1973.

MATERIAL	SECONDARY EMISSION PROPERTIES	
	E _{max}	max
Gold	800 eV	1.45
Aluminum	300 eV	0.97
Aluminum w/Oxide	300 eV	2.60
SiO ₂	420 eV	2.50
Aquadag	350 eV	0.75
BeCu	300 eV	2.20
BeCu activated	400 eV	5.00

Table 1. Secondary Emission Properties of Various Materials
(Gibbons, 1966 and Hachenberg et al. 1959)

A useful form for backscattering has been developed by S**3 for their NASCAP program(Katz, et.al., 1977). It is

$$Y = .1 * (1. - .05/E) * (\beta + \text{EXP}(-E / 5.))$$

for E > 50 eV

$$Y = 0 \quad \text{for} \quad E < 50 \text{ eV}$$

E in keV

$$\beta = 10 * (1 - (\frac{2}{e}) *.037 * Z)$$

Z = atomic number of element

Secondary electrons due to ions are well fitted by

$$Y(E) = \begin{cases} .05 & E < 1 \text{ keV} \\ 1.36 * (E)^{**.5} / (1 + E/40.) & E > 1 \text{ keV} \end{cases}$$

E in keV

This form is also from the S**3 work.

These yields are plotted versus the ATS-5 channel number in Figures 11 and 12. This is a log energy scale, and again shows how the coefficients vary over the region of interest (50 eV to 50 keV). Since the

average atomic number for SiO₂ is 10, this value was chosen to plug into the backscattering constant. Increasing the atomic number (say to 13 for aluminum) would merely add a small constant value to the backscattering coefficient. The ion term is material independent. We see the backscatter yield is low below 1 keV, and mildly varying thereafter. The relative flatness of the curve shows that the backscatter yield will be relatively independent of the ambient electron temperature, so long as it is over a keV. The secondaries due to ions yield is quite low at low energies, but increases rapidly in the 10 keV region. This higher yield can be quite important in multiplying the effect of the high energy ion fluxes seen in substorms.

The plots shown are for normal incidence. The angular dependence of secondary production is not well known for any of these processes, especially at grazing incidence. Fortunately the $\cos(\theta)$ term in the scattering integral reduces the effect of this ignorance.

Secondary electrons due to protons are thought to go as $\sec(\theta)$ Ref. Sternglass, 1957, Phys. Rev., vol. 108, p 1; Allen, 1939, Phys. Rev, vol. 55 p. 336; Aarsett, 1954, Journal of Applied Physics, vol 25, p. 1365.

True secondaries go as either $\sec(\theta)$, or $\sqrt{\sec(\theta)}$ according to a review by Gibbons (1966). The latter dependence was chosen as a slightly better fit.

Backscattering is modeled by Darlington and Cosslett (1972) J. Phys. D: Appl. Phys, Vol 5, p.1969-1951. The angular dependence is roughly given by $\sec(\theta)$ (by interpretation of Figure 3 in Darlington and Cosslett).

If the $\sec(\theta)$ dependences are assumed, it is easy to average the yield functions over angle. Assuming the plasma is isotropic, we have:

$$YIELD = \iiint d^3v Y(E, \theta) v \cos(\theta) f(v)$$

$$YIELD = \iint d\Omega \cos(\theta) \int dv v^3 f Y(E, \theta)$$

if $Y(E, \theta) = A(E) * B(\theta)$, then

$$YIELD = \iint d\Omega B(\theta) \cos(\theta) \int dv v^2 f(v) A(E)$$

We define the integral

$$I = \iint d\Omega B(\theta) \cos(\theta)$$

For the three possible theta dependences mentioned above, we find:

$$I = \begin{cases} \pi & B(\theta) = 1 \\ \frac{4}{3} \pi & B(\theta) = \sqrt{\sec(\theta)} \\ 2 \pi & B(\theta) = \sec(\theta) \end{cases}$$

We see that the main effect of these angular dependences is to increase the effective secondary coefficient, and can optionally include the factor in our yield calculations.

Calculation of the secondary flux for ATS-5 distribution functions was a matter of converting the integral to a sum over the 62 energy channels in the 50 eV to 50 keV range.

6.1.4 NET CURRENTS IN MAXWELLIAN ENVIRONMENTS -

The net current density to a spacecraft was studied for Maxwellian environments in order to obtain a qualitative understanding of the relationships of the different currents to the environment and each other.

As part of this study, the yield for each secondary production term was studied as a function of the electron temperature. The term which was most interesting was the true secondary term, which has the largest variation in yield as a function of energy. The integral yield

$$I = \iiint d^3v \, f(\vec{v}) \, Y(v) \, \vec{v} \cdot \hat{n} / \iiint d^3v \, f(\vec{v}) \, \vec{v} \cdot \hat{n}$$

is plotted for true secondaries in Figure 13. The dominant feature in the plot is the peak at low energies, reaching almost 0.9 in this case. The true secondary characteristics used here are those for a material with a maximum yield of 1 at an energy of 400 eV. This is a low yield compared to several in Table 1. Even with a low maximum yield, the integrated yield approaches the ambient electron flux at low temperatures. This shows that for low temperature environments and surface materials with large secondary yields, the emitted secondary flux will exceed the ambient electron flux. The spacecraft will generally charge positively in response to the situation, and the secondary emission will be limited.

Similar calculations for backscattering showed the same integral to be roughly constant once the ambient temperature reached 1 keV.

If we take a surface in an isotropic Maxwellian plasma, and sum the ambient and secondary currents, we obtain the net current density to the surface as a function of the spacecraft potential (see Figure 14). The surface properties in this example are those of a material with atomic number 10, and a maximum true secondary yield of 1.5 at 400 eV. These characteristics are similar to aluminum or silicon dioxide. The $\sec(\theta)$ angular dependence for secondary production was included and averaged over in this case. The ambient particle density is $1/\text{cm}^3$, with an ion temperature of 5 keV. The electron temperature varies from 2 to 10 keV. In the absence of additional currents, such as photoemission or artificially generated currents, the equilibrium potential of our fictitious spacecraft would be found by locating the intercept of the appropriate curve with the current=0 axis. For the coolest plasma shown here ($T_e = 2$ keV), the equilibrium potential is positive, and the curve

does not reach zero current on this plot. The higher energy curves show equilibrium potentials between -2 and -7 kV.

6.1.5 MODEL CALIBRATION -

The lack of information on the actual surface materials of the ATS-5 satellite required us to vary the secondary yield parameters to obtain a balance of currents to the spacecraft in equilibrium conditions. This was done by assuming that the yield coefficients for aluminum were close to correct, at least in their functional forms, and adding an undetermined coefficient to the yield term. This results in the following equation:

$$\text{NET FLUX} = F_{\text{ion}} - F_{\text{electron}} + a * F_{\text{true}} + b * F_{\text{backscatter}} + c * \text{scdp}$$

where F_{ion} = ambient ion flux
 F_{electron} = ambient electron flux
 F_{true} = true secondary flux
 $F_{\text{backscatter}}$ = backscatter secondary flux
 F_{scdp} = secondary electrons due to protons

and each term is obtained by summing over the observed energy range.

The different flux terms were calculated over a range of environments for the eclipsed spacecraft in the first year of operation (1969 to 1970). If the coefficients a, b, c were 1, the net flux obtained in each case would be zero. The coefficients were varied about 1 to bring the net flux to zero. In practice, this was initially done by looking at the RMS error defined by the sum of the squares of the net flux divided by the ambient electron flux (to normalize).

Variation of the parameters showed a problem. The parameter b, the backscatter yield, increased until the backscatter yield equaled the ambient electron flux, and the a and c parameters dropped to zero. It was realized that this was due to the relative flatness of the backscatter yield curve, and thus the close proportionality of the backscatter yield to ambient electron flux. The electron flux is about 10 times the ambient ion flux in the average eclipse case, and the fit could obtain less than 10 % RMS error in the above manner. Because of this problem, the b parameter was set so that the the average backscatter flux was 40 % of the ambient electron flux, which results in b=1.5. Proceeding with a fit, we found a=.7 and c=.5 when using the angular average over the sec(theta) dependences of the yield.

6.1.6 RESULTS FOR ELECTRON EMITTER CURRENT MEASUREMENT MODELING -

The current balance calculation has relatively large errors in it, and the calibration set from 1969-1970 gave an RMS error of 12 %. Detector degradation causes an additional uncertainty of about 50% in the electron flux, and about 10% in the ion flux. (see appendix)

The current balance model was applied to the ATS-5 electron emitter operations. The net fluxes are now a measure of the current emitted by the hot filament. Conversion from flux to current requires integration of the flux over the area of the spacecraft. The question of which surface area to use becomes apparent at this time. The current balance the neutralizer is involved in is the balance to the mainframe of the spacecraft. The conducting area of the spacecraft is therefore the area to use in the integration. The cylindrical spacecraft has the dimensions: length = 184 cm, diameter = 146 cm, for an area of 12 m^2 , neglecting the interior walls of the cavities. The conducting area is not accurately known, but is about one tenth of the total area.

Net fluxes of 30 picoamps/cm² were obtained from the equilibrium data, with maximum values of 60 picomaps/cm² obtained at the discharge peak. This gives an equilibrium current of .3 microamps, assuming a conducting area of 1 m^2 . The equilibrium current of .3 microamps was substantially below the capabilities of the emitter (nominally milliamps). This fact, coupled with the peculiar time dependence of the potentials, lead to a consideration of how the current might be limited.

Space charge effects were considered, but they could not explain the observed time dependences. Most reasonable spacecharge limiting processes would occur much more rapidly than the effects seen on ATS-5.

The solution was found to involve differential charging of the spacecraft surfaces. Because the majority of the spacecraft surface is insulating, it is able to hold a potential substantially different from the spacecraft mainframe. We will show below that such potentials can limit the neutralizer current. Finally, because of the difference in magnitudes of the spacecraft to plasma capacitance (picofarads) and solar array to mainframe capacitance (microfarads), the two time constants observed in the data are explainable as the time constants of the two capacitances. This will be seen in the time dependent model below.

6.2 THREE-DIMENSIONAL, TIME DEPENDENT MODELING

The twin problems of a limiting process and time dependence require a code which can calculate fluxes to a three dimensional object, and do so for the time dependent case of switching on and off an artificial current. The three dimensional analysis is required to obtain the electrostatic barrier generated by an uneven distribution of surface potentials.

6.2.1 INTRODUCTION TO NASCAP -

The NASCAP (NASA Charging Analyzer Program) code was developed for the solution of equilibrium and time dynamic charging problems in magnetospheric environments by Systems, Science and Software (Mandell, et.al., 1978).

Objects are modeled on a 16 by 16 by 33 grid, with up to 15 different materials. The internal capacitances of the spacecraft are defined and calculated, and the capacitance of the spacecraft to the distant plasma. Space charge effects are left out, and Laplace's equation is used to determine the potentials in space around the object. Given an initial potential distribution on the spacecraft, the fluxes to the spacecraft are calculated based on a specified environment. A one-dimensional (spherical) approximation is used to calculate the flux to each surface. Secondary fluxes emitted from those surfaces are calculated based on the ambient fluxes. The effects of local electric fields on these emitted currents, i.e. barrier effects, are included, and can limit the emitted secondary electron flux. Barrier effects are also checked in the photoemission flux calculation. The code then works in cycles, calculating the change in potentials and fields caused by the current flow, then the new currents in the new electric field distribution. The accuracy of the code is largely a question of how accurately the material properties are known.

6.2.2 ATS-5 MODEL OBJECT -

The ATS-5 satellite was modeled as shown in Figure 15, filling most of the first grid. The object is embedded in a larger grid which is twice the size of the inner grid. In the ATS-5 object shown in Figure 15, small conducting areas are surrounded by insulators.

The secondary emission properties of all surfaces are those of aluminum, a concession to our lack of knowledge of ATS-5 surface properties. The insulators and conductors differed only in their resistivity in the model object.

6.2.3 POTENTIAL CONTOURS AND BARRIER EXISTENCE -

In the initial computer runs, we simply established potential distributions on the spacecraft to study the resulting fields. The objective was to establish an electrostatic barrier to electron emission. It was found that almost any non-uniform potential distribution did so! Figure 16 shows the results for a spacecraft at -50 volts, with insulators at -70 V. The potential contours are given in the plane perpendicular to the spacecraft axis, midway along the axis. These conditions generated a saddle point at -53 V in front of the conducting surfaces, which results in a barrier of 3 V to electrons. Electrons emitted from the conducting spacecraft surfaces with less than 3 eV kinetic energy

will be returned to the surface. This demonstrated that differential charging of the spacecraft could quickly lead to a limitation of the current emitted by the hot filament.

6.2.4 NASCAP TIME STEPPING -

The final stage of the modeling was to attempt to duplicate the time dependence of the data. The electron emitter was modeled as a 10 microamp source of photoelectrons, which the computer object emits with a thermal energy of 2 eV. Surfaces were given the secondary emission properties of aluminum. The model spacecraft had a capacitance to the distant plasma of 104 picofarads, and a much larger capacitance to the solar array of 1.3 microfarads. Thus the capacitance governing differential charging was 10,000 times larger than the capacitance corresponding to the mainframe to plasma potential difference. Given that the net current to the spacecraft at any time is roughly proportional to the potential of the spacecraft, an effective resistance can be invoked. When combined with the system capacitance, this gives an effect time constant for the time dependent effects seen. The large difference in capacitances implies the time constants for charging and differential charging will show a substantial difference.

The results for a 10 keV Maxwellian environment are shown in Figures 17 and 18. The first case is a single Maxwellian population, the second the sum of a 100 eV and 10 keV Maxwellian. The different populations were considered because of the energy dependent variation in secondary yield. The noteworthy points here are not the magnitudes of the voltages, but rather the relative shapes of the curves. At time zero the spacecraft is allowed to charge negatively to equilibrium. At 2 minutes, the emitter is started. The spacecraft discharges promptly (milliseconds). Until this time, no differential potentials had developed. The solar array now begins to charge negatively again, limited by the capacitance of the solar arrays to the spacecraft mainframe. Within 10 seconds, the solar array is 10 V negative with respect to the spacecraft, and a barrier is forming. Once a barrier has formed, the spacecraft potential drops back in the direction of its equilibrium eclipse value. The differential potential and barrier height stabilize, and the drop in potential slows. At emitter off, the potential promptly drops to the equilibrium value it had before the operation. This time development is identical to that seen in the actual operations. The different particle populations give slightly different potentials, but the same time dependences and curve shapes are seen.

The negative overshoot at emitter off was seen in a few of the model runs, but was not always seen. It seems to depend upon the environment. The overshoot can be understood as part of this model. At the time the neutralizer is switched off, there is a differential potential on the spacecraft which is generating a barrier to low energy electrons. There is no fundamental difference between the filament electrons and those generated by true secondary emission. If the environment is such that the true secondaries are an important part of the current balance,

a barrier around the conductors will seriously affect the current balance to the spacecraft even after the emitter is switched off. It can be seen in the figure that for this case, the differential potential has a time constant of about one minute for decaying. This time constant depends on the inter-spacecraft capacitances, which are poorly determined. More accurate knowledge of the spacecraft structure, used in the right environment, should yield quantitative as well as qualitative agreement with actual operations.

7.0 SUMMARY AND CONCLUSIONS

The electron emitter on ATS-5 was operated over a hundred times over a 4 year period. These operations succeeded in reducing the magnitude of the potentials on the satellite, but rarely discharged the spacecraft completely. Transient negative potentials of greater size than the eclipse equilibrium value were seen when the neutralizer was switched off. Modeling of the current balance to the spacecraft showed that less than 1 % of the emitted current was escaping the spacecraft at equilibrium. Three dimensional modeling of the potentials and currents with NASCAP showed the development of differential potentials was the cause. The operation of the emitter caused differential potentials of on the order of a hundred volts to be developed on the spacecraft surfaces, limiting the emission of the filament. This limitation was sufficient to explain the equilibrium potentials seen, and would apply to most spacecraft with insulating surfaces. The NASCAP computer code was shown to be an effective tool in the modeling of three dimensional charging problems, providing both the model of the limitation mechanism, and the model for the time development of the observed effects.

APPENDIX: DETECTOR EFFICIENCY CALIBRATION

The emitter operations we wished to study began in the fall of 1974, some 5 years after launch. Over this period of time the detector (spiraltron) efficiencies dropped considerably. A major piece of work was to recalibrate the detector efficiencies.

We examined some eighty days of data spread over the five years of instrument operation preceding the 1974 neutralizer operations. A spectral average was taken over each day, typically including 24 hours of data. The assumption is that this will smooth out any transient phenomena, and give the detector response to an average particle population.

Over a range of high and low activity, the slower variations in the environment should average out. Assuming there are no long term variations (i.e. over the 5 year period) in the density and temperature of the environment, we then have the detector's response to an average plasma over 5 years. There are annual variations in the average flux seen by the detectors. This is caused by the seasonal variation in latitude, and was partly suppressed by taking data primarily from the fall seasons.

In practice, the count rate in each of the 64 channels of the 4 detectors was averaged over one hour. Obviously bad data points were removed, occasionally entire hours were deleted. The one hour averages were in turn averaged for each day. Comparison of the 24 hour spectral averages showed little change in the relative efficiency as a function of energy. (ATS-6 did show such relative changes, particularly in the low energy ions) Taking the relative efficiency as a constant, the averaged count rate can then be summed over the channels. This reduced the detector efficiency to a single number, which was plotted and printed out. Normalization is made to the first months of operation to obtain the efficiencies.

For the plots seen in Figure 19, a further average was made over periods of 5 to 7 days. The data points are the means, the error bars \pm one standard deviation. The starred data points represent data from days 3869 and 4009. These were the only data available for 1973, and are included only as indicators of the decay. We see that the two ion detectors (channels 2 4) have remained close to their initial efficiencies over the 5 year period, while the electron detector efficiencies have dropped by two orders of magnitude. This is because the ion detectors have measured 10 to 100 times fewer counts than the electron detectors, and will take correspondingly longer to decay. (The decay in efficiency is generally correlated with the number of particles counted). The differences in the two electron detectors are presumably due to some initial differences in the channeltrons in manufacture, or in subsequent pre-launch handling, as well as the difference in fluxes measured over the instrument history. There will be differences in the flux measured due to the angles the detectors make with the magnetic field. On the average, detectors 3 & 4 (called the parallel detectors) will look mainly along the magnetic field line, while detectors 1 & 2 look perpendicular to it.

Efficiency corrections used for the 1974 data were:

EPSILON(1) = 300.
EPSILON(2) = 2.5
EPSILON(3) = 75.
EPSILON(4) = 1.8

>

DIFFERENTIAL CHARGING EFFECTS ON ATS-6

1.0 INTRODUCTION AND HISTORY

Shortly after data started returning from ATS-6, it became clear that large fluxes of electrons were being returned to the UCSD detector from the spacecraft surface. Work by Whipple (1976 a,b) established that there was an electrostatic barrier returning secondary electrons and photoelectrons to the detectors. This barrier was shown not to be due to electron space charge effects, and it was postulated that the barrier was due to differential charging of spacecraft surfaces.

The EME package on ATS-6 was almost entirely conducting, but large portions of the spacecraft surface were covered with insulators. In the work done to determine possible sources of the differential charging barrier, a number of possible surfaces were considered until the large dish antenna was shown to be capable of producing the observed barrier.

One other effect was studied in detail, the observation of intense fluxes of accelerated electrons near the energy of the differential charging barrier. One source of these particles was determined to be the University of Minnesota energetic particle detector, a small cube coated with an insulating white paint, located inside the barrier region, on the EME box.

The purpose of these studies was to provide the background of information necessary to understand the ion engine and plasma bridge neutralizer operations on ATS-6. One of the major effects of such operations is to cause a reduction of differential charging effects around the EME box, and it was necessary to understand the causes of the charging before we could study its elimination.

2.0 SPACECRAFT AND INSTRUMENTS

ATS-6 was a large spacecraft, with major dimensions on the order of 10 meters as illustrated in Figure 20. It can be seen that the dominant features are the large dish antenna, the solar arrays extending out above the antenna, the Earth Viewing Module (EVM) below the antenna, and the smaller Environmental Measurements Experiment (EME) package above the antenna.

The UCSD detectors are located on the EME package, as shown in the photograph in Figure 21. The detectors are differential in energy, angle, and time, covering the 1 ev to 80 keV energy range in 64 exponential steps in sixteen seconds. The energy bandwidth is 20 % of the selected energy, and the angular width is 2 by 5 degrees. The two rotating heads sweep through a 220 degree range, with angles defined in Figure 22. The north-south head rotates in a plane through the spacecraft and the earth's axis, while the east-west head rotates in a plane perpendicular to the earth's axis. (Mauk and McIlwain, 1975) In the midnight region, where differential charging effects are most prevalent, the EVM and antenna are aimed at the earth, and the EME package is pointed away from the earth and the sun, and the top of the package is in shadow.

The dish antenna is a complicated and important portion of the spacecraft structure. The antenna was composed of a dacron mesh, flashed with copper to create a conductor, then coated with silicon to aid deployment and maintain thermal control. The antenna was folded at launch, and its successful deployment was one of the early achievements by a remarkable satellite.

The EVM carried the spacecraft systems, communication equipment, and the engineering experiments. It's surface was largely covered with a thermal blanket, with the insulating kapton surface facing outwards. Substantial differential charging undoubtedly occurs on the EVM, and the spacecraft potential is probably largely determined by the EVM.

3.0 DATA-BARRIER EFFECTS

3.1 JULY 17, 1974

A good example of the observations of trapped electrons is shown in spectrograms in Figures 23 and 24. The data from the north-south and east-west heads are shown for a two hour period, shortly after local midnight. Both detectors are rotating, with the angular position reflected in the diagonal traces at the tops of the spectrograms. The trace above the north-south spectrogram is the pitch angle of the particles seen by the detector, which indirectly shows the rotation of the detector, while the trace over the east-west spectrogram is the detector angle. The count rates are plotted with a grey scale, with black being

zero count rate, and white a maximum. The grey scale has an overflow provision for times when the count rate exceeds a maximum value, as is seen in the 40 eV ions between 08:00 and 08:05 in the north-south data. The major features to be noted are the absolute spacecraft potential, which accelerates the ambient low energy ions into the spacecraft at the spacecraft potential energy, and the high electron fluxes at energies which mirror the potential. The potential is seen by the absence of ions below an energy ranging from 20 to 50 eV between 07:20 and 09:00. The differential charging signature is the bright white band of low energy electrons over the same time period, reaching a maximum of 50 to 100 eV in the middle of the time period. The diagonal pattern along the barrier edge reflects the angular scanning pattern of the detector heads.

Other common features that are seen in the spectrograms are the intense high energy electron fluxes seen between 1 and 20 keV, which are the cause of the negative surface potentials seen here. Vertical black stripes at slightly over 5 minute intervals in the North-South detector show the obstruction of particles by the solar array strut extending northward from the spacecraft.

Bright vertical stripes at irregular intervals in the low energy ions (below the spacecraft potential energy) are believed to be ions generated on spacecraft surfaces and returned to the spacecraft. These ions return at detector angles between 90 and 100 degrees in both detectors, and are apparently being accelerated from above the EME box into the spacecraft.

Looking in more detail at this data, we present the distribution functions from the two detectors at 07:56 UT. Most of the interesting features in the spectrogram are found here in Figures 25 and 26, for the electrons and ions respectively. The break in the electron distribution functions in Figure 25 show the division between spacecraft and ambient populations comes at 55 eV for the NS detector, and between 100 and 120 eV for the EW detector. A bump near 40 eV in the NS detector data is an example of the accelerated electron fluxes to be studied in a later section. These fluxes are coming from a spacecraft surface that is about -40 V away from the detector potential. Data from all three ion detectors are given in Figure 26. They show a typical ion charging spike in each detector at 55 eV. These fluxes are the thermal ions which have been accelerated into the spacecraft. A flux of ions generated on or near the spacecraft appears in the NS detector between 10 and 40 eV, peaking at 25 eV.

The angular dependence of the barrier heights in the two data sets are shown in Figure 27. The barrier height

was taken to be the energy at which the electron distribution function had a distinct break or drop in value. This became difficult to determine at large detector angles. Detector angles are as defined in Figure 22, with 90 degrees radially away from the spacecraft, and 0 or 180 degrees roughly tangential to the large dish antenna (see Figure 20). The North-South detector looks roughly along the solar array strut at very low angles. We see that the two detectors both see a minimum when looking directly away from the spacecraft, and a poorly defined maximum when looking parallel to the antenna. This type of angular dependence will be seen in the monopole plus dipole model barrier in section 5.

Whether or not the trapped region is filled with electrons depends upon the intensity of electron emission at the spacecraft surface. The same phenomena on ATS-5 often gave a complete absence of electrons below the barrier energy.

3.2 JULY 22, 1974

A second example of the observed barrier is shown in Figure 28, a spectrogram for 12 hours of data from July 22, 1974 (day 203). Note that the energy scale for the ion data is inverted (zero energy at the bottom) compared to the other spectrograms in this paper. There is a small amount of charging activity beginning at 07:00, but the important features are seen between 08:00 and 11:00. An injection of hot plasma at 08:00 provides the energetic electron fluxes necessary to charge the spacecraft surfaces. We again see the mirroring of the absolute potential by the differential potential.

The gradual buildup of potential and barrier is in contrast to the rapid charging of the spacecraft upon entering eclipse, or when there is an energetic particle injection while the spacecraft is eclipsed. Both events have time scales of seconds, as opposed to the several minute time scale seen here.

In the next series of figures, we will show the spacecraft potential versus time, the barrier height versus spacecraft potential, spacecraft potential versus electron temperature, and the electron distribution functions during this time. These should illuminate some of the dynamics of the charging process. Figure 29 shows the spacecraft potential increasing exponentially with time between 08:10 and 08:40. The closeness of this curve to a straight exponential rise is remarkable, and suggests the charging cir-

cuit analogy of an RC time constant. The straight line through the early data gives a time constant of 7.6 minutes. This comparison will be pursued in the analysis section. Figure 30 gives the relationship between the differential potential and the spacecraft potential for the chargeup process. We see here that the apparent mirroring of the barrier height and spacecraft potential that is commonly seen is not exact. The barrier seems to lead the spacecraft potential initially, but reaches an equilibrium much sooner than the spacecraft potential.

A similar plot is shown for the data on February 2, 1975, in Figure 31. This is again the initial charging of the spacecraft in a hot environment. The spike energy here is actually the energy of the differential charging spike near the edge of the barrier. These spikes will be discussed below. The fit shown was done by least square fitting the logarithm of the potential and barrier heights. The resulting equation is

$$E_{\text{spike}} = 12.7 * (\text{spacecraft potential})^{*.5}$$

The $1/2$ power is a result of the fit, and was not imposed. Again, we see the barrier first leading, and then trailing the potential magnitude. The significance of the $1/2$ power has not been determined. It presumably reflects the relative charging rates of the absolute and differential potential capacitances, in terms of an equivalent circuit analogy.

A different type of information that is available in this data is the relationship between the spacecraft potential and the environment, particularly the electron temperature. Whipple (1965) has shown that for a wide variety of conditions that the spacecraft potential is proportional to the electron temperature times a logarithmic function.

Johnson et al. (1978) studied the July 22 charging event, and plotted the potential versus mean energy, as shown in Figure 32. The mean energy here is the integrated energy flux divided by twice the integrated particle flux. This is equal to the temperature for a Maxwellian distribution. The closed circles represent data from 08:00 to 09:00, i.e. the chargeup of the spacecraft following the substorm. The open circles are data points from 09:00 to 10:00, following the drop in spacecraft potential as the environment cools. The change in spacecraft potential and differential charging effects make the change in the effective temperature subject to some confusion, and we look briefly at the individual distribution functions before proceeding. Figure 33 shows the electron distribution functions at 08:00, 09:00, and 10:00. We find that the distributions are similar and differ mainly in the cutoff

at high energies, as was already apparent in the spectrogram.

We see therefore, that the temperature is indeed relatively constant during the chargeup period, and the change in potential during this time is not due to the variations in the environment. By contrast, the drop in the potential following 09:00 is due to the cooling of the environment. Two different physical processes appear to be at work during the two time periods.

4.0 DATA SUMMARY

The two days of data presented here show the dominant differential charging effects noted on almost every day of operation of the UCSD detectors. A barrier to low energy electrons is established at the same time the spacecraft begins to charge negatively, in the midnight region. This charging is in response to the injection of energetic particles during magnetospheric substorms. The height of the barrier and the magnitude of the spacecraft potential mirror one another, rising slowly following an injection, then falling as the environment cools.

A detailed look shows that the apparent mirroring of the absolute potential by the differential potential is real but not exact. The rise in differential potential initially leads the absolute potential, then follows it. The change in spacecraft potential following an injection of hot plasma shows an exponential slope suggesting the analogy of an RC circuit. This slow time development in a constant environment is in contrast to the rapid drop in potential seen in eclipses when there is an injection (several kilovolts in less than a minute). The initial charging of the spacecraft thus seems to be dependent on processes occurring on the spacecraft, in particular the development of differential potentials on the insulating surfaces. The return of the spacecraft to zero potential as the environment cools, (Figure 32) is commonly seen, and seems to be more straightforward.

5.0 BARRIER MODELS

Simple current balance models, as studied by DeForest (1972), and Prokopenko and Laframboise (1980) have shown that in the absence of photoemission, surfaces in energetic environments will charge negatively. Also, shadowed insu-

lating surfaces on a sunlit spacecraft will charge negatively.

5.1 MONOPOLE PLUS DIPOLE MODEL

To illustrate the concept of a barrier, a simple dipole model is presented here. (Besse and Rubin, 1980, have presented a similar model). A spherical object with cylindrical symmetry has a surface potential given by:

$$\text{PHI}(\text{THETA}) = V_{\text{monopole}} + V_{\text{dipole}} \cdot \text{COS}(\text{THETA})$$

with theta the angle from the z-axis. The dipole is aligned along the z axis. Potential contours for equal values for V_{monopole} and V_{dipole} of 10 V are shown in Figure 34. This shows the symmetry about the z axis, with a saddle point on the z axis at -2.5 V. Note that the top of the sphere is at zero volts potential which means that the -2.5 volt saddle point is a 2.5 volt barrier to electrons emitted from the top of the sphere. Figure 35 gives the angular dependence of the barrier height as seen from the top of the sphere. The lower curve shows the maximum potential along a ray from the top of the sphere, and therefore does not include effects due to angular momentum. The upper curve gives the results of tracking particles from the top of the sphere outward. Note the similarity of the curve shape to that seen in the particle data for July 17, 1974 (Figure 27).

Sample trajectories are shown for two sets of cases in Figures 36 and 37. Figure 36 shows the trajectories for particles emitted from the sphere with 3.5 eV kinetic energy for different initial angles, while Figure 37 presents the results for particles emitted at an angle of 45 degrees for various energies. Figure 36 reinforces the idea that the barrier height is a function of angle, and shows how a rotating detector can scan from ambient particles to spacecraft generated particles as it moves. (The trajectories are reversible, and can be considered to be the trajectories of particles incident at the top of the sphere as a function of angle). Figure 37 shows how the transition is made from spacecraft generated to ambient particle trajectories for a detector scanning in energy.

5.2 NASCAP

Studies of differential charging by Systems, Science, and Software (Mandell, et. al., 1978) have shown that spacecraft with large insulating surfaces will develop negative potentials on shaded surfaces, and that the resulting fields will then inhibit photoemission from sunlit surfaces, and cause the entire spacecraft to charge negatively. The differential potential which developed the barrier is maintained during the charging of the spacecraft. These studies used the NASA Charging Analyzer Program (NASCAP), a three dimensional code which solves for potentials and currents to spacecraft surfaces in magnetospheric environments. The potential solver portion of this code was used to model the spacecraft, and to attempt to generate a barrier to electrons by means of differential surface potentials.

Early runs with large negative potentials on the solar arrays showed that they were too far from the EME package to generate a barrier around it. The next attempt, an idealized model of the dish antenna and EME package, was very successful in generating fields which would give the observed behavior. The geometric model used in the field calculations is shown in Figure 38. The small box in the center is the EME while the large grid is the antenna. Each was fixed at a potential, and the code was allowed to solve for the resulting fields. The large equipotential surface was found to overwhelm the smaller EME surface area. Barriers to charged particles of height similar to the differential potential were found in most runs. A case of -50 V spacecraft potential, and -100 V potential was found to generate a 3 volt barrier, for example.

Ideally, we would like to match an observed data set, and set of potentials, with a model run. The primitive model and lack of information on the antenna potential makes this difficult. A data set from an eclipse event is shown in Figure 39, a spectrogram for September 8, 1974. The ion data show the spacecraft is charged to -4000 V at the end of the eclipse period, and -80 V after exiting eclipse. A differential charging barrier of 60 V height is visible in the electron data shortly after eclipse.

This case was modeled with NASCAP with -80 V on the spacecraft, and -300 V potential on the antenna. The -300 V potential was a compromise between the observed eclipse potential of the spacecraft and the observed sunlight potential of the spacecraft. Experience with this model and some luck eliminated the need to try other potentials. This model run, shown in Figure 40, resulted in a barrier height of 58 V.

NASCAP runs were made with potential distributions on the antenna which were not equipotentials. As long as the potentials were more negative than the spacecraft, a barrier was created, with the fields distorted, and the saddle point off center.

The result of these barrier calculations is the identification of the antenna as the source of the differential charging barrier seen around the UCSD detectors and the EME package. This barrier is not necessarily the same barrier that is controlling the spacecraft potential, since not all of the conducting surface areas of the spacecraft are on the EME package. Other conducting areas are the struts supporting the solar arrays and some portions of the EVM. The charging dynamics of the insulators around these surfaces are the same, however, and they are believed to behave in the same way.

5.3 TIME DEVELOPMENT

The time dynamics of the charging process can now be addressed.

The antenna structure and most of the EVM are coated with an insulator. In an active environment, the shadowed portions of these surfaces will begin to charge negatively, hindered mainly by the capacitances of these surfaces to their conducting substrates. This capacitance determines the initial time constant for the charging process. As the negative potentials on the shadowed surfaces build, limiting fields are developed which affect the sunlit surfaces of the spacecraft, as in the monopole plus dipole model of Figure 34. Once the barrier starts to form, the emitted photoelectric current and secondary electron fluxes are limited, and the current balance of the mainframe is altered. The growth of the barrier introduces a second time constant to the process. Eventually, a barrier forms that is large enough to completely limit the photoelectric current. At this time, the entire spacecraft begins to respond as though it is in eclipse. The available evidence (no daylight potential below -2 kV has been seen, in comparison to -19 kV in eclipse) suggests that some portions of the spacecraft mainframe continue to emit photoelectrons throughout this process, and are not (completely) shielded.

6.0 DATA-ACCELERATED FLUXES

6.1 SEPTEMBER 5, 1974

A phenomenon related to the barrier is the presence of accelerated electron fluxes at an energy near the barrier height. One example has been seen in the distribution function for the NS detector on July 17, 1974 (Figure 25). A clear case is shown in Figure 41, a one hour spectrogram from September 5, 1974 (day 248). The environment is highly energetic, with electron fluxes up to 80 keV, but relatively constant in time, as reflected in the constancy of the spacecraft potential at -200 V. The north-south detector is rotating, and the barrier height is varying between 100 and 200 V. The bright spots tracing the outline of the barrier are the accelerated fluxes of interest. The black stripes are due to the detector looking at one of the solar array struts at one end of its rotational pattern. Figure 42 is an energy angle spectrogram for the middle time period of the energy-time spectrogram, and shows the energy vs. angle distribution of the charged particles. The ion spectrogram at the left mainly shows the ion charging peak at 200 eV, with the rest of the ambient population above 10 keV. The electron distribution is also relatively featureless, except for the bright spots at 100 and 130 eV at the middle and left of the plot.

Data from this time period are presented in three more plots, in Figures 43, 44, and 45. Figure 43 is a plot of the count rate versus time for a minute of data at 09:02. The dotted lines show the scan in energy, while the solid line is the electron count rate. A typical scan begins at 6 seconds, and runs to 22 seconds. At low energies, there is a bump due to trapped low energy electrons, then a large spike, followed by a broad bump of ambient electrons. (about 20 keV temperature) The large spike is the 'differential charging spike' and is the flux of electrons seen in the spectrogram. The amplitude of the spike can be seen to vary with time, responding to the detector rotation.

The flux in this peak can be modeled as a Maxwellian distribution accelerated through a potential drop. Because the detector energy bins are large compared to the temperature of the distribution, it was useful to model the count rate rather than the distribution function. The results from such a model are shown in Figure 44. We see that the fluxes are well modeled by a 10 eV Maxwellian accelerated through a 95 V potential drop. The flux is equivalent to a

10 eV distribution with a density of $.164 \text{ cm}^{-3}$. There is a good chance that we are not observing the center peak of the beam of electrons, and the density estimate is low. Subject to this constraint, the thermal flux in the accelerated electrons is $8.6 \times 10^6/\text{s-cm}^2$.

The top of the spacecraft is in shadow at this time, and it is possible that these are secondary electrons and not photoelectrons. Secondary electron production is strongest for 100 to 1000 eV primary electrons. The ambient electron population in that energy range has a density of $.2 \text{ cm}^{-3}$ and a temperature of 400 eV, assuming a spacecraft potential of -191 V. If this distribution (deaccelerated by 286 V) is integrated over a secondary yield spectrum with a peak yield of 1 at 400 eV one obtains a secondary flux of $2.5 \times 10^7/\text{s-cm}^2$. The peak at 400 eV is typical of many materials, the peak value of 1 is low by a factor of 2 compared to average materials. Thus, the calculated secondary flux may be somewhat low. Even so, it is within a factor of ten of the observed flux.

Figure 45 shows a variation on the energy-angle spectrogram presentation of Figure 42. Three minutes of data were reduced to distribution functions, and plotted versus detector angle, with energy as a parameter. The largest peaks occur for 140 eV electrons at 40 degrees detector angle, and 102 eV at 100 degrees.

The variation of the energy of the peak with detector angle can be explained in terms of the electron trajectories, as illustrated in Figure 46. Higher energy electrons would take a more direct path to the detector, and enter the detector at relatively low angles, while lower energy particles enter at higher angles due to the relatively larger effect of the local electric fields. The presence of two distinct sets of curves with maxima in Figure 45 suggests the possibility of two distinct source areas at different potentials.

6.2 AUGUST 24, 1974

Speculation about the source (or sources) of the spikes eventually centered upon the only insulating surfaces near to the UCSD detectors, the University of Minnesota detectors. These small cubes were coated with an insulating white paint for thermal control. This speculation would have been limited to just that, but for the rotation of one of the two cubes. In the normal operating mode of these detectors, the detector furthest from ours rotated in 15 degree steps at 8 second intervals, covering a 180 de-

gree range in 12 steps (13 positions).

On August 24 and 25 of 1974, the UCSD detector was in a unique mode, dwelling for long time periods at energies close to the barrier height. Two hours of data from August 24 are shown in Figure 47. The spacecraft can be seen to charge negatively from 04:20 to 05:05, with differential charging also present during this time. Figure 48 shows the data taken at 61 eV when the UM detector rotated. The energy here is that of the charging spike, or accelerated electrons. The count rate increased by a factor of 5 in 50 milliseconds, with a large spike that may represent the whiplash in the UM rotational motion. Figure 49 is one of 5 other clear measurements made over this two day period. This shows the same large transition, this time in the downward direction. The gradual peaking of the data shows the effect of the UCSD detector rotation of 1.4 degrees a second.

These data show that at least one of the sources observed by UCSD is a surface of the UM detector. There is a fair possibility that the stationary box is also a source of accelerated electrons. Having observed large differential potentials on the dish antenna, it is not surprising that the UM detectors charge negatively when shadowed. The peculiar things are that they should charge to just the potential of the barrier height, and that we should see them.

A rationale for the observed charging potentials is as follows. The insulators on the spacecraft will nominally charge to different potentials. If the secondary coefficients of the white paint are fairly high, (as high or higher than that of the antenna) the shadow equilibrium of the paint will not be as negative as the silicon on the antenna. As the barrier around the EME box builds, therefore, the UM potential will lag behind somewhat. This subjects the UM detector to a limiting field, however, since secondaries it emits will not be able to escape. It must therefore charge to the potential of the barrier height, thus enabling it to achieve its own current balance with its plasma environment.

We have shown here the existence of intense accelerated fluxes of surface generated electrons, and identified at least one such source.

7.0 SUMMARY

A barrier to electrons was found to exist around the UCSD detector on ATS-6. This barrier resulted from surface potentials on the large dish antenna that were substantially more negative than the spacecraft mainframe. The differential charging was found to correspond to the absolute spacecraft potential, first leading and then following its fall.

The charging of the spacecraft was found to have a time dependence based on changes in the spacecraft, rather than changes in the environment. The exponential behavior of the spacecraft charge-up suggest an RC time constant, and possible dominance of differential charging effects in the absolute potentials attained by the spacecraft.

Intense fluxes of accelerated electrons were traced back to at least one differentially charged dielectric surface, the University of Minnesota detector. The fluxes were comparable to the secondary electron production from that surface.

ION ENGINE OPERATIONS

1.0 INTRODUCTION

ATS-6 carried on board the twin ion thrusters of the GSFC Ion Engine Experiment. These thrusters were designed to test ion engine technology and to test its usefulness for stationkeeping on the three-axis-stabilized satellite. After initial operations, the main thrusters failed, but the neutralizers were successfully operated in restart attempts in 1974, and in special operations in 1976 and 1977 to study the changes in spacecraft potentials caused by plasma emission.

The thruster operations were both in sunlight, the neutralizer operations in both sunlight and eclipse. These experiments were conducted in a range of environments, from exceptionally quiet to moderately active. Experiments were conducted with initial spacecraft potentials between +15 V and -5 kV. Major reductions were seen in differential charging barrier phenomena. These barriers were explained in the previous section as the result of large negative potential surfaces near the UCSD detector.

2.0 ION ENGINE DESCRIPTION

The thruster assemblies are illustrated in Figure 50. The discharge chamber utilizes the magnetoelectrostatic (MESG) concept, in which the magnetic and electric fields in the chamber constrain the plasma. Two parallel grids are used to extract the plasma, with the outer accelerator grid at -550 V, and the inner screen grid at +550 V. The 8 cm. diameter thruster produced one millipound (4.5 millinewtons) thrust, with .1 amp of cesium ions at a final kinetic energy of 550 eV.

The plasma bridge neutralizer is necessary to provide charge and current balance for the main beam, and is an excellent plasma source by itself. The neutralizer emission modes have a large effect on the spacecraft potentials. The cathode is located 5.0 cm. downstream from the accelerator electrode, and points 60 degrees downstream. The hollow cathode is provided with an auxiliary electrode, or probe, slightly above the cathode. In operations, cesium is fed through the cathode, and an arc is struck between the probe and cathode. The probe is initially held at +150 V with respect to the neutralizer, then drops in poten-

tial as current begins to flow. About 50 milliamps of emission current is drawn by the control circuit in operation. (Worlock, et. al., 1975; Rawlin and Pawlik, 1968; Ward and King, 1968)

The emission characteristics of the neutralizer vary with cathode temperature and cesium flow rate. At low cathode temperatures (typically in startup), operation is in a low emission current, high extraction voltage mode named plume mode, for the appearance of the discharge. (See Figure 51) Once the cathode heats up, the cesium flow rate increases and the plasma bridge enters spot mode (Figure 51 b). Spot mode is characterized by high emission currents at low extraction voltages. The neutralizer can provide substantial electron current in either mode, but does not become an efficient ion source until spot mode.

We will see that the equilibrium condition when the ion engine is operating is to have a negative spacecraft potential of a few volts. A diagram of the potential distribution in the spacecraft/ion engine system is shown in Figure 52. The distant plasma is defined as the zero volt potential point. An imaginary potential distribution along the beam is plotted above the diagram. (Ogawa, Cole, and Sellen, 1969, 1970) The extraction grids provide well defined potential points, but outside the acceleration grid, the potential distribution is less clear. A dense sheath forms outside the grid to balance the emitted ions with neutralizer electrons, and to shield the negative grid. Once past the sheath, the beam is nominally positive with respect to the spacecraft and ambient plasma, in order to trap neutralizing electrons. The potential drops slowly as the beam recedes from the spacecraft. The coupling between the neutralizer and the beam gives a potential difference between the beam and the spacecraft between 4 and 7 volts.

3.0 July 18, 1974 - Ion Engine 2

The first operation of the GSFC Ion Engine experiment was on July 18, 1974. The data taken on this day are unique for a number of reasons besides the ion engine operation. The satellite was in the earth's midnight region, normally an environment of hot (keV) plasmas. The environment was unusually quiet on this day, with $(\sum)Kp = 12+$, and no injections of hot plasmas (i.e. substorms) during the day. The previous day was also quiet, with $(\sum)Kp = 15+$, and the 3-hour Kp at the time of operation was 2. Because the magnetosphere was quiet for an extended time period, the environment was an unusually cool, dense plasma. The detectors were in an unusually good mode for this

study, with excellent low energy coverage. There was a wave-like disturbance of the magnetic field with a 5-6 minute period and a magnitude of 1 gamma(nanotesla).

Two six hour spectrograms are presented for July 18. Data from the north-south detector are in Figure 53, and from the east-west detector in Figure 54. A strong pitch angle dependence in the ion population is visible in the north-south detector data before the operation begins. Data from the east-west head showed a thermal ion population perpendicular to the magnetic field which became more apparent when the engine was operated. Looking at the spectrograms during the operations, we find the bright band of low energy electrons (0-20 eV) darkens considerably during each of the engine operations, signalling a shift in the spacecraft potential. This can be seen during the neutralizer operation from 03:10 to 03:15, and during the main thruster operations from 03:32 to 04:03 and 04:08 to 04:35. The intensification of ion fluxes at these times is also due to the potential shift.

The distribution functions from before and during the operation provide some details of the ion engine effects. Figures 55 and 56 show the ion and electron distribution functions for 03:24 (engine off) and 03:32 (engine on) from the east-west detector. The electron data at 03:24 shows a break at 5 eV, suggesting a boundary between spacecraft generated electrons (photoelectrons) and the ambient population, and thus a +5 V potential. The electrons below the break are characterized by a temperature of 2.45 eV and a density of 27.8 cm^{-3} , as determined by a least square fit of the 2.0 to 5.0 eV data. The ambient population at 03:24 between 10 and 20 eV has a temperature of 4.2 eV and density of 10.7 cm^{-3} (potential = 0), or 4.6 cm^{-3} (potential = +5V). The electrons at 03:32 give a fit with temperature 6.0 eV and a density of 1.4 cm^{-3} (potential = -3V). This latter data does not show the photoelectron flux seen at positive spacecraft potentials.

The 03:32 ion data shows a sharp drop at 3 eV, giving a -3 V potential when the engine is on. A shift of 8 or 9 eV in the particle spectra in the appropriate directions bring them into agreement, showing that there has been an 8 or 9 V shift in spacecraft potential. The absolute measurements and shift measurement give a comforting agreement.

The data were examined in this fashion throughout the operation period, and the resulting potentials are shown in Figure 57. The neutralizer probe voltage is at the top of the plot. This measurement gives the status of the small plasma bridge, particularly denoting the beginning of spot mode operation. The beam current gives the status of the main thruster. The potential measurements at the bottom

are subject to ± 1 V uncertainties, with error bars left off to avoid clutter. Small fluctuations in potential are probably real.

We see that the neutralizer operation resulted in a -1 V potential, while the full beam set the spacecraft to -4 V. The shift to negative potentials implies a distinct change in the spacecraft current balance. More photoelectrons and secondary electrons will now escape, increasing the (inwards) positive current to the spacecraft. The change in potential reduces the ambient electron flux and increases the ambient ion flux, again increasing the positive current to the spacecraft. These changes, shown graphically in Figure 58, are balanced by a net ion current leaving the spacecraft through the beam. The changes due to the small change in potential will mostly be in the thermal fluxes. The thermal electron flux has a 6 eV temperature and a density of 1.4 cm^{-3} , while the ion population is mostly a 1 eV, 2 cm^{-3} hydrogen plasma. The secondary electron fluxes in this environment are a fairly small percentage of the current balance. The photoelectron flux has a maximum value of $1 \times 10^{10} / \text{cm}^2 \text{ s}$. This is reduced by a factor of 10 to 100 by the $+5$ V potential when the neutralizer is off. The thermal fluxes for zero potential are 2×10^8 for the electrons, and 3×10^6 for the ions. The balance of currents shown in Figure 58 gives a net ion flux from the neutralizer that basically equals the integrated photoelectron flux, about 1.6 milliamps assuming 100 m^2 surface area (an extreme upper bound).

No signs of cesium ions being returned to the spacecraft were found.

4.0 October 19, 1974 - Ion Engine 1

The second successful ion engine operation began on October 19, 1974, and ran for 92 hours. The environmental conditions at this time were considerably different from those found in the first test. The operation began in the midst of a substorm, 2 hours after local midnight. Data are only available from the north-south detector head.

Two hours of data from the engine ignition period are shown in Figure 59. An injection event at 07:05 caused the spacecraft to charge to between -40 and -50 V, and causes an increase in the height of the differential charging barrier to about 100 V by 07:15. The potential can be seen to rise to near zero at 07:40-:43, when a series of short vertical lines appear in the low energy (0-20 eV) ion data. At this time also, the differential charging barrier height

drops, and then disappears completely at 08:05.

The spacecraft potential and differential charging barrier height are given in Figures 60 and 61. The spacecraft potential was measured by finding the lowest energy ion channel with measureable counts, and taking that as the spacecraft potential. This can lead to potential measurements which are too negative if there are too few ambient low energy ions to measure. Data points were taken with the detector at 90 degrees (straight up, away from the spacecraft) to minimize the effects of local fields. The measurement assumes that the observed ions are not generated on the spacecraft, which proved to be a good assumption at this angle. The barrier height was measured by examining the electron distribution function, and finding the break, or drop, where the transition to spacecraft generated to ambient particles occurs. These measurements were also made at 90 degrees. Both measurements are subject to about $\pm 10\%$ error due to the width of the energy channels.

The plasma bridge enters spot mode at 07:41 and the spacecraft potential rises to about -3 V. The differential charging barrier falls to about 20 V from 100 V about two minutes later. The engine ignition at 08:00 causes a slight drop in potential, and then the disappearance of the differential charging barrier. The time dependence of the observed effects will help explain the physical phenomena that are occurring.

The other major piece of information in the particle data is the direction of the thermal ion fluxes. There is a peculiar effect to be noted in the angular distribution of the intense fluxes of low energy (0-20 eV) ions seen after the neutralizer ignites.

These ions are neither isotropic nor field aligned, the usual angular distributions seen in this energy range. Close examination of the data at 08:26 and 08:28 on the spectrogram reveals field aligned ions down to a few eV. These are not nearly as intense as the fluxes at other angles. Furthermore, the incident angle of the intense fluxes changes with time, while the environment is almost constant. Figure 62 gives the incident angle of the intense fluxes as a function of time. We see that the intense fluxes initially appear at 83 degrees spacecraft at 07:44, several minutes after the neutralizer enters spot mode. The incident angle drops steadily until 08:10, when the thruster ignites. The incident angle stabilizes at near 0 degrees spacecraft angle thereafter. This is shown in an energy-angle spectrogram, Figure 63, for the two hours following engine ignition, from 08:45 to 11:00. Here, the time scale normally found on the horizontal axis has

been replaced by the detector angle.

The change in the incident angle of the intense fluxes reflects the changes in the local electric fields as the ion fluxes from the engine discharge the negative dielectrics on the top of the EVM, the antenna, and the solar arrays. In equilibrium, the incident direction stabilizes at one end of the detector rotational pattern, with particles entering tangentially along the antenna and solar array strut.

Having established the potential changes and time patterns, and seen some of the discharge fluxes, we now look at the physical events. Initially, the sunlit spacecraft has a number of dielectric surfaces around the conducting spacecraft components which are negatively charged with respect to the spacecraft. This condition has been shown to be the normal response of the spacecraft to an energetic particle environment. We have seen the large dish antenna is largely responsible for the barrier around the EME module. The insulators on the EVM (primarily the kapton surface of the thermal blanket) serve a similar purpose there. These barriers are essential for the development of negative potentials in this environment. Emission of electrons only (at energies below the barrier height) will not discharge the satellite. For the spacecraft to be discharged, the differentially charged insulators must be brought closer to the mainframe potential. Once the barrier has been removed, an electron current from the neutralizer can escape, and discharge the mainframe. Laboratory tests on hollow cathode devices show that the ion current extracted from a cathode depends on the extraction voltage, and suggest that for fields of tens of volts, currents of tens of microamps can be extracted. (Komatsu and Sellen, 1978)

A possible sequence of events is:

1. The negatively charged spacecraft has insulating surfaces which are negatively charged with respect to the main frame.
2. The neutralizer ignition into plume mode has no measureable effect on the spacecraft, because the thermal electrons cannot push through the barrier.
3. Spot mode operation of the neutralizer provides an ion source capable of discharging the EVM insulating surfaces which were limiting the emission of photoelectrons and secondary electrons from the conducting surfaces of the EVM. This alone probably would be sufficient to discharge the satellite.

4. The neutralizer provides an electron current as necessary to raise the spacecraft potential to -1 to -3 volts.
5. Ion fluxes from the neutralizer partially discharge the antenna, but do not complete the process. The extraction field is apparently not high enough to draw sufficient current.
6. The engine ignites, causing a shift in the operating mode of the neutralizer and providing a large flux of charge exchange ions. These ions complete the discharge of the dielectrics, leaving only sufficient potentials to maintain the ion flux to the dielectric surfaces.

4.1 OCTOBER 19 TO 23, 1974

The engine ignition process discussed in the previous section was followed by 92 hours of uneventful (from an engineering viewpoint) operation. After examination of the ignition sequence, this long operation provides a different sort of information, namely the equilibrium behavior of this charging system. We find a reassuringly constant behavior.

The rotating detector head stuck early in the operation, and was pointed in the direction of the large ion flux. This did not hinder other measurements however, and the data taken during this time show several interesting effects. Figure 64 is a 4 and 1/2 day spectrogram covering this time period. The bright band of ions can be seen to extend across most of the spectrogram. White indentations in the middle of the spectrogram at 18:00 of each day are an instrumental effect, and reflect the absence of low energy particle information at these times. The transition of the white band of ions to black seen at 0 to 4 UT on day 293 and 294 is an example of the cycling of the grey scale. The spacecraft was held at about -4 V throughout this time period, in spite of the great variety of environments the spacecraft passes through, including four large substorms. Remarkably, the night side data is free of differential charging throughout this time period. Close study shows that any differential charging effects generated no barrier above the 1 V level. This implies that fluxes of thermal ions were moving from the ion engine to the shadowed insulating surfaces which ordinarily charge negatively and cause a barrier to electrons.

Another experiment in the EVM provides us with a measure of the flux seen at the EVM near Ion Engine # 1, on the north face. The Quartz Crystal Microbalance (QCM) was designed to measure contaminant fluxes to the spacecraft surface, including the ion engine. (Rogers, 1975) The measurements made by the instrument in 1974 are shown in Figure 65. The sharp discontinuity in the curve between days 270 and 300 is the effect of the ion engine. The average accretion rate of the QCM during this period was 1.0×10^{10} ions/s cm^2 . The flux at the QCM was about an order of magnitude larger in the first few hours of operation. The flux at the EME package was about 1×10^7 ions/s cm^2 at startup, reaching a peak of 1×10^8 ions/s cm^2 at times during the operation. The distribution shown in Figure 66 is not Maxwellian, but could be two roughly Maxwellian populations. This could be the ions from the neutralizer and the charge exchange ions from the main beam.

We see that the operation of the thruster maintained the spacecraft near zero volts potential, eliminated the problem of differential charging, and as a result greatly improved the particle data. The length of the operation allowed the QCM measurement to be made, and showed there will be intense plasma fluxes near the ion engine.

5.0 I.E. 2 NEUTRALIZER OPERATIONS

The failure mode of the ion thruster was not understood until long after the July operation of engine no. 2. Because of this, the restart attempts of the engine, with and without the neutralizer, continued until the power supply was so badly shorted out that it could not supply the necessary heater current to send the plasma bridge into spot mode. During the latter stages of the restart attempts, the transitions to spot mode did come, but slowly, providing us with the opportunity to study some of the time dependence of these transitions.

5.1 JULY 20, 1974

The initial restart attempts on July 20 occurred in the midst of a substorm environment, one in which the spacecraft was negatively charged, with an electrostatic barrier around the spacecraft. These operations were similar, therefore, to those on October 19 discussed previously. When the neutralizer reached spot mode, the spacecraft would discharge, and the differential charging would decre-

ase. When the neutralizer was turned off thereafter, the spacecraft began to recharge if the environment was still active enough.

A spectrogram for the north-south detector data is shown in Figure 67 for the 5 hour period when the operations took place, and a two hour spectrogram for the fixed ion detector and east-west ion detector is shown in Figure 68. An injection at 04:40 started the magnetic activity, with the first neutralizer operation coming at 06:10. By this time, the spacecraft had already charged to -50 V, and discharged back to near zero volts. A small differential charging barrier of 10 or 20 V is still in evidence around the EME package. The neutralizer enters spot mode at 06:13 for about two minutes. A large ion flux appears in the fixed detector at this time, and the differential charging barrier drops to a few volts at most. This drop was probably due to both the drop in the energy of the environment and the discharge effect of the neutralizer ion fluxes. The environment was not energetic enough to reestablish the differential charging barrier after it had been eliminated.

A larger substorm at 06:35 generates a new differential charging barrier, with negative spacecraft potentials beginning at 07:00. The delay here is due to the operation of the neutralizer at this time. The neutralizer is switched on at 06:30, and ignited into plume mode between 06:40 and 06:45. The barrier began to build in height at 06:37, but is clearly diminishing in height by 06:50, though the environment has not yet cooled at all. The cause for this drop in the differential charging barrier was the ignition of the neutralizer into spot mode at 06:49. Ions from the neutralizer are reversing the normal development of a barrier. Ions from the neutralizer appear in the fixed detector at this time, lasting from 06:49 to 06:54, when the ion engine arcing caused the engine to shut down. The differential charging around the spacecraft resumes its increase at this time, and the spacecraft charges negatively at 07:00 reaching -30 or -40 V.

The neutralizer is again turned on at 07:06 and ignites by 07:15. Spot mode occurs briefly from 07:18 to 07:19, and this is enough to discharge the satellite. Plume mode operation is then sufficient to maintain the spacecraft at near zero potential. Spot mode resumes at or before 07:25, and large ion fluxes appear in the fixed detector again, lasting until the engine arcs off. These fluxes are visible in the east-west detector when it is looking parallel or antiparallel to the fixed detector. In this last portion of the experiment, the transition to spot mode was quite slow, and we have a measurement of the energy of the ion fluxes at the UCSD experiment as a function of the neutralizer probe voltage, which is the primary neu-

tralizer status monitor. Looking at this portion of the operation in more detail, the ion distribution functions from the fixed detector are shown for three times during the operational period, and once from before ignition are given in Figure 69. The normal charging peak at 39 eV is due to the negative spacecraft potential that has developed. The warm thermal plasmas below this energy have been swept into the detector. Note that these are warmer than the plasmas seen two days earlier. When the neutralizer begins to operate, we find the potential dropping, and a high sharp peak forming in the low energy channels. The peak is at its lowest energy initially, at 07:23, at 4 eV. The peak increases in energy, passing through 8 eV at 07:30, and reaches a maximum at 12 eV at 07:33, just before the neutralizer switches off. The extreme height of this peak, an order of magnitude over the natural charging peak, shows that this plasma is from the neutralizer.

The same data set is presented in a slightly different way in Figure 70. The count rate from the fixed detector is plotted for the 5 eV, 12 eV, and 42 eV channels. The 42 eV channel is the natural charging peak. This peak disappears at 07:18 when the neutralizer briefly enters spot mode. There is a brief surge in the two low energy channels, but the counts then drop back to background until 07:22. The neutralizer enters plume mode at this time, and substantial fluxes are seen at 5 eV, with lower fluxes found at 12 eV. Spot mode operation begins at 07:27, and the fluxes increase in energy. This is a reflection of the movement in the peak energy of the distribution function presented in Figure 69.

We see now that the neutralizer mode is controlling the intensity and energy of the plasma reaching the UCSD detector. These ions are again reaching the differentially charged dish antenna in sufficient quantity to partially discharge the antenna. There is a drop in the barrier height from 50 V to 30 V occurring between 07:28 and 07:30, just as the neutralizer enters spot mode. The variations in ion fluxes seen at this time therefore represent the changes in local fields at this time as well as the variations in neutralizer mode.

The differential charging barrier drops during spot mode, then increases between 07:30 and 08:00. After 08:00, the cooling plasma causes the barrier to drop naturally.

5.2 JULY 21, 1974

Operations on the following day were in a quieter environment, and the neutralizer did not cause major changes in the spacecraft potential. Figure 71 shows the data from the east-west detector for the operations on this day. The major feature of the spectrogram is the broad band of photoelectrons stretching along the low energy electron data. It is broken up into darker patches as neutralizer operation reduces the positive spacecraft potential for periods of up to 25 minutes.

We look again at the relationship between spacecraft potential and the neutralizer status. The spacecraft potential must be inferred entirely from the electron data at this time, because of the relatively large positive potential and absence of visible ions. The distribution functions for the east-west detector electrons are plotted for 02:43, when the neutralizer is off, and for two times when the neutralizer is in spot mode, 03:01 and 03:28. The shapes in Figure 72 can be seen to be the same, they are simply shifted in potential by 6 to 7 volts. Breaks in the distribution functions imply the equilibrium spacecraft potential here is +14 V when the neutralizer is off, and + 8 V in spot mode. (note that the neutralizer does not fully reach spot mode, compare July 18). Using the break in the distribution functions and their shifts relative to each other, the potential was obtained as a function of time. Plotted in Figure 73 along with the probe voltage, we see again the strong dependence of the spacecraft potential on the neutralizer mode.

The spacecraft is driven toward zero by the neutralizer at 03:00 and 03:30 by the two operations. Although the probe voltage telemetry does not come on scale for much of this period, it appears that the neutralizer was on the edge of spot mode during the periods the spacecraft is partially discharged. This is the case from 02:55 to 03:05 and from 03:22 to 03:32. When the probe voltage drops to 5 or 10 V, and the neutralizer ion current increases, we see a further drop in the spacecraft potential, as seen at 03:30.

We find again that the neutralizer mode affects its ability to produce ions, and the ion current produced by the neutralizer determines the spacecraft potential.

6.0 ECLIPSE OPERATIONS

As part of the program to study the effects of the ion engine on spacecraft potential, and to study means of modifying potentials, the ion engine neutralizers were operated during periods of spacecraft eclipses. ATS-6 was normally at a positive potential in sunlight in quiet environments. If the positive spacecraft then entered eclipse, the particle data usually showed a small shift in the negative direction as the photoelectric current was cut off. The equilibrium potential in such eclipses was generally between +1 V and -3 V. In energetic environments, the sunlit satellite was generally 10's of volts negative to as much as a kilovolt negative. Under such conditions, an eclipsed satellite normally charged to several kilovolts negative.

Analysis of the neutralizer operations associated with the full thruster tests suggest that the neutralizer should do as thorough a job of controlling the spacecraft potential in eclipse as it did in sunlight. We will see that this is so.

6.1 OCTOBER 14, 1976

An example of an operation in a quiet environment in eclipse is found on October 14, 1976. The data are again displayed in spectrogram format, in Figure 74. The detector head is parked at 100 degrees spacecraft angle, or about 55 degrees pitch angle. No thermal ions are visible before the operation. The time sequence of this operation was as follows

Neutralizer ignition	03:50
Spot mode	03:57
Full eclipse	04:13
Neutralizer off	04:21
Exit eclipse	04:29

The behavior here is similar to that seen in the operations in July, 1974. The positive spacecraft is pushed negative by the neutralizer operation, allowing the appearance of the ambient thermal ion population. The identification of the particles as ambient is reinforced by the similarity of the fluxes from 04:00 to 04:10, when the sunlit spacecraft was pushed negative by the neutralizer, and the fluxes from 04:21 to 04:28, when the eclipsed spacecraft was naturally slightly negative. It is noteworthy

that the eclipsing of the satellite caused a shift in the spacecraft potential while the neutralizer was operating.

Simple current balance arguments again show that the neutralizer is emitting a net ion current both in the sunlight case and in the eclipse period. Figure 75 shows the argument for the eclipse case, the sunlight case is the same as in Figure 58. The ambient electron current and balancing secondary electrons are unaffected by the minor change in potential, since the electron temperature is high and all the secondaries are escaping. The ion flux increases by a factor of two or three due to the change in potential, and it is this change the neutralizer must balance. In the sunlight case, the major changes due to the shift in potential are the increase in emitted photocurrent, a slight drop in the current due to ambient electrons, and an increase in the ambient ion current. Each of these changes causes a net increase in the positive current to the spacecraft. This change must be balanced by the neutralizer, which must therefore be emitting a net ion current. The fact that there is a difference in the potential when spacecraft enters eclipse shows the neutralizer ion current is affected by the extraction voltage.

6.2 SEPTEMBER 3, 1976

When the environment at local midnight was an active one, as is frequently the case, the operation of the neutralizer provided substantially different results in eclipse. The operations in active environments showed that the neutralizer could prevent the negative charging of the spacecraft mainframe, or discharge a negatively charged satellite. An event of the first type occurred on September 3, 1976 (day 247). Data from this operation are displayed in Figure 76. The important times in this sequence are:

Neutralizer igniton	00:03:00
Begin Eclipse	00:17:55
Full Eclipse	00:20:50
Neutralizer off	00:30:35
Begin eclipse exit	00:52:00
Full Sunlight	00:54:55

Eclipse times are taken from measurements of the solar array current, which is proportional to the illumination of the satellite. Injections at 023:55 and 00:15 can be seen by their effects on the high energy electron data. The two events have an unfortunate coincidence with the other time events in the operation.

The 23:55 injection would have caused the buildup of a differential charging barrier, but the ignition of the neutralizer at 00:03 prevented this. A small burst of ions can be seen at ignition, presumably from the neutralizer. The later injection was energetic enough to begin the formation of a barrier of about 20 V even with the neutralizer on. Cesium ions appear again at eclipse entry as the spacecraft fields adjust to the negative antenna. The barrier seems to persist even after eclipse entry. This has been seen in some cases of this spacecraft when the neutralizer was not operated. Switching the neutralizer off allowed the spacecraft to charge negatively to -4 kV, and the rest of the eclipse process proceeded normally.

We see from this operation that the neutralizer can provide sufficient current to prevent kilovolt charging in eclipse, something the electron emitting filament on ATS-5 was unable to do.

6.3 APRIL 7, 1977

Finally, we show an example of the neutralizers ability to discharge a spacecraft in eclipse. Two operations in April 1977 showed that if the spacecraft was charged several kilovolts negative, the neutralizer would discharge the satellite. Figure 77 shows the results from April 7, 1977. The solar array current reflects the illumination of the spacecraft, the neutralizer probe shows its status, and the potential at the bottom comes from UCSD ion data. The spacecraft charges to -3 kV in eclipse from 09:05 to 09:15, and the potential rises to near zero at 09:15 when the neutralizer ignites. The neutralizer is an excellent electron source even in plume mode, and the absence of differential charging in this case means that ions are not needed in such abundance. The spacecraft remains near zero potential until the neutralizer is switched off at 09:33. At this time, the spacecraft potential falls to -1.5 kV for the few minutes remaining in eclipse.

In behavior similar to that in the September experiment just described, neutralizer operation has provided the necessary electron current to discharge the satellite, and maintain it at low potentials. This is again in contrast to the observed results of filament emission of electrons on ATS-5. The difference is again the need to have ions present to discharge the dielectrics.

7.0 SUMMARY

We see that operation of the ion engines and plasma bridge neutralizers had major effects on the spacecraft potential with respect to the ambient plasma, and on the differential potentials on the spacecraft surfaces. The neutralizer or the engine could discharge large negative potentials at all times. Differential charging was reduced by the neutralizer when operated in spot mode (i.e. as an ion source), and eliminated by operation of the ion engine.

The operation of the neutralizer or the main thruster in a quiet environment resulted in the production of a net ion current by the engine, sufficient to drive the spacecraft slightly negative. Moving into eclipse changed the amount of ion current being supplied by the neutralizer.

When the neutralizer was used in daylight cases of negative charging, i.e. in active environments, the neutralizer caused the spacecraft to rise to a few volts negative potential, and the reduction of differential charging on the insulating surfaces of the spacecraft. Operation of the thruster in active environments held the spacecraft at -4 to -5 V potential, and eliminated the problem of differential charging. Fluxes of ions were seen from the engine and neutralizer when the spacecraft was in active environments.

The small plasma source has definite applications in the area of controlling harmful spacecraft potentials.

BIBLIOGRAPHY

Besse, A.L., and A.G. Rubin, A simple analysis of spacecraft charging involving blocked photoelectrons, Journal of Geophysical Research, 85, p 2324, 1980.

DeForest, S.E., Spacecraft charging at synchronous orbit, Journal of Geophysical Research, 77, p 651, 1972.

DeForest, S.E., Electrostatic potentials developed by ATS-5, Photon and Particle Interactions with Surfaces in Space, pp 263-276, R.J.L. Grard, ed., D. Reidel, Holland, 1973.

Gibbons, D.S., Secondary electron emission, Handbook of Vacuum Physics, Beck, ed., Pergamon Press, Oxford, vol. 2, part 3, 1966.

Grard, R.J.L., K. Knott, A. Pederson, Influence of photoelectron and secondary emission on electric field measurements in the magnetosphere and solar wind, Photon and Particle Interactions with Surfaces in Space, R.J.L. Grard, ed., D. Reidel, Holland, pp 163-189, 1973.

Hachenberg, O., and W. Brauer, Secondary electron emission from solids, Advances in Electronics and Electron Physics, Academic Press, New York, XI, pp 413-499, 1959.

Katz, I., D.E. Parks, M.J. Mandell, J.M. Harvey, D.H. Brownell, S.S. Wang, and M. Rotenberg, A Three Dimensional Dynamic Study of Electrostatic Charging in Materials, NASA CR-135256, SSS-R-77-3367, 1977.

Knott, K., Equilibrium potential of a magnetospheric satellite in an eclipse situation, Planet Space Sci., 20, pp 1137-1146, 1972.

Komatsu, G.K., and J.M. Sellen, Jr., A plasma bridge neutralizer for the neutralization of differentially charged surfaces, Effect of the Ionosphere on Space and Terrestrial Systems, J. Goodman, ed., NRL and ONR, 1978.

Lovell, R.R., N.J. Stevens, W. Schober, C.P. Pike, and W. Lehn, Spacecraft charging investigation: A joint research and technology program, Spacecraft Charging by Magnetospheric Plasmas, Progress in Astronautics and Aeronautics, 47, A. Rosen, ed., 1976.

Mandell, M.J., I. Katz, G.W. Schnuelle, P.G. Steen, and J.C. Roche, The decrease in effective photocurrents due to saddle points in electrostatic potentials near differentially charged spacecraft, IEEE Transactions on Nuclear Science,

6, (NS25), 1313, 1978.

Mauk, B.H., and C.E. McIlwain, ATS-6 UCSD auroral particles experiment, IEEE Transactions on Aerospace and Electronic Systems, vol. AES-11, p 1125, 1975.

McPherson, D.A., and W.R. Schober, Spacecraft charging at high altitudes, the SCATHA satellite program, Spacecraft Charging by Magnetospheric Plasmas, Progress in Astronautics and Aeronautics, 47, A. Rosen, ed., 1976.

Olsen, R.C., and E.C. Whipple, Active Experiments in Modifying Spacecraft Potential: Results from ATS-5 and ATS-6, NASA 5-23481, 1979.

Prokopenko, S.M.L. and J.G. Laframboise, High-Voltage differential charging of geostationary spacecraft, Journal of Geophysical Research, to be published, 1980.

Rawlin, V.K., and E.V. Pawlik, A mercury plasma-bridge neutralizer, Journal of Spacecraft and Rockets, 5, pp 814-820, 1968.

Rogers, J.F., ATS-6 quartz crystal microbalance, IEEE Transactions on Aerospace and Electronic Systems, vol AES-11, p 1185, 1975.

Ogawa, H.S., R.K. Cole, and J.M. Sellen, Measurements of equilibration potential between a plasma "thrust" beam and a dilute "space" plasma, AIAA 7th Electric Propulsion Conference, #69-263, 1969.

Ogawa, H.S., R.K. Cole, and J.M. Sellen, Factors in the electrostatic equilibration between a plasma thrust beam and the ambient space plasma, AIAA 8th Electric Propulsion Conference, #70-1142, 1970.

Sternglass, E.J., Secondary electron emission and atomic shell structure, Phys. Rev., 80, pp 925-926, 1950.

Ward, J.W., and H.J. King, Mercury hollow cathode plasma bridge neutralizers, Journal of Spacecraft and Rockets, 5, p 1161, 1968.

Whipple, E.C., Jr., The Equilibrium Potential of a Body in the Upper Atmosphere and in Interplanetary Space, NASA Technical Note X-615-65-296, 1965.

Whipple, E.C., Jr., Theory of the spherically symmetric photoelectron sheath: A thick sheath approximation and comparison with the ATS-6 observation of a potential barrier, Journal of Geophysical Research, 81, p 601, 1976a.

Whipple, E.C. Jr., Observation of photoelectrons and secondary electrons reflected from a potential barrier in the vicinity of ATS-6, Journal of Geophysical Research, 81, p 715, 1976b.

Whipple, E.C., and R.C. Olsen, Experiments on regulation of electric charge on space vehicles, AIAA conference, 1979.

Worlock, R.M., E.L. James, R.E. Hunter, and R.O. Bartlett, ATS-6 cesium bombardment engine north-south stationkeeping experiment, IEEE Transactions on Aerospace and Electronic Systems, vol. AES-11, p 1176, 1975.

WARM IONS IN THE MIDNIGHT SECTOR

1.0 INTRODUCTION

The appearance of low energy ions in the UCSD particle data during ion engine operations required a study of the nature of the thermal ion population in the midnight sector of the magnetosphere. This study made it possible to separate the ambient thermal plasmas and the plasmas generated by the ion engine in the particle data taken during engine operations.

The study of 1 to 100 eV plasmas showed that there were two possible populations in the midnight sector. The most commonly seen population was a field aligned, thermal plasma. Fluxes of this type were strongest after long periods of quiet (12 hours or more) with ΣKp less than 20. Local Kp needed to be 2 or less for the population to appear. A novel feature of these populations was the discovery that they are well modeled as Maxwellian populations displaced in velocity space parallel to the magnetic field line. In extremely quiet environments, an isotropic, cold plasma population developed, appearing only during eclipses or ion engine operations. Positive spacecraft potentials hid the cold ion population at other times.

2.0 Fitting procedure

An interactive fitting procedure was developed to study the thermal ion populations after it was discovered that they were not simple Maxwellian distributions.

The fitting procedure was to model the observed distribution as a sum of Maxwellians displaced in velocity along the magnetic field line. The equation used was:

$$f = \sum n_i \left(\frac{m_i}{2\pi kT_i} \right)^{3/2} \exp \left(-\frac{m_i (\vec{v}_\infty - \vec{v}_{\text{stream}})^2}{2kT_i} \right)$$

$$v_\infty = \left(v_{s/c}^2 + (2q/m) \phi_{s/c} \right)^{1/2}$$

One assumption made in this work is that the trajectories are not greatly distorted by the spacecraft fields. This assumption is reasonable as long as there is not substantial differential charging, and the absolute potential is not large compared to the initial kinetic energy of the particles.

3.0 September 18, 1974

The first, and clearest, case of the equilibrium field aligned plasma population is from September 18, 1974. The data from this event are displayed in spectrogram format in Figure 78. The two hours of data around local midnight were taken with the rotating detector assembly that sweeps in a north-south plane on the fixed satellite. The spectrogram covers the time period 05:00 to 09:00 UT, with an eclipse occurring between 05:35 and 06:45. The pitch angle is plotted at the top of the spectrogram, with electron data below, and finally the ion data. The detector look direction comes within 14 degrees of the magnetic field line in this data set, looking at particles streaming north from the equator. The bright streaks in the 0-20 eV range in the ion data are the low energy field aligned ions. The pitch angle distribution is plotted for 5 eV data taken during the eclipse period in Figure 79. It can be seen that the particles are strongly field aligned, dropping to background by 40 degrees, and one-half maximum by 20 or 25 degrees. It is not clear from this data set what the pitch angle structure below 15 degrees is. Other data sets seem to indicate that these populations are truly field aligned, with no depressions at lower angles.

Distribution function plots with the Maxwellian fits are given in Figure 80 for spectra at the end of the eclipse. Note that the energy scale is actually the energy per unit charge, as is measured by the detector. The fits of the eclipse data give a clear measurement of H⁺ streaming at 30 km/s, with a temperature between .8 and 1 eV, and a density of about 15 cm⁻³. Count rates are into the thousands in the 4-20 eV region, well above background noise and statistical fluctuations. At higher energies (20-100 eV), counts of 20-50 are measured, which are above background, but subject to statistical fluctuation. With this limitation noted, we find He⁺, O⁺, and O⁺⁺ streaming at 30 km/s, with temperatures of 1.5 eV, 10 eV, and 5 eV respectively. Densities are about 0.1 cm⁻³ for He⁺, and .2 cm⁻³ for each of the oxygen species.

The magnetic activity is the crucial factor in determining the observation of this plasma in the midnight sector. The (sum)Kp for this day was 20, which is moderately high, but the previous day had a (sum)Kp of 7-, and on this day kp(6 UT)=1-. There were no injections of hot plasma (i.e. substorms) in the previous 18 hours, as observed by ATS-6.

The potential was between +1 v and -1 v during the eclipse, and this greatly enhanced the measurement. Outside eclipse, this environment allowed the photoelectron flux

from the spacecraft surface to dominate the spacecraft current balance, and drive the spacecraft between 5 and 10 volts positive. The effect of exiting eclipse on the ion data can be seen in Figure 80 where the sunlight spectra can be seen to be shifted about 5 to 10 eV in energy. Note that the hydrogen peak begins to disappear at positive potentials of 5 to 10 V.

On September 18, 1974, the first magnetic activity of the night did not occur until after local midnight, which reflects the low magnetic activity on this day. Following the strong fluxes observed in eclipse, there was another hour of constant streaming. Returning to Figure 78, we see the field aligned fluxes intensify and increase slightly in energy until 08:00, when the magnetic activity begins to interfere with the streaming. In the injection event, there is a large acceleration of the streaming which is most visible at 08:08 and 08:13. The population disappears after the injection.

The increase in stream velocity makes the multiple ion species much more distinct, and it was just this behavior which brought about their identification. Figure 81 shows the spectra from 07:37:49, 07:41:25, and 07:48:13 as the stream velocity increases from 35 km/s to 45 km/s. Assuming similar stream velocities, multiple peaks in the distribution function are easily identified as H^+ , He^+ , O^+ , and O^{++} . The stream velocities of the different species remain within 10 % of each other throughout the acceleration process.

At the injection at 08:02, we find a moderate streaming velocity of 50 km/s, as seen in Figure 82. The increase in velocity was not monotonic, however, and there were higher velocities both before and after this time. It is at these higher velocities that the multiple mass components become clear. The contribution of each of the 4 species is shown in Figure 82. It was because of such relatively clear cases that the multiple species identification was extended to quiet time data.

The peak velocity is seen at 08:07 in Figure 83. The streaming velocity has reached a maximum of about 150 km/s, a maximum that was equaled in some other injections. The thermal fluxes effectively disappeared after the injection. This population rebuilds slowly following an injection.

4.0 October 8, 1974

One clear observation of an isotropic, warm plasma population was made on ATS-6. This came during an eclipse,

when the repelled ions were able to reach the spacecraft. Figure 84 is an 8 hour spectrogram for October 8, 1974. The eclipse period is from 05:35 to 06:32, and is clearly visible in the spectrogram as the period where a bright band of low energy ions appear in the particle data. The count rates prior to and after eclipse are at the background level. Figure 85 shows the count rate versus detector angle for 27 minutes of data in the second half of the eclipse. The dip at the end of the plot show the obstructing effects of the spacecraft body. The count rates of the 2 and 5 eV channels are otherwise relatively constant over the angular scan pattern.

Fits to the distribution functions gave a 2 to 3 eV temperature, and a density of 10 to 50 cm^{-3} , after correcting for spiraltron degradation and a spacecraft potential of about -2 V . A positive spacecraft potential of 10 V in sunlight was sufficient to exclude the cool plasma.

5.0 Summary

Two examples of the low energy plasma population in the midnight region have been given. Most observations made in the ATS particle data corresponded to the first example given, a field aligned plasma, streaming along the magnetic field line with a kinetic energy comparable to or greater than the thermal energy of the plasma. The only other population observed in the particle data was an isotropic plasma that was considerably less energetic than the field aligned flows. This plasma only becomes visible in eclipses, as shown here, or during ion engine operations, as occurred on July 18, 1974.

FIGURES

Figure 1. ATS-5 spacecraft drawing, showing the locations of the UCSD detectors and the ion engine experiments.

Figure 2. ATS-5 ion engine experiment. The neutralizer filament is at the end of the experiment, near the exit aperture.

Figure 3. ATS-5 spectrogram, October 16, 1969. This grey scale presentation of UCSD particle data plots low count rates as black or dark gray, and higher count rates as light gray or white. The gray scale overflows at high count rates, as seen at 4500 eV in the ion data from 06:30 to 07:00 universal time. The energy scales both start at 0 eV in the center, increasing up and down, for electrons and ions respectively. The eclipse event from 06:20 to 07:20 is the period when the spacecraft charges to -4 kV. The electron fluxes decrease, as shown by the darkening from 0 to 4 keV. The ion fluxes show an absence from 0 to 4 keV, with a large peak at the charging energy.

Figure 4. ATS-5 spectrogram, September 20, 1974. Format as above, but with a shorter time scale. The electron filaments are operated twice, causing a discharge of the satellite, at 06:35 and 07:10.

Figure 5. ATS-6 spectrogram, September 20, 1974. Two hours of data at local midnight, showing an eclipse charging event.

Figure 6. Potential plot for September 20, 1974 neutralizer operation. The mainframe potentials for both ATS-5 and ATS-6 are plotted for the eclipse period.

Figure 7. Potential plot for September 30, 1974 neutralizer operation, as above.

Figure 8. Potential plot for March 28, 1978 neutralizer operation.

Figure 9. Summary of ATS-5 neutralizer operations from 1974 to 1976. Crosses represent individual measurements, circles multiple measurements. The solid line shows the potential on=potential off boundary.

Figure 10. True secondary yield as a function of ambient electron energy, and ATS-5 channel number. Both are logarithmic scales. Parameters are those for a material with a maximum yield of 1 at 400 eV at normal incidence.

Figure 11. Backscatter yield as a function of ambient elec-

tron energy and ATS-5 channel number. Parameters are those for a material with atomic number 10, at normal incidence.

Figure 12. Secondary electron yield as a function of ion impact energy, and ATS-5 channel number, for normal incidence.

Figure 13. The integral yield for true secondaries as a function of the temperature of the incident Maxwellian distribution. The parameters are for a material with a maximum yield of 1 at 400 eV, using the normal incidence values.

Figure 14. The net current density to a surface in a Maxwellian environment is plotted as a function of surface potential. The ion temperature is 5 keV, electron temperature varies from 2 to 10 keV. The yield terms plotted previously are used, but with the angular averaging effects included.

Figure 15. NASCAP/ATS-5 model object. The object is defined on a rectangular grid, and is an octagon. Small darkened regions show the conducting area, light squares are the insulating surface area.

Figure 16. ATS-5 object potential contours, generated by NASCAP. The contour cut is through the center of the object. The potential contours from -50 V to -70 V are plotted for an object at -50 V, with insulators at -70 V. A saddle point is shown by an X in front of conducting areas, this point is at -53 V.

Figure 17. ATS-5 NASCAP time sequence. This plot shows the mainframe potential of the object, and the differential potential of the insulating cells as a function of time. The solid lines and dots are the conductor potential, with a scale on the on the right. The environment is a single Maxwellian of 10 keV energy.

Figure 18. ATS-5 NASCAP time sequence. As above, for a double Maxwellian environment, with 100 eV and 10 keV plasmas.

Figure 19. ATS-5 detector efficiencies. The average count rate of the ATS-5 detectors is plotted versus Monterey day, from Fall 1969 to Fall 1974. Plus (+) signs are for 1973 data, which is not used in the study.

Figure 20. ATS-6 spacecraft, the location of the detectors on the spacecraft, and the relationship of the spacecraft to the earth.

Figure 21. ATS-6 EME package photograph. The UCSD detectors are the cylindrical heads extending from near one

corner of the package. The University of Minnesota detectors are the two white boxes near the center of the EME, on the opposite side from the UCSD detectors.

Figure 22. UCSD detector angle definition. The left drawing emphasizes the north-south rotating detector assembly, the right drawing the east-west rotating detector assembly.

Figure 23. ATS-6 spectrogram, July 17, 1974. Two hours of data from the north-south detector. The diagonal pattern at the top of the figure shows the pitch angle of the particles measured by the rotating detector.

Figure 24. ATS-6 spectrogram, July 17, 1974. Two hours of data from the east-west detector. The diagonal pattern at the top of the figure shows the detector angle.

Figure 25. ATS-6 electron distribution functions from July 17, 1974. Data was taken at 07:56 UT, for the north-south detector at 100 degrees, and the east-west detector at 10 degrees.

Figure 26. ATS-6 ion distribution functions from July 17, 1974. Data from the north-south, east-west, and fixed ion detectors is included.

Figure 27. ATS-6 differential charging barrier height as a function of detector angle. Spacecraft potential is -55 V, the minimum in barrier height is between 50 and 60 V.

Figure 28. ATS-6 spectrogram, July 22, 1974. Twelve hours of data from the north-south detector. The charging event of interest is between 08:00 and 10:30 UT.

Figure 29. ATS-6 potential plot, July 22, 1974. Potential is plotted against universal time, with a straight line plot of a 7.6 minute time constant superimposed.

Figure 30. ATS-6 potential plot, July 22, 1974. Barrier height is plotted against spacecraft potential. The straight line is to show where the absolute potential equals the barrier height.

Figure 31. ATS-6 potential plot, February 2, 1975. Charging spike energy is plotted against spacecraft potential. The straight line is a least square fit to the form $E_{\text{spike}} = (-\text{potential})^{0.5}$.

Figure 32. ATS-6 potential plot, July 22, 1974. Spacecraft potential is plotted against the temperature of the environment from 08:00 to 10:00. Dark circles are the first hour, open circles the second.

Figure 33. ATS-6 electron distribution functions, July 22, 1974. Three distribution functions taken during the charging event, showing the cooling of the environment.

Figure 34. Monopole + dipole model potential contours. The spherical (circular) surface is the inner boundary, solid lines the equipotentials. The dotted line is the potential minimum along rays from the top of the sphere. There is a saddle point at -2.5 volts above the top of the sphere.

Figure 35. Monopole + dipole model barrier height. The height of a barrier seen by an emitted particle is plotted against the emission angle measured from the normal to the top of the sphere. The lower trace is the maximum potential along a ray from the top of the sphere, the upper trace was created by particle tracking, and includes angular momentum effects.

Figure 36. Monopole + dipole model trajectories. Trajectories are shown for different emission energies at a constant emission angle, 45 degrees. Trajectories at less than 2.93 eV return to the sphere.

Figure 37. Monopole + dipole model trajectories. Trajectories are shown for different emission angles at a constant emission energy, 3.5 eV. Trajectories at greater than 60 degrees are returned to the sphere.

Figure 38. NASCAP/ATS-6 antenna object. Two views of the object designed to study ATS-6 barrier effects. The large flat plate is the dominant feature, intended to represent the ATS-6 dish antenna. The hole is filled with a small box, 2 grid units square by 1 grid unit high, intended to represent the EME.

Figure 39. ATS-6 spectrogram, September 8, 1974. Two hours of data around an eclipse event, with charging during and after the eclipse.

Figure 40. NASCAP/ATS-6 potential contours. The potential contours are given for the case of -80 V on the small box, and -300 V on the antenna plate. A saddle point is formed over the box at -138 V.

Figure 41. ATS-6 spectrogram, September 5, 1974. One hour of data from the north south detector, emphasizing the structure seen in the charging data.

Figure 42. ATS-6 spectrogram, September 5, 1974. One-half hour of data in an energy-angle format. The horizontal axis is the spacecraft angle of the north-south detector, the vertical axis is a log energy scale.

Figure 43. ATS-6 line plot, September 5, 1974. One minute of data, 09:02 UT. Dotted vertical lines show the detector energy, with scales on the left and right. The count rate from the north-south electron detector is plotted on the upper scale.

Figure 44. ATS-6 electron flux, September 5, 1974. The modified count rate is plotted against energy, with a pair of Maxwellian fits over two energy ranges. The first fit is for a 9.74 eV Maxwellian, with density $.164 \text{ cm}^{-3}$, accelerated through a 95 V potential. The higher energy fit is for a 400 eV Maxwellian with density $.187 \text{ cm}^{-3}$.

Figure 45. ATS-6 electron distribution functions, September 5, 1974. The distribution function from a 3 minute period is plotted against north-south detector angle, parameterized by energy.

Figure 46. ATS-6 electron trajectories. Possible trajectories of electrons from the dish antenna to the UCSD detectors are shown.

Figure 47. ATS-6 spectrogram, August 24, 1974. Two hours of data from the north-south detector are given.

Figure 48. ATS-6 electron count rate, August 24, 1974. Five seconds of data from the north-south detector are plotted versus time. Particles are 61 eV in energy.

Figure 49. ATS-6 electron count rate, August 25, 1974. Five seconds of data from the north-south detector are plotted versus time. Particles are 102 eV in energy.

Figure 50. ATS-6 ion engine diagram.

Figure 51. Plasma bridge neutralizer operational modes, plume mode and spot mode. Physical, circuit diagram plots are at the top, with potential and density diagrams along the anode cathode line given below.

Figure 52. Ion engine potential diagram. The potential and plasma distributions in and around the ion engine are given. Plasma density and potential decrease away from the engine radially and downstream.

Figure 53. ATS-6 spectrogram, July 18, 1974. Six hours of data from the north-south detector. The ion engine operation from 03:30 to 04:30 causes an increase in ion fluxes which causes the grey scale to saturate, and cycle back to black in the 0 to 20 eV range.

Figure 54. ATS-6 spectrogram, July 18, 1974. Six hours of data from the east-west detector.

Figure 55. ATS-6 electron distribution functions. Data from the east-west detector is given for 03:24 and 03:32 on July 18, 1974.

Figure 56. ATS-6 ion distribution functions. Data from the east-west detector is given for 03:24 and 03:32 on July 18, 1974.

Figure 57. ATS-6 potential during ion engine operation. The spacecraft potential, ion beam current, and neutralizer probe voltage are plotted versus time for July 18, 1974.

Figure 58. Sunlight current balance, quiet time. The current balance for ATS-6 is indicated with balancing vectors that include photoelectrons, ambient ions, ambient electrons, and engine generated ions.

Figure 59. ATS-6 spectrogram, October 19, 1974. Two hours of data at the time of the ion engine ignition. The pitch angle of the observed particles is again plotted above the data from the north-south detector.

Figure 60. ATS-6 potential measurement. The mainframe potential is plotted from 07:30 to 08:50 on October 19, 1974.

Figure 61. ATS-6 potential measurement. The differential charging barrier height is plotted from 07:30 to 08:10 on October 19, 1974.

Figure 62. ATS-6 warm ion angular distribution, October 19, 1974. The detector angle of the intense warm ion fluxes is plotted versus time from 07:40 to 08:10.

Figure 63. ATS-6 spectrogram, October 19, 1974. Energy angle spectrogram for data from the north-south detector from 08:45 to 10:00. The horizontal axis is the detector angle, the vertical axis is particle energy.

Figure 64. ATS-6 spectrogram, October 19 to 23, 1974. Data from the north-south detector for 4 1/2 days is given in standard format.

Figure 65. ATS-6 Quartz-crystal microbalance, June to December, 1974. Data from the OCM show the abrupt rise in accumulated mass during the ion engine operation from October 19 to 23 (days 292 to 296).

Figure 66. ATS-6 ion distribution function, October 20, 1974. Data from the north-south detector, at 02:19 UT.

Figure 67. ATS-6 spectrogram, July 20, 1974. Five hours of data from the north-south detector.

Figure 68. ATS-6 spectrogram, July 20, 1974. Two hours of data from the east-west and fixed ion detectors. The diagonal trace is the detector angle of the east-west detector. It looks parallel to the fixed detector at its maximum extent, antiparallel at its minimum.

Figure 69. ATS-6 Ion distribution functions, July 20, 1974. Four spectra are shown from the fixed detector. Times are 07:17, 07:23, 07:29, and 07:33.

Figure 70. ATS-6 count rates. Data from the fixed detector 5, 12, and 42 eV channels are plotted versus time, from 07:15 to 07:35 on July 20, 1974. The neutralizer probe voltage is plotted below the count rates.

Figure 71. ATS-6 spectrogram, July 21, 1974. Three hours of data from the east-west detectors, showing disappearance of photoelectrons during neutralizer ignitions.

Figure 72. ATS-6 electron distribution functions, July 21, 1974. Data from the east-west detector is plotted for three times, 02:43, 03:00, and 03:28. The first is for neutralizer off, the latter two for neutralizer on. The two 'on' curves overlap, and would match the 'off' curve if moved laterally 6 eV, the difference in potential energy.

Figure 73. ATS-6 potential plot, July 21, 1974. Spacecraft potential measurements made from the electron data, plotted with the neutralizer probe voltage. Drops in the spacecraft potential occur when the probe voltage indicates the neutralizer is entering spot mode.

Figure 74. ATS-6 spectrogram, October 14, 1976. Two hours of data around local midnight, with an eclipse of the spacecraft from 04:10 to 04:30. The eclipse and neutralizer operation(03:57 to 04:21) cause the appearance of intense low energy ion fluxes, and the intensity scale cycles to black.

Figure 75. Eclipse current balance, quiet time. A rough vector display of the principal current contributions to the spacecraft balance on October 14, 1976. The terms included are ambient ions and electrons, and ions from the neutralizer.

Figure 76. ATS-6 spectrogram, September 2, 1976. Two hours of data from a neutralizer operation during eclipse entry. Eclipse is from 00:20 to 00:52, the neutralizer is in spot mode from 00:03 to 00:30. The spacecraft charges negatively following the neutralizer 'off' command.

Figure 77. ATS-6 potential plot, April 7, 1977. The spacecraft potential, neutralizer probe voltage, and solar array

bus current are plotted versus time, from 09:00 to 09:50. The solar array current shows the eclipse period, the probe voltage the neutralizer status. The spacecraft discharges while the neutralizer is in plume mode.

Figure 78. ATS-6 spectrogram, September 18, 1974. Data from the north-south detector are plotted, with field aligned structure indicated by periodic variations in the low energy ion data. The spacecraft is eclipsed from 05:35 to 06:45, causing an intensification in the ion fluxes, and a drop in the low energy electron fluxes because of a shift in spacecraft potential. An injection of hot plasma is visible at 08:00 in both the electron and ion data.

Figure 79. ATS-6 warm ion angular distribution, September 18, 1974. Data from the north-south ion detector 5 eV channel is plotted versus the pitch angle of the observed particles for the time period 05:40 to 06:35.

Figure 80. ATS-6 ion distribution functions, September 18, 1974. Data from eclipses, 06:39, and sunlight, 06:44 are plotted. The pitch angle at these times is 14 degrees. The solid line is an interactive fit of multiple ion species streaming at a velocity of 32 km/s. Other parameters in the fit are:

species	density	temperature
H+	18.5	1.0
He+	0.1	1.8
O++	0.2	7.0
O+	0.1	3.0

Figure 81. ATS-6 Ion distribution functions, September 18, 1974. Three plots from the north-south detector data, all at 15 degrees pitch angle. Streaming velocities start at 35 km/s and increase through 38 km/s to 45 km/s. Parameters are:

time	species	density	temperature
07:37:49	H+	9.4	1.8
	He+	0.3	1.0
	O++	1.6	2.0
	O+	0.2	11.0
07:41:25	H+	20.0	1.8
	He+	0.4	1.5
	O++	0.4	4.0
	O+	0.15	10.0
07:48:13	H+	18.0	2.0
	He+	0.4	1.5
	O++	0.5	4.6
	O+	0.15	10.2

Figure 82. ATS-6 Ion distribution functions, September 18, 1974. Plot of data from north-south detector measuring 13 degree pitch angle particles, with components of fits plotted. The stream velocity is 50 km/s, and the individual parameters are:

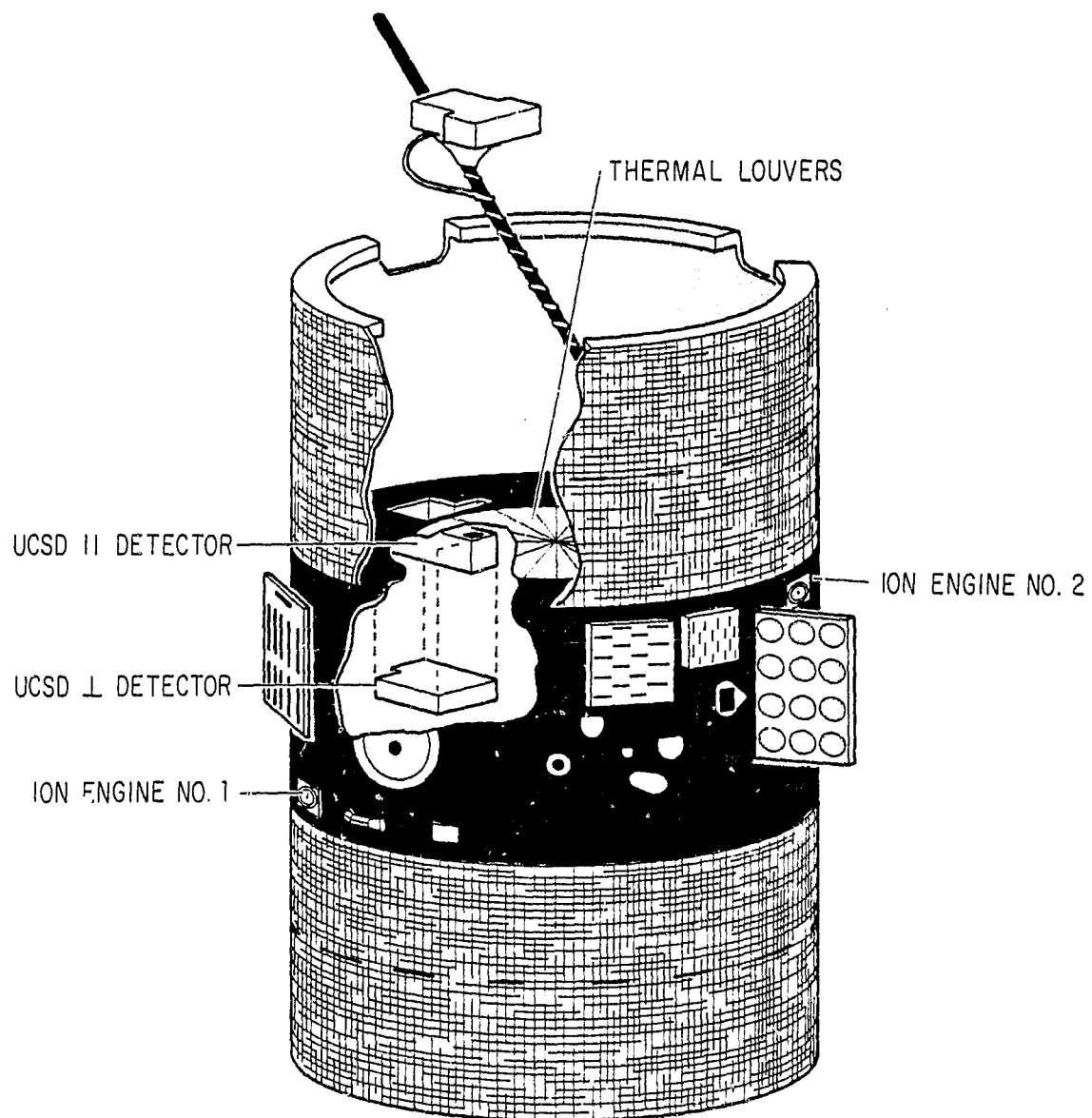
species	density	temperature
H+	1.1	1.3
He+	0.7	4.0
O++	1.1	6.0
O+	0.2	20.0

Figure 83. ATS-6 Ion distribution function, September 18, 1974. Data from the north-south detector at 14 degree pitch angle. A large streaming velocity of 150 km/s is found in the fit. Parameters are:

species	density	temperature
H+	0.61	5.0
He+	0.11	9.72
O++	1.21	27.0
O+	0.56	27.0

Figure 84. ATS-6 spectrogram, October 8, 1974. Data from the north-south detector for hours 0 to 8. The spacecraft is eclipsed from 05:35 to 06:32, and a bright band of ions appears at this time. The electrons fade due to the shift in potential and absence of photoelectrons.

Figure 85. ATS-6 ion angular distribution, October 8, 1974. Data from the north-south detector 5 eV (ch. 2) and 8 eV (ch. 3) are plotted versus north-south detector angle.



ATS-5 SPACECRAFT

79C0-6-004

ORIGINAL PAGE 1
OF FOUR

FIGURE 1

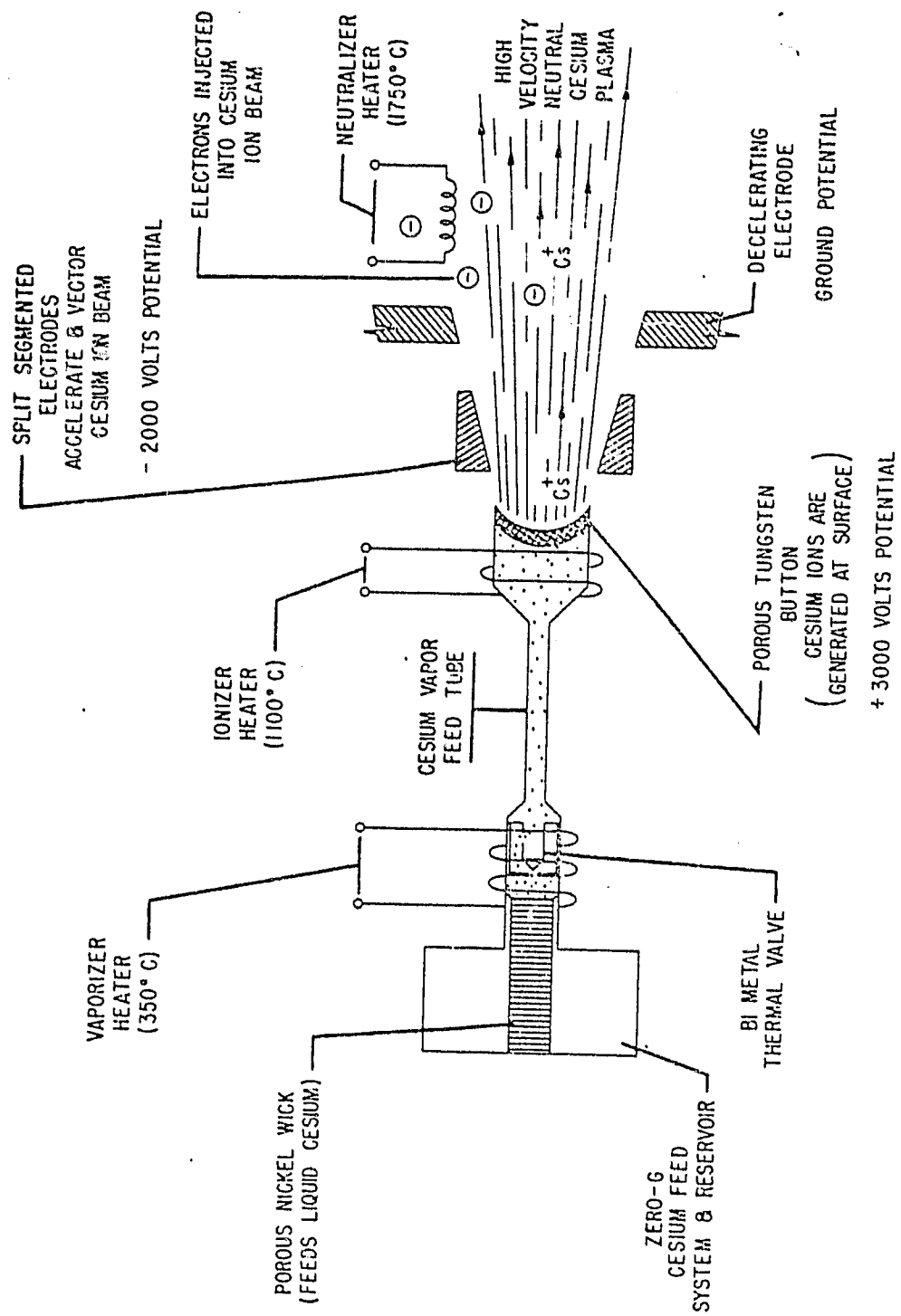


FIGURE 2

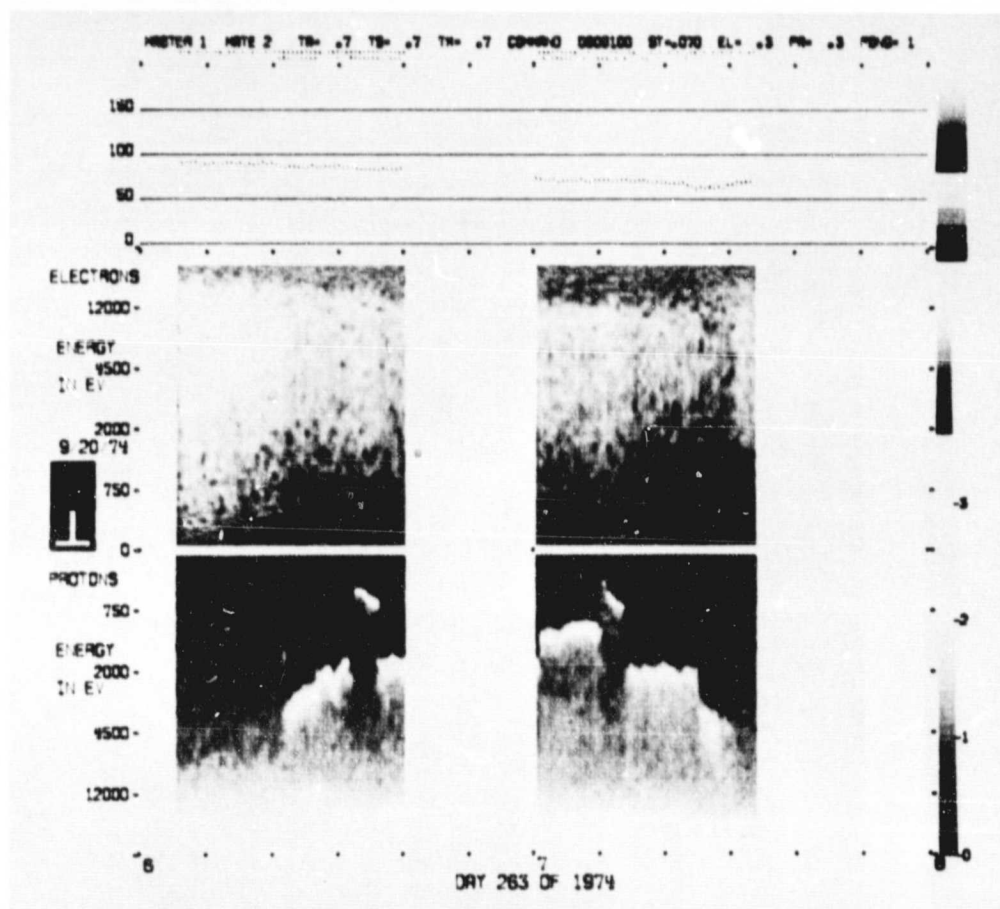


FIGURE 4

ORIGINAL PAGE IS
OF POOR QUALITY

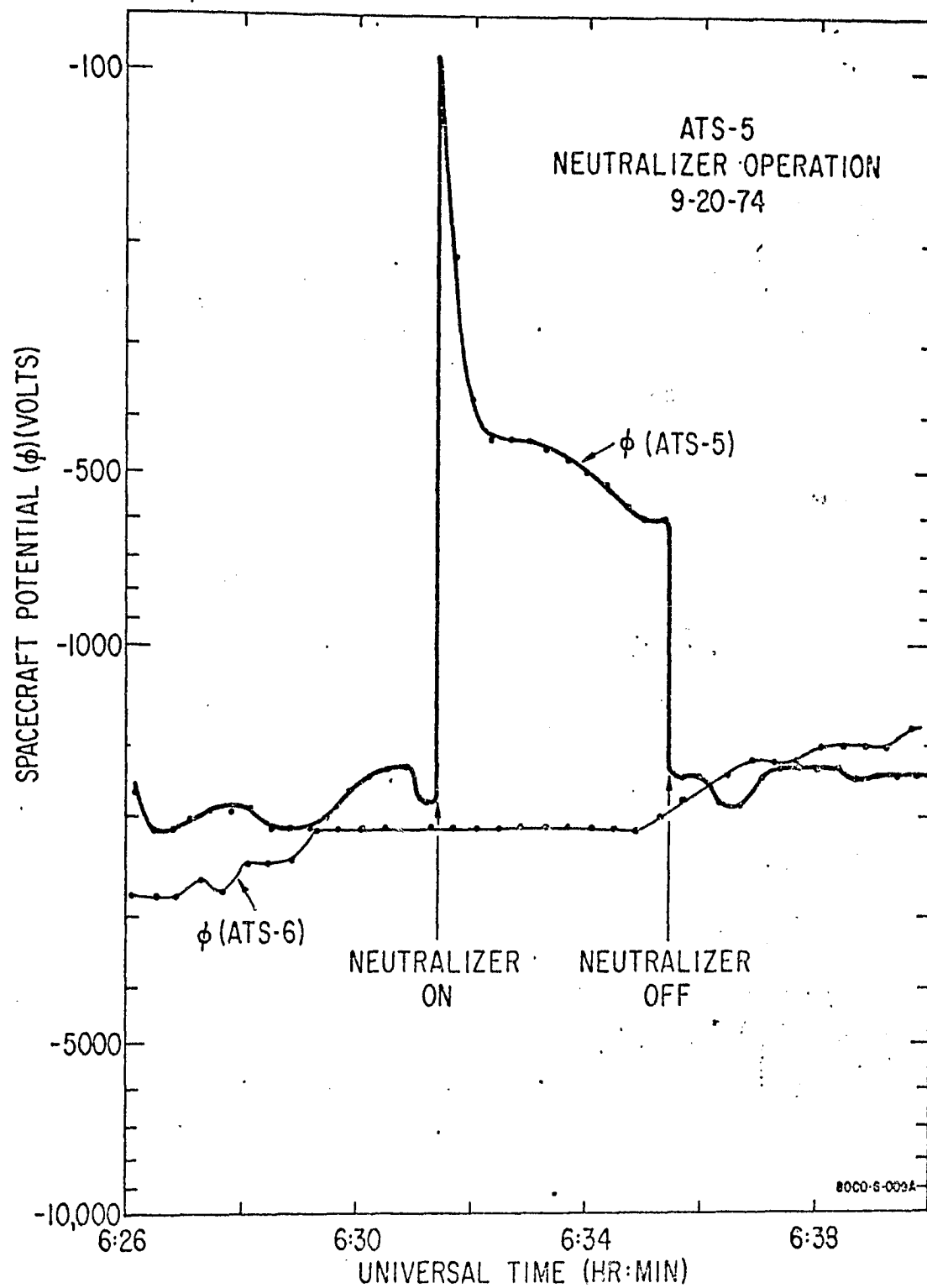


FIGURE 6

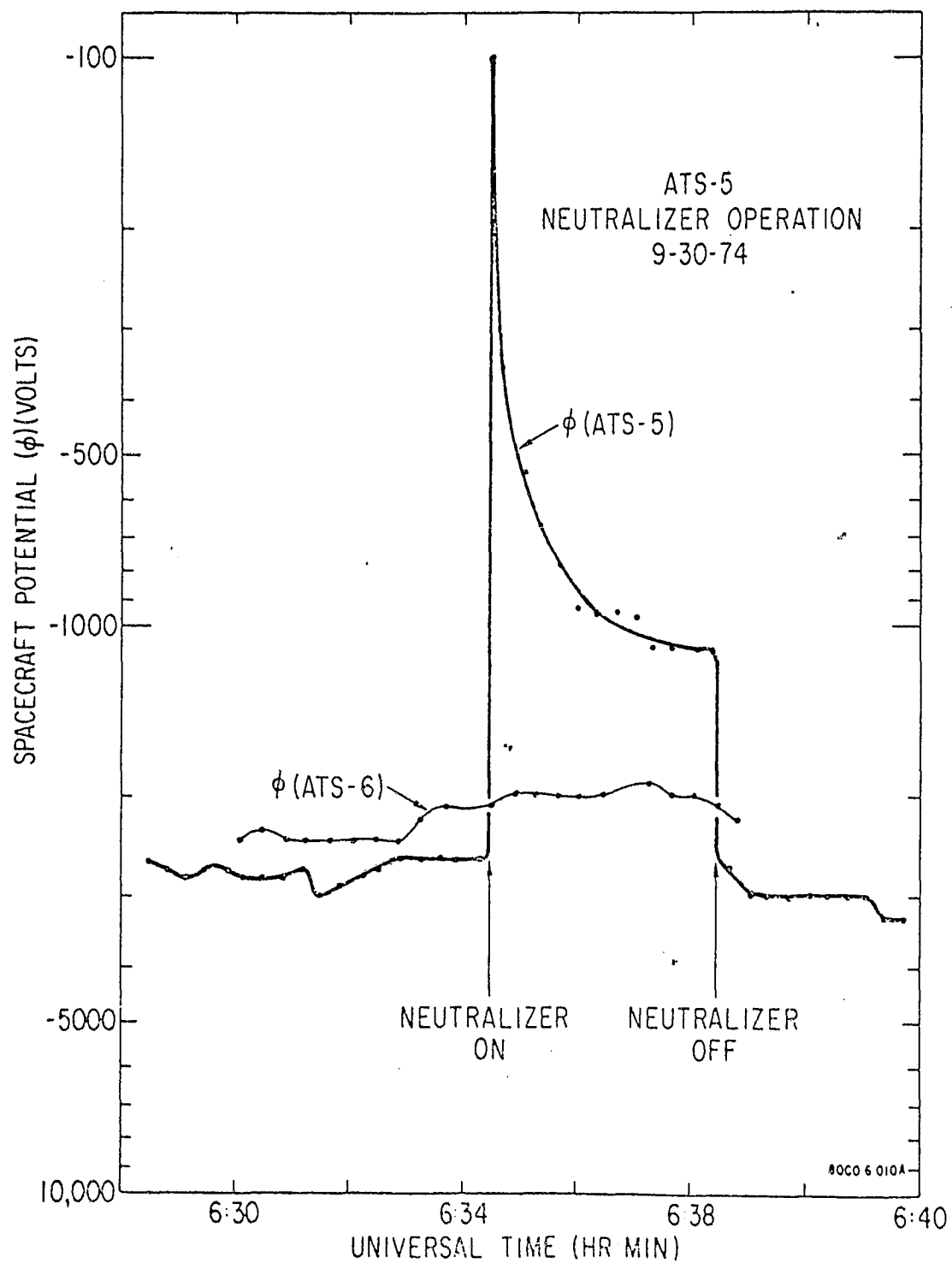


FIGURE 7

ATS-5 NEUTRALIZER / ECLIPSE OPERATION
3-28-78

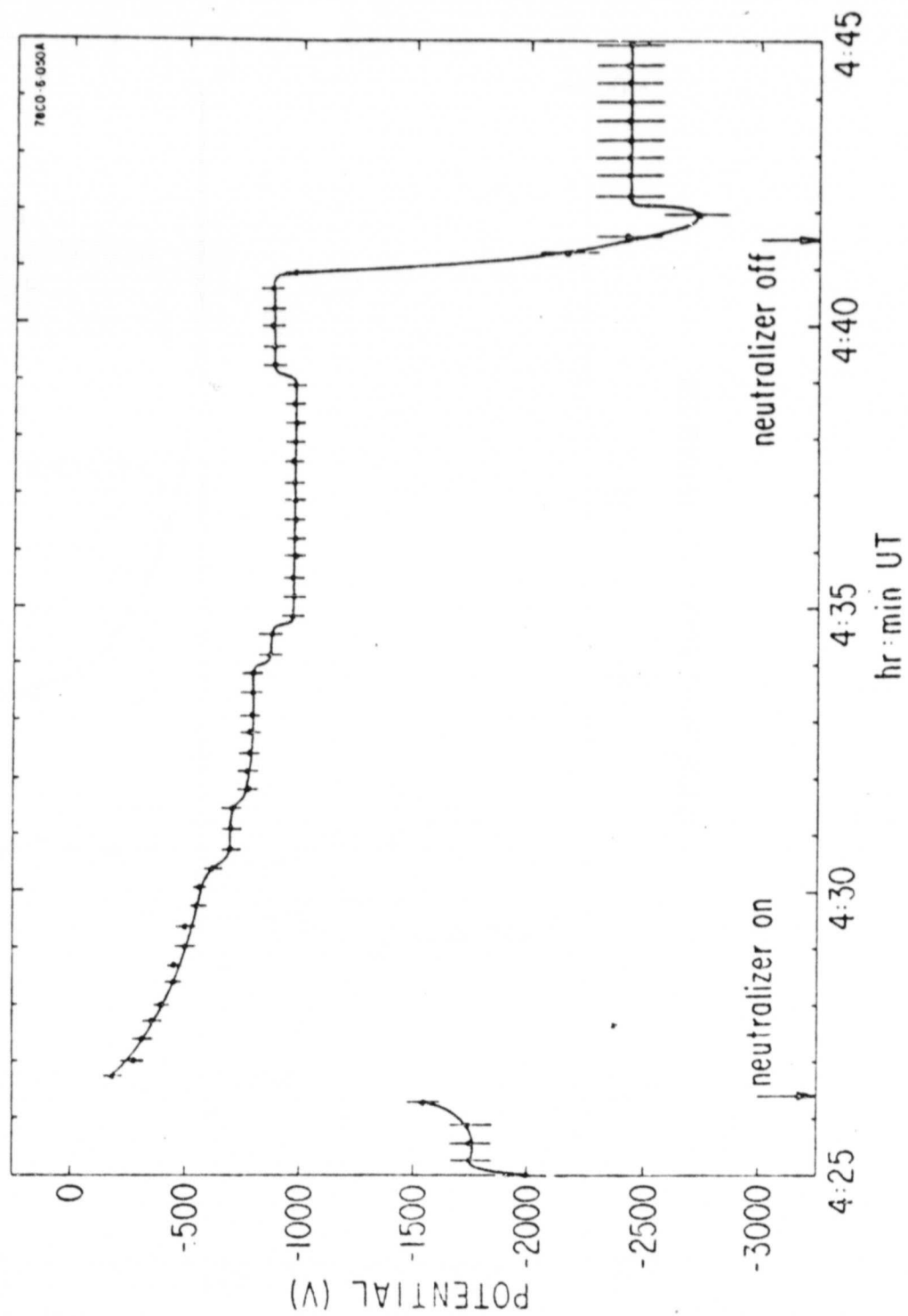


FIGURE 8

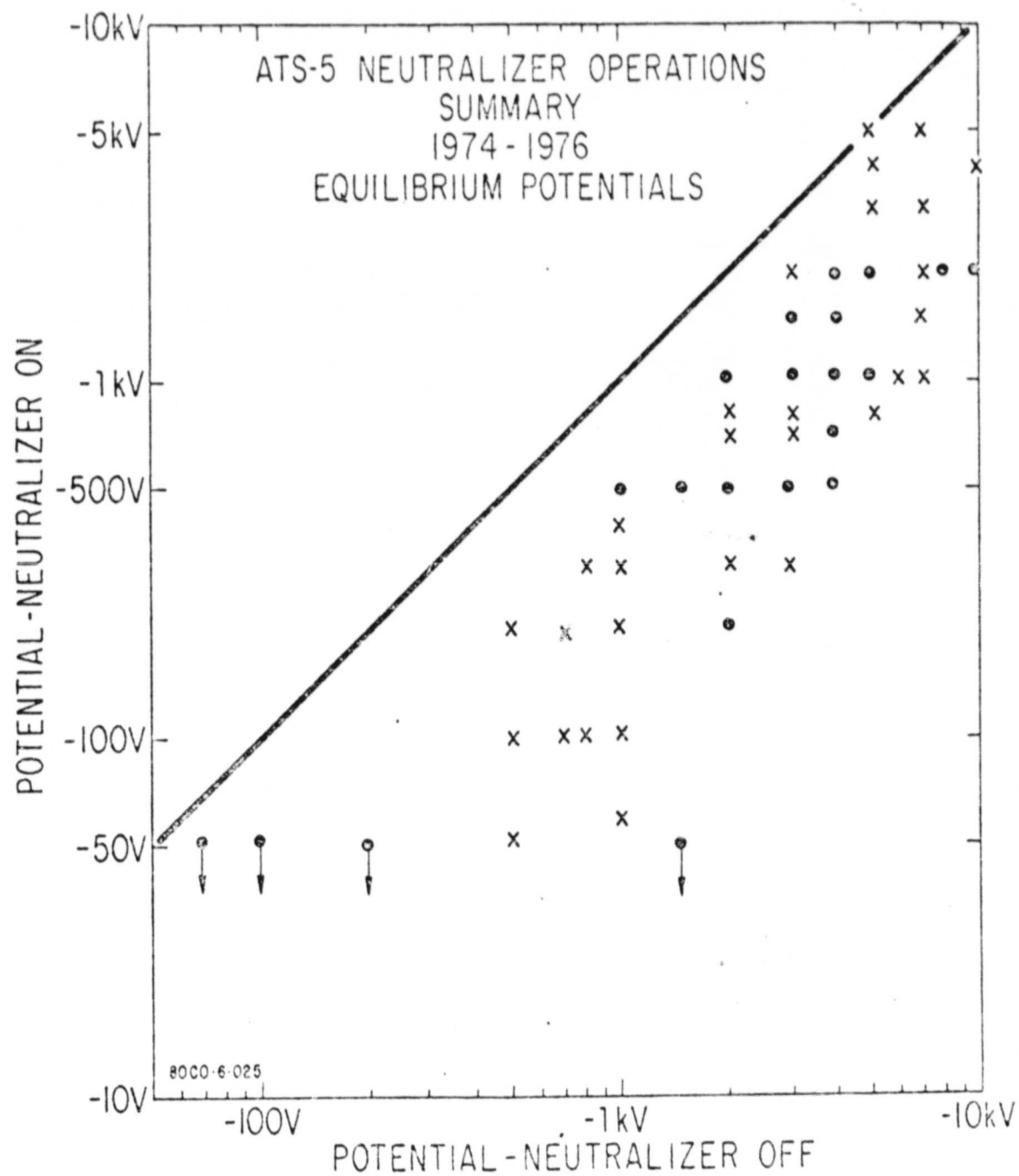


FIGURE 9

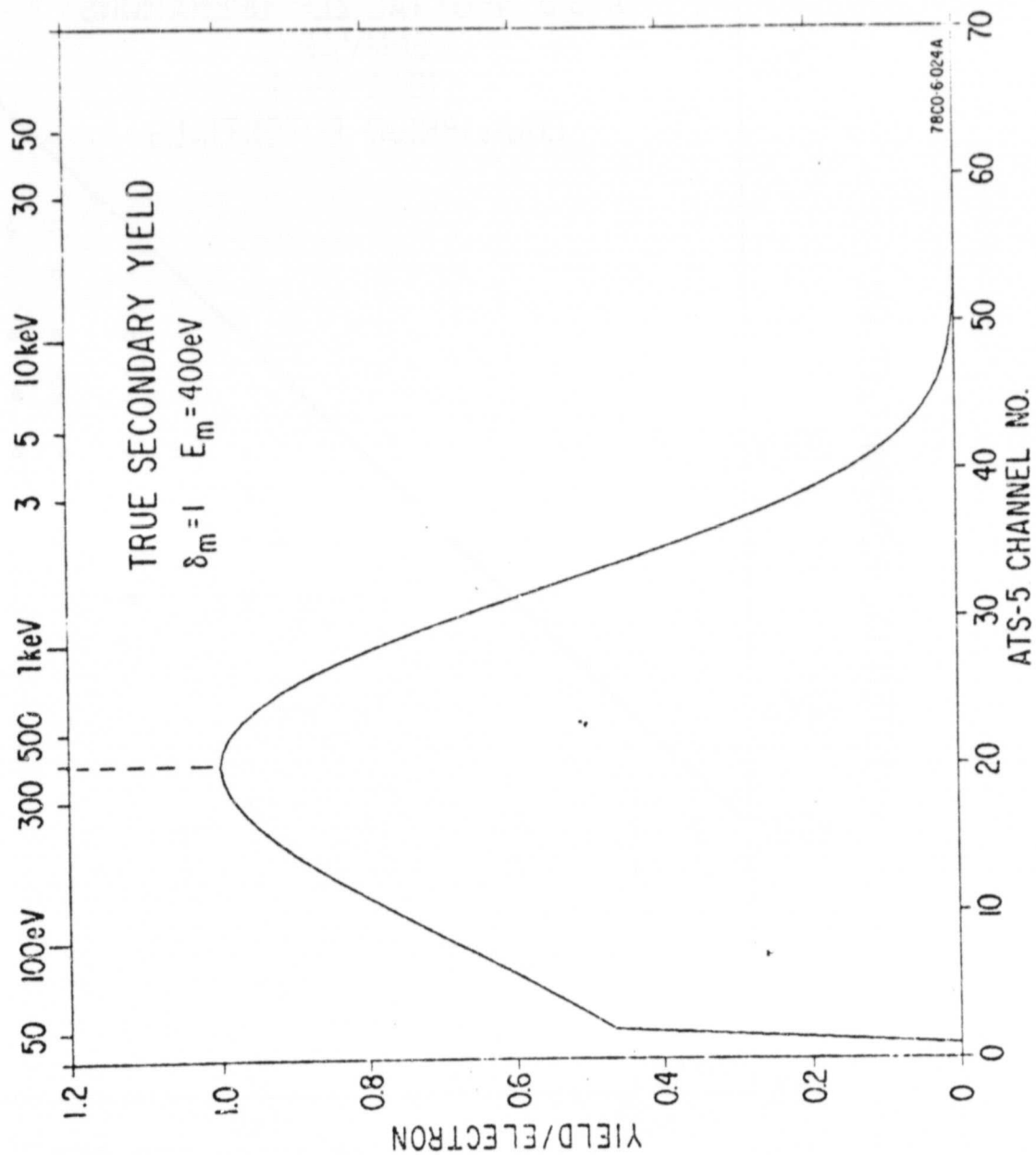


FIGURE 10

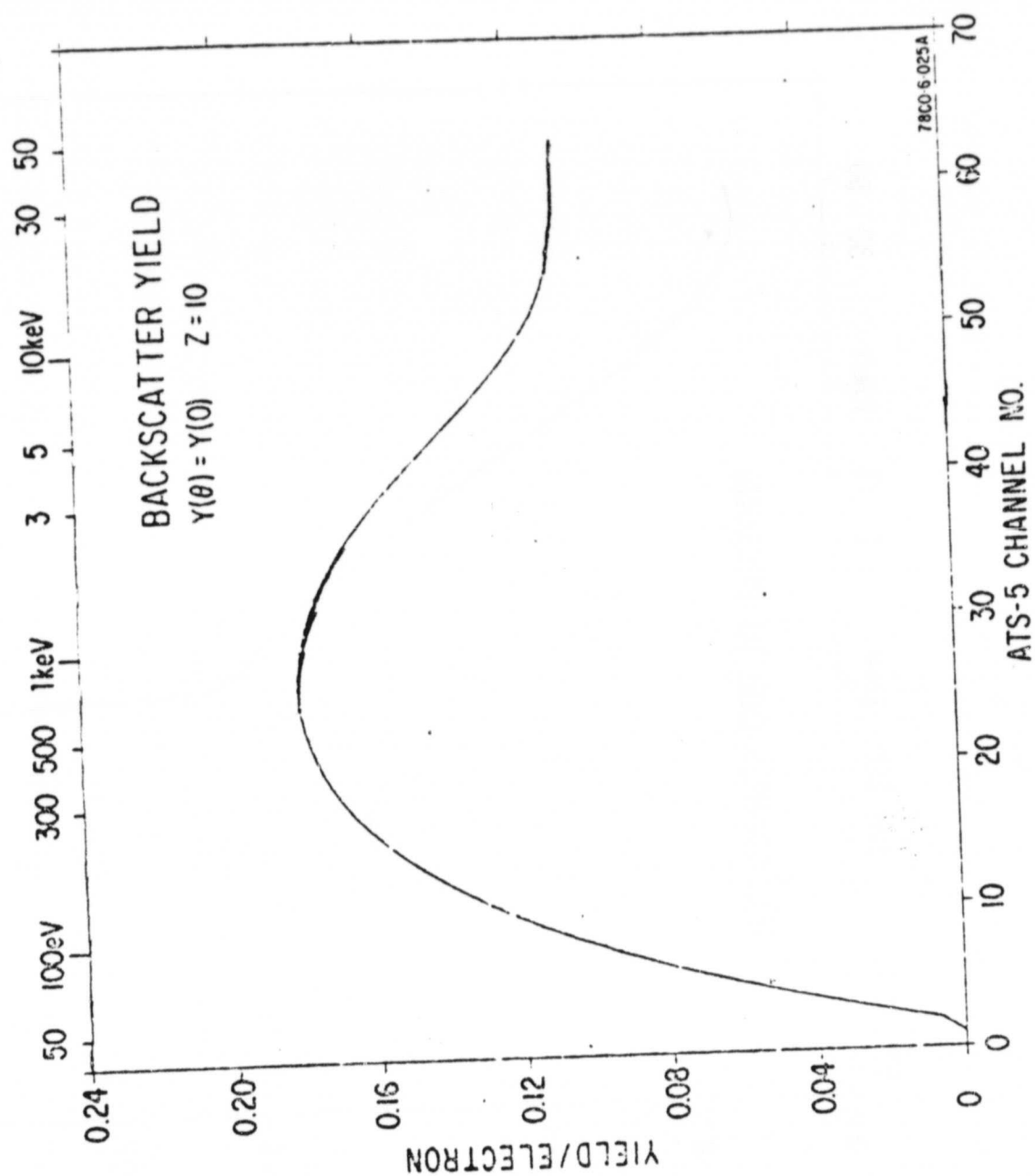


FIGURE 11

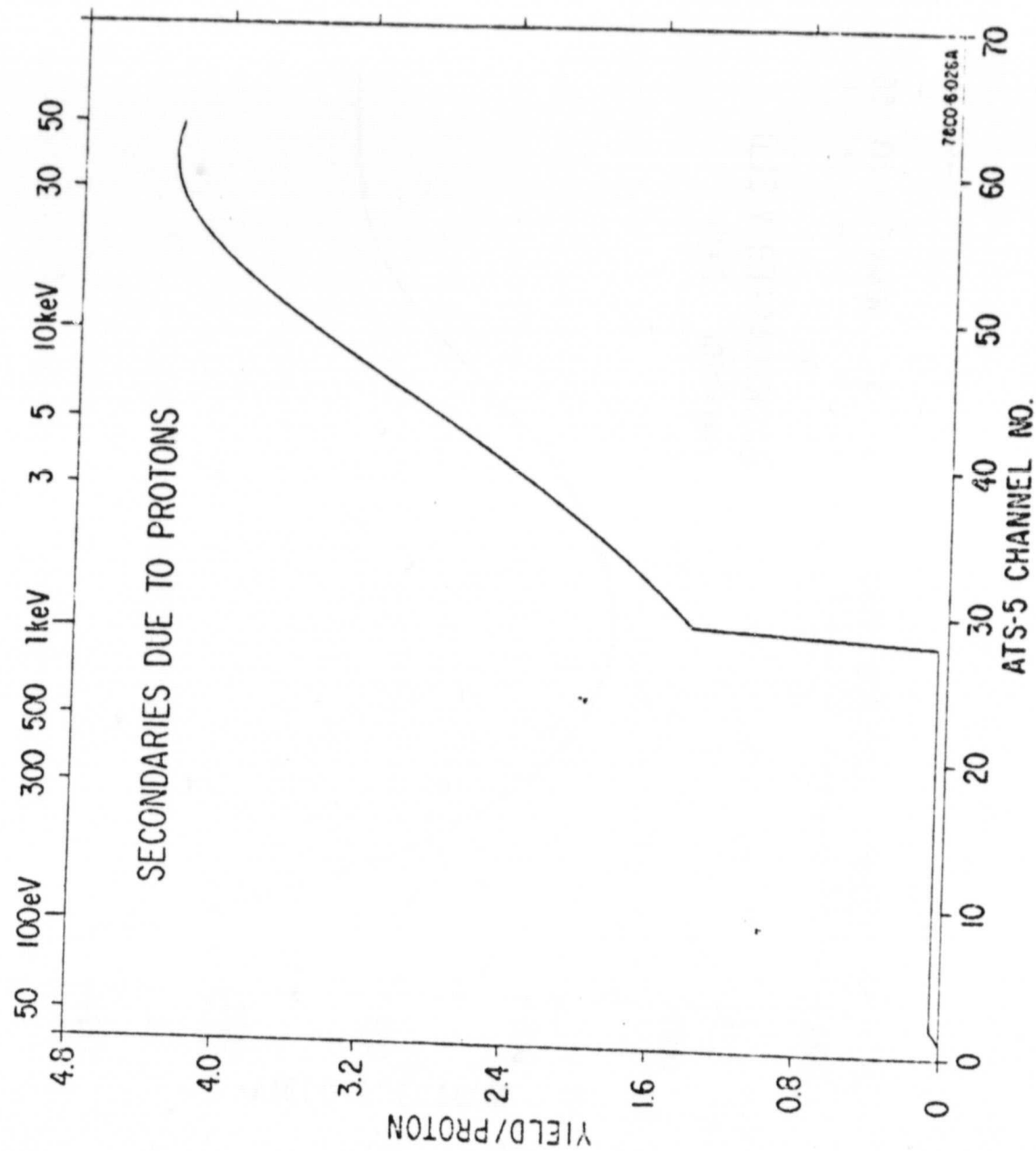


FIGURE 12

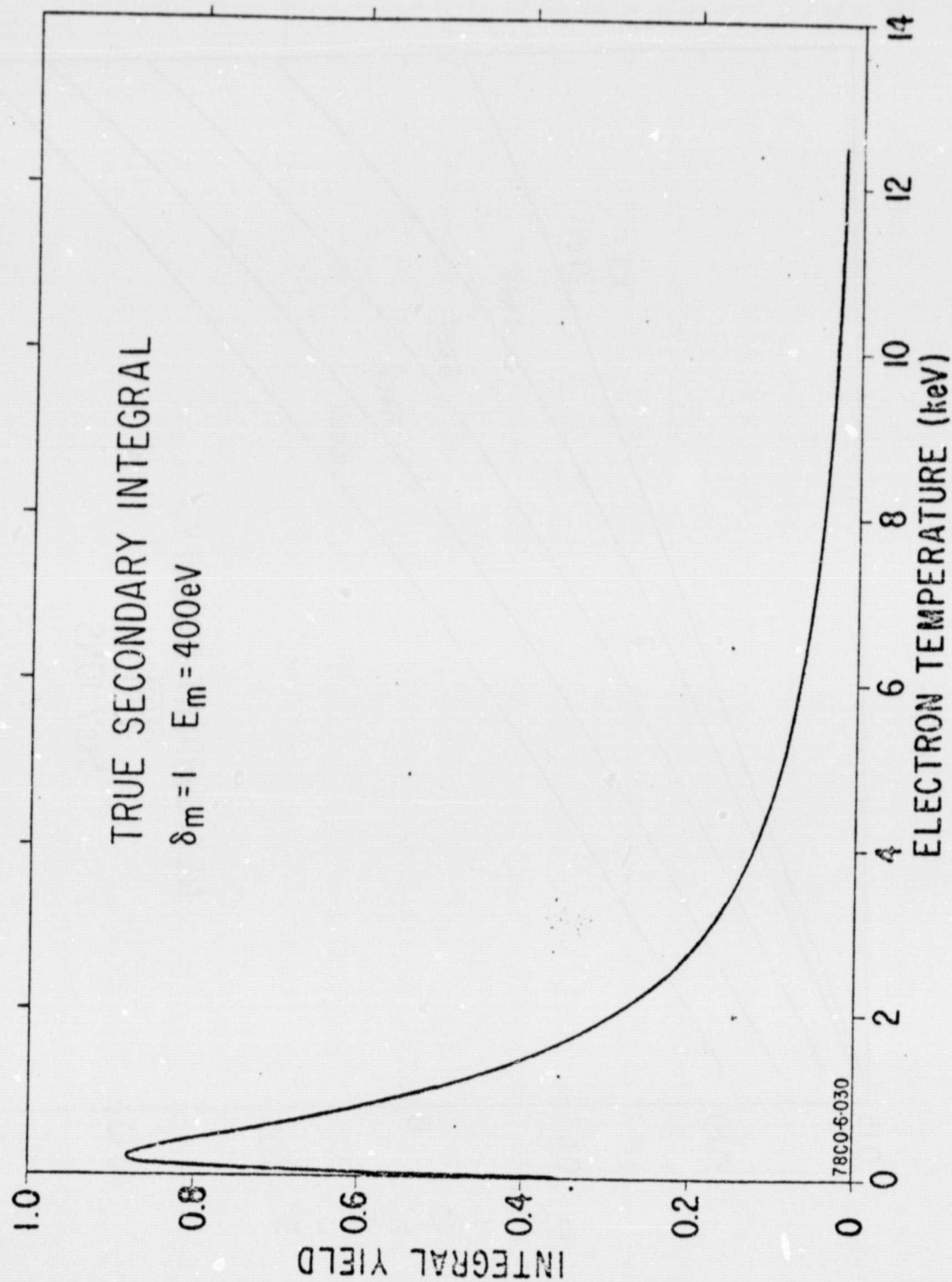


FIGURE 13

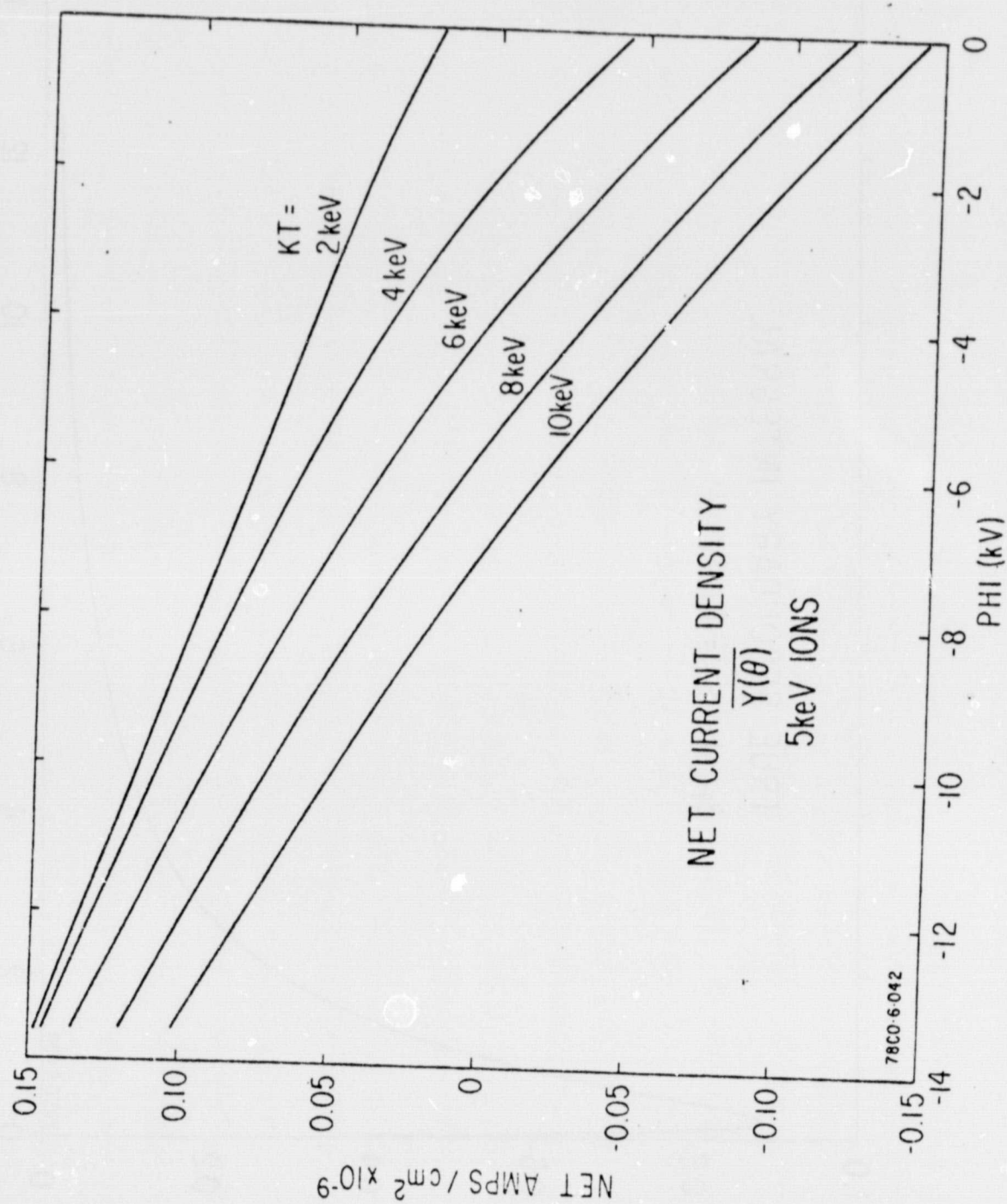
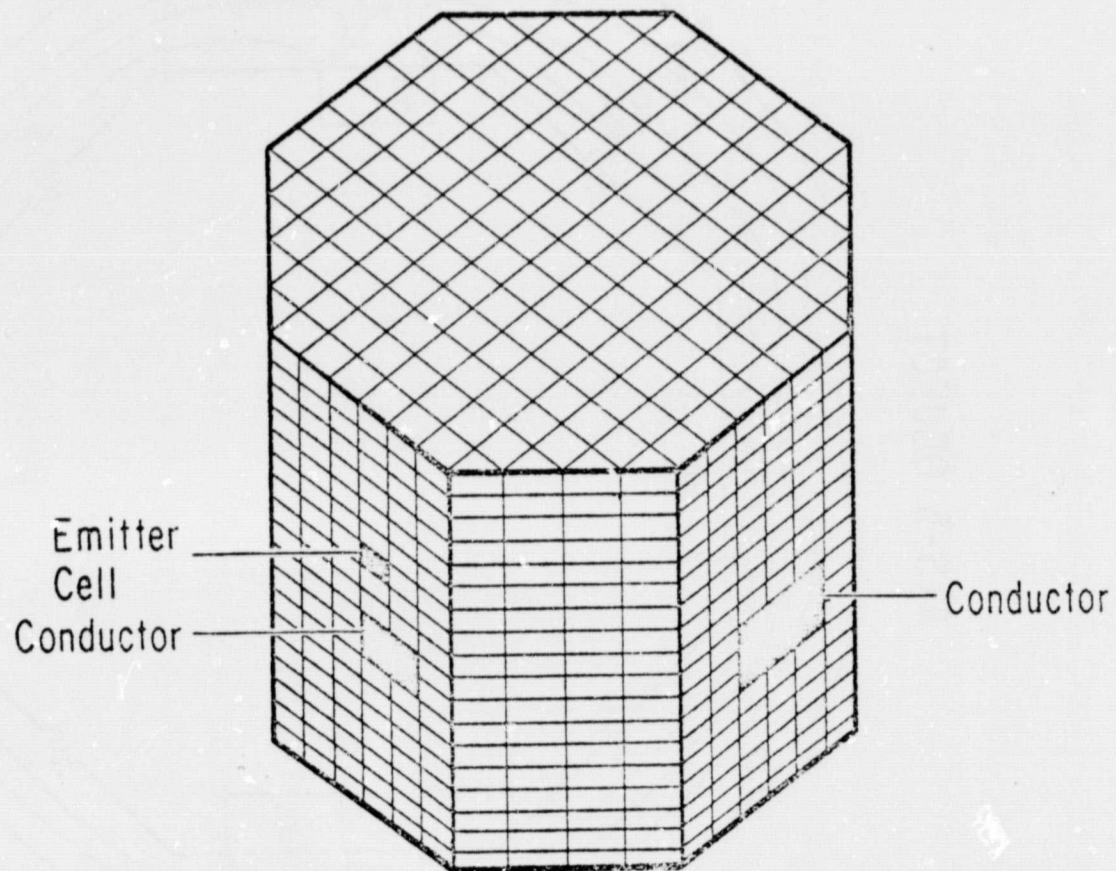


FIGURE 14

NASCAP / ATS-5 MODEL OBJECT

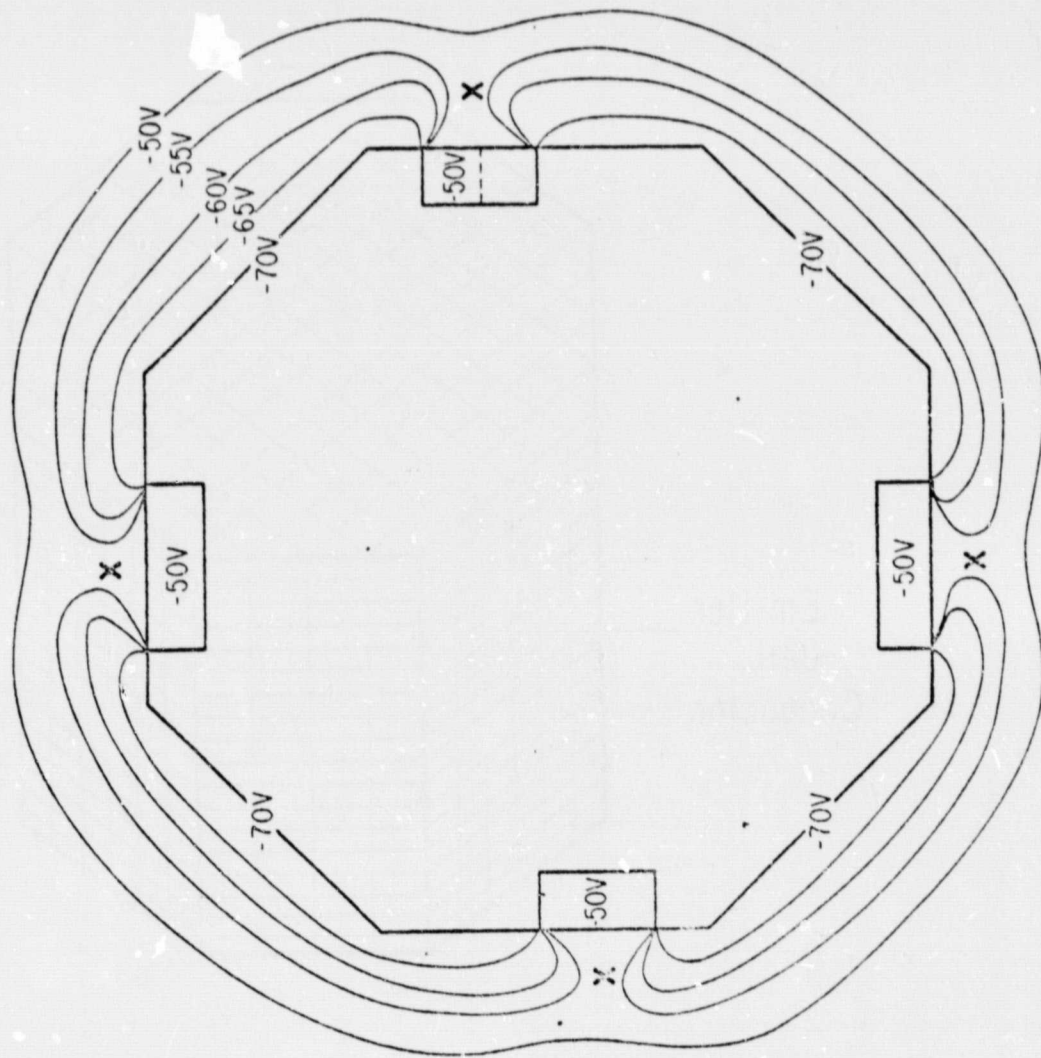


8000-6-032

ORIGINAL PAGE IS
OF POOR QUALITY

FIGURE 15

ATS-5 OBJECT



$\phi_{S/C} = -50V$
 $\phi_{S/A} = -70V$
 $V_{BARRIER} = 3V$
 $X = -53V$

8000 6 003

FIGURE 16

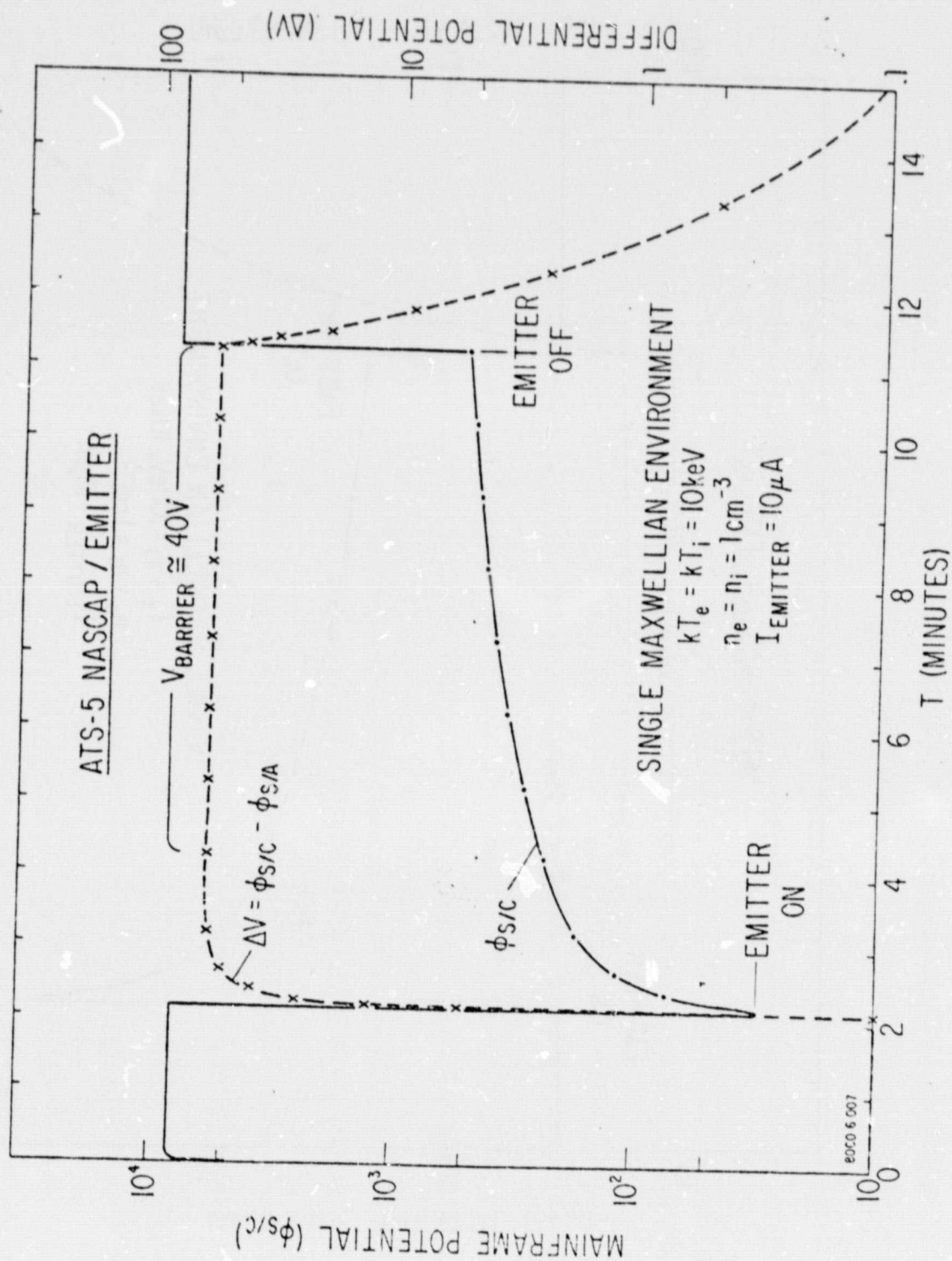


FIGURE 17

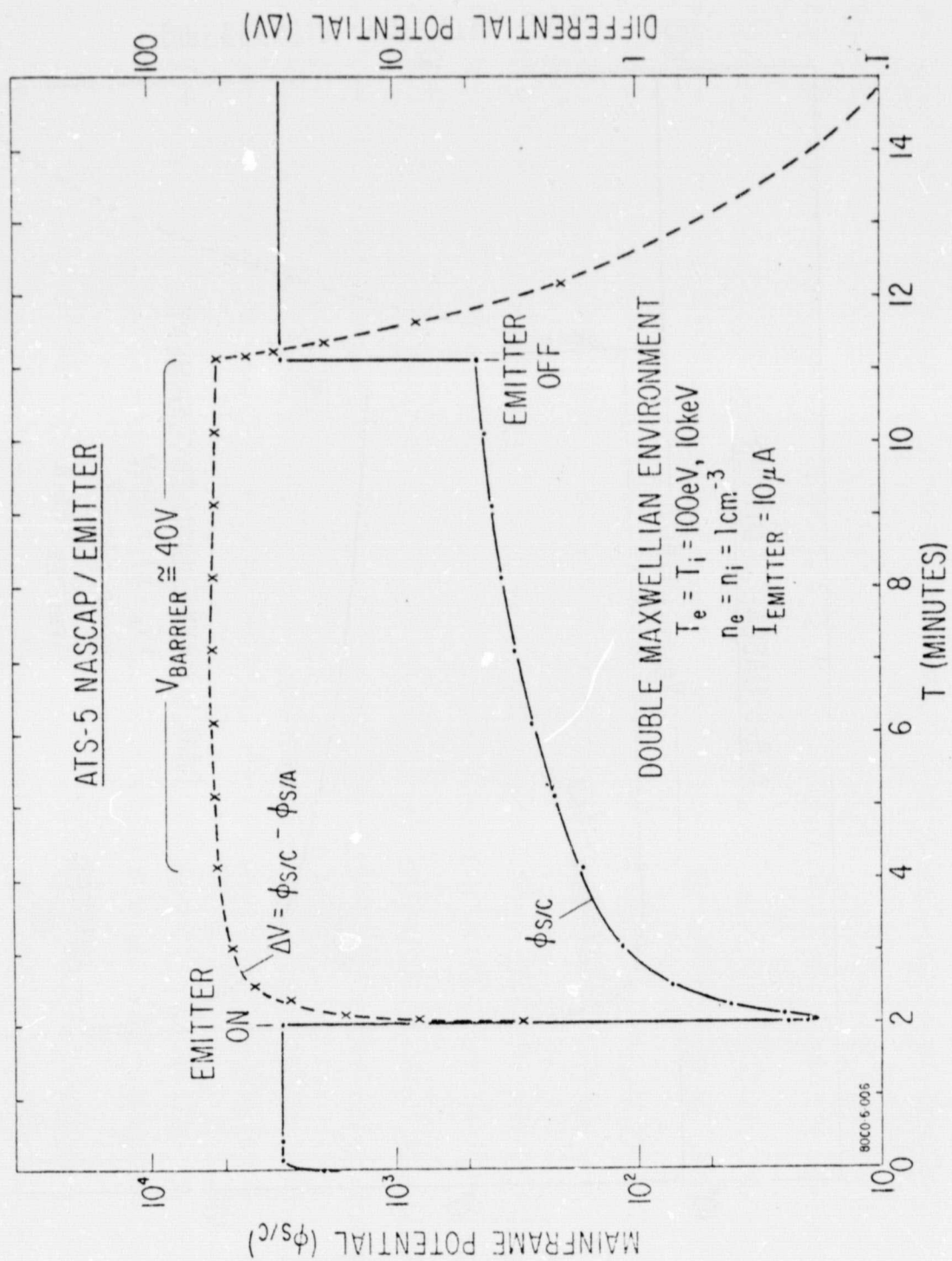


FIGURE 18

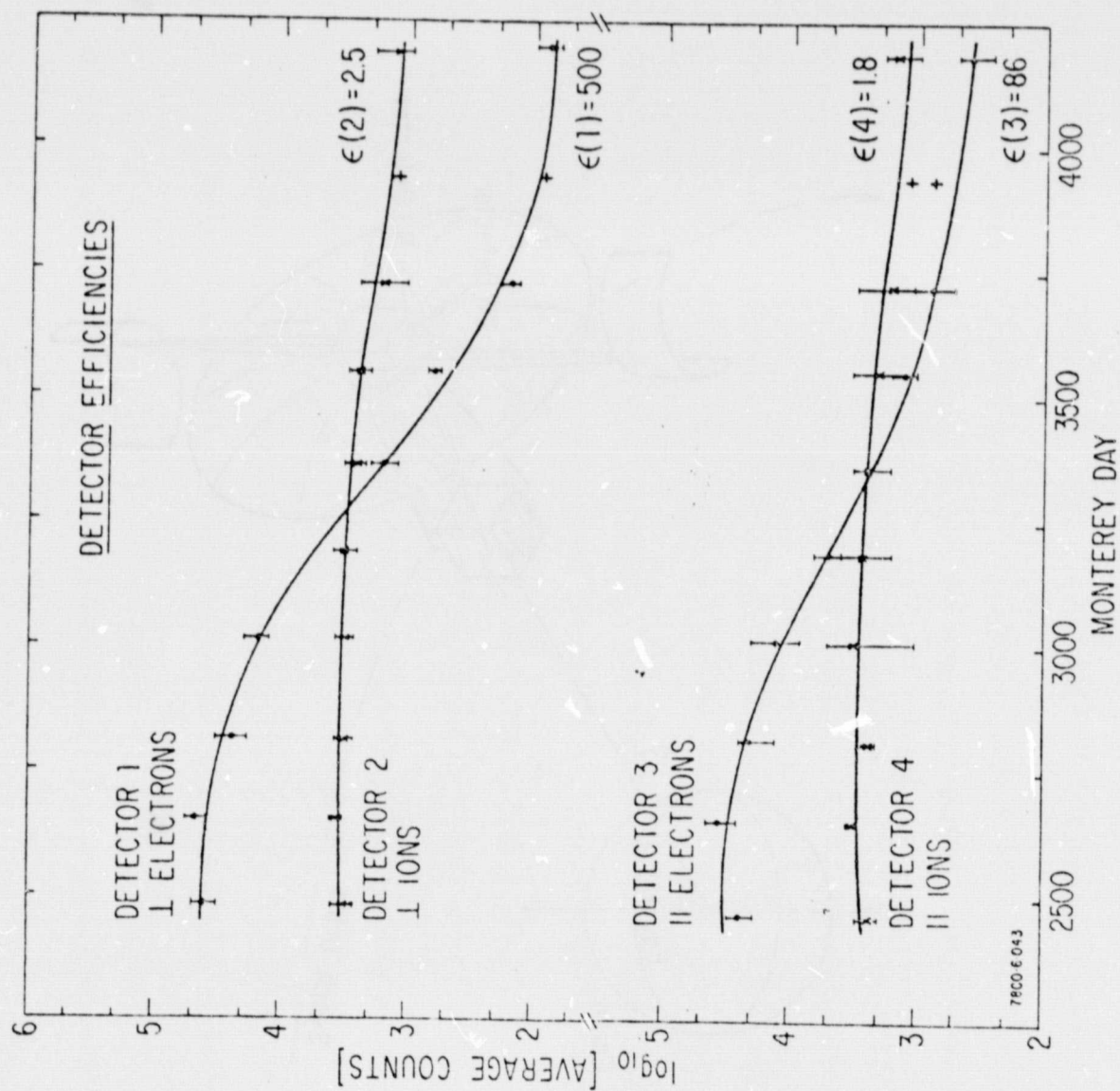


FIGURE 19

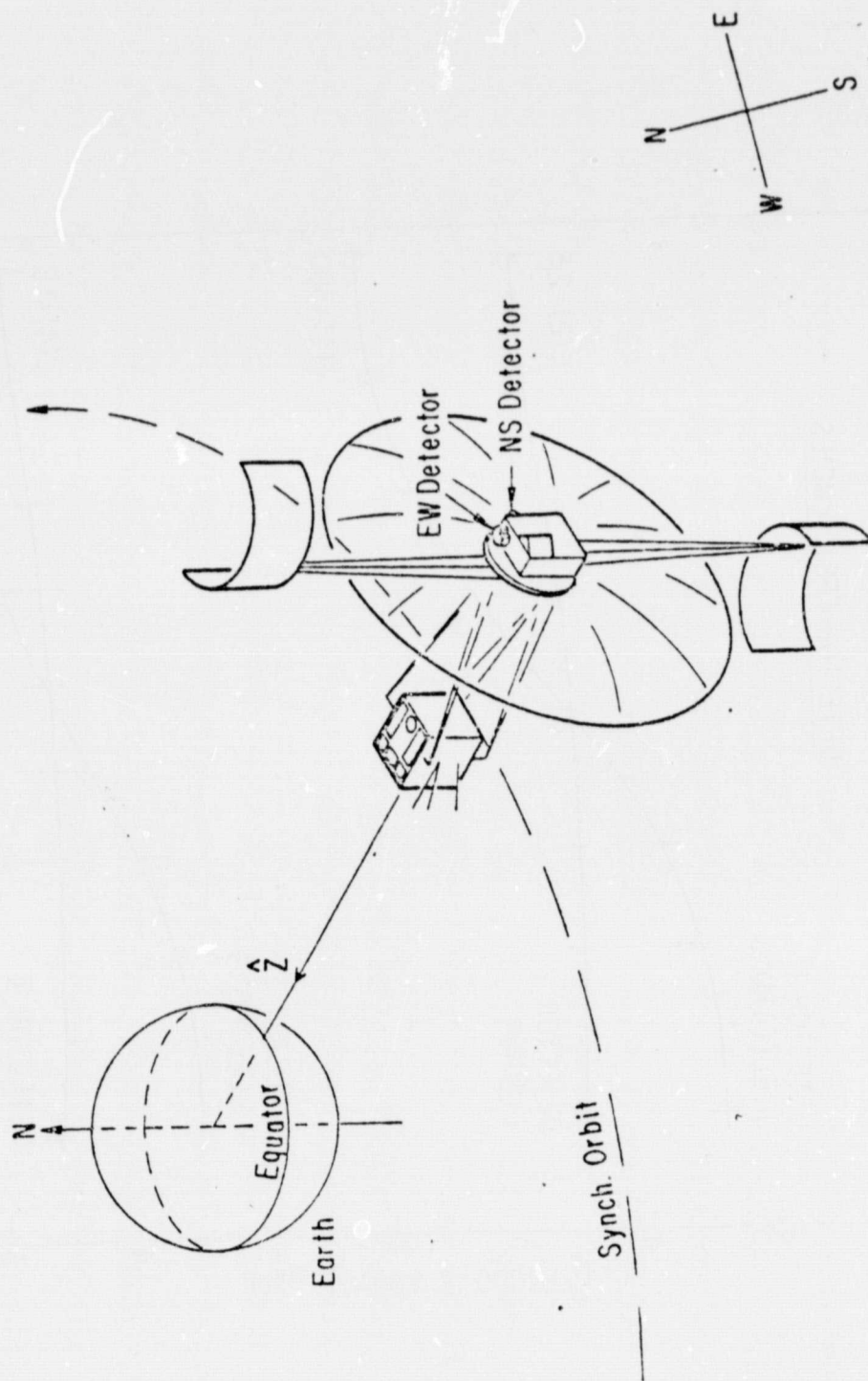


FIGURE 20

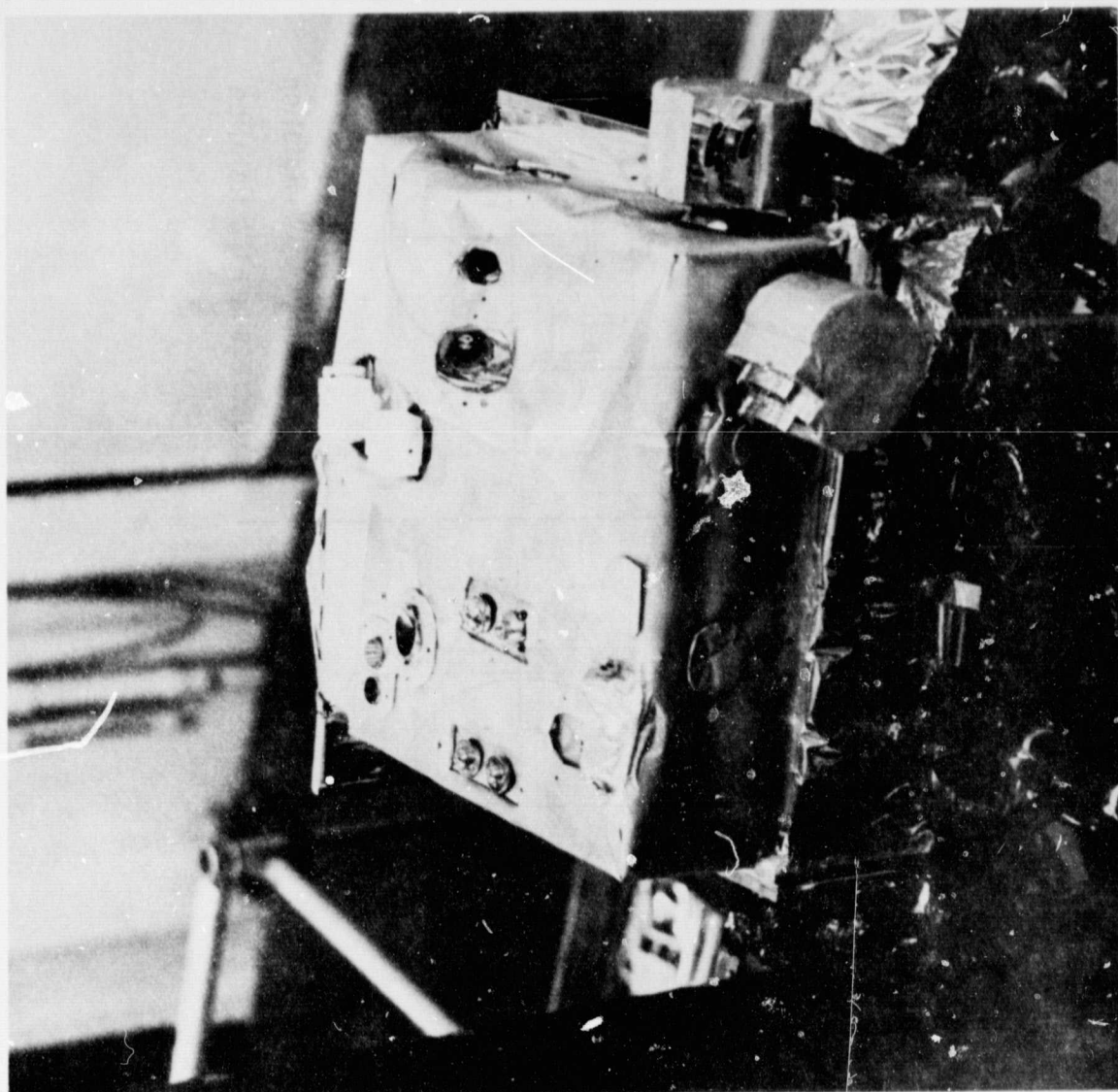


FIGURE 21

ORIGINAL PAGE IS
OF POOR QUALITY

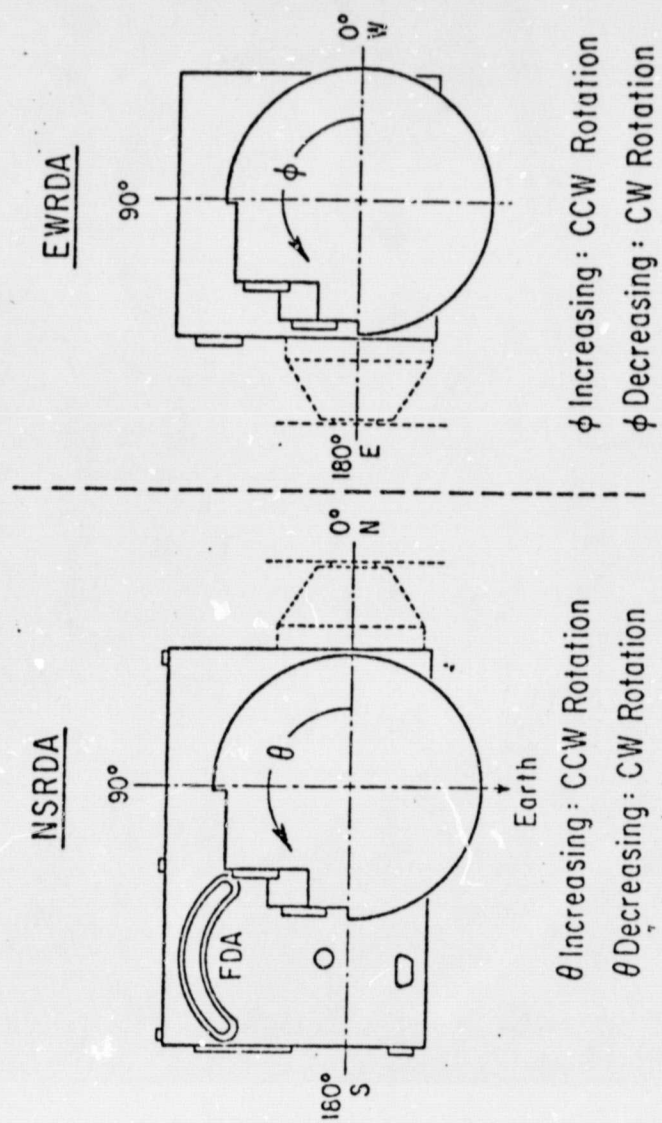


FIGURE 22

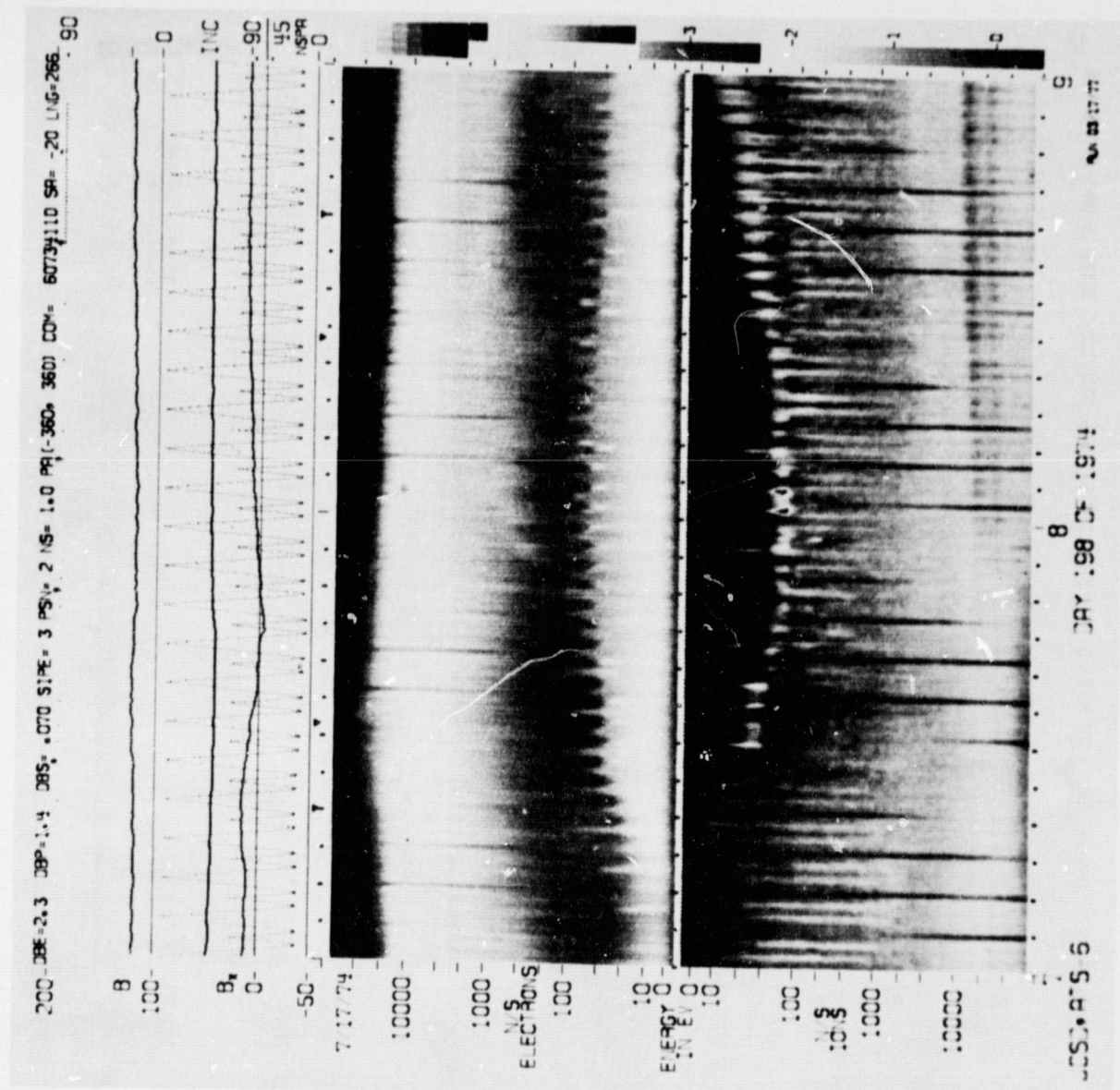


FIGURE 23

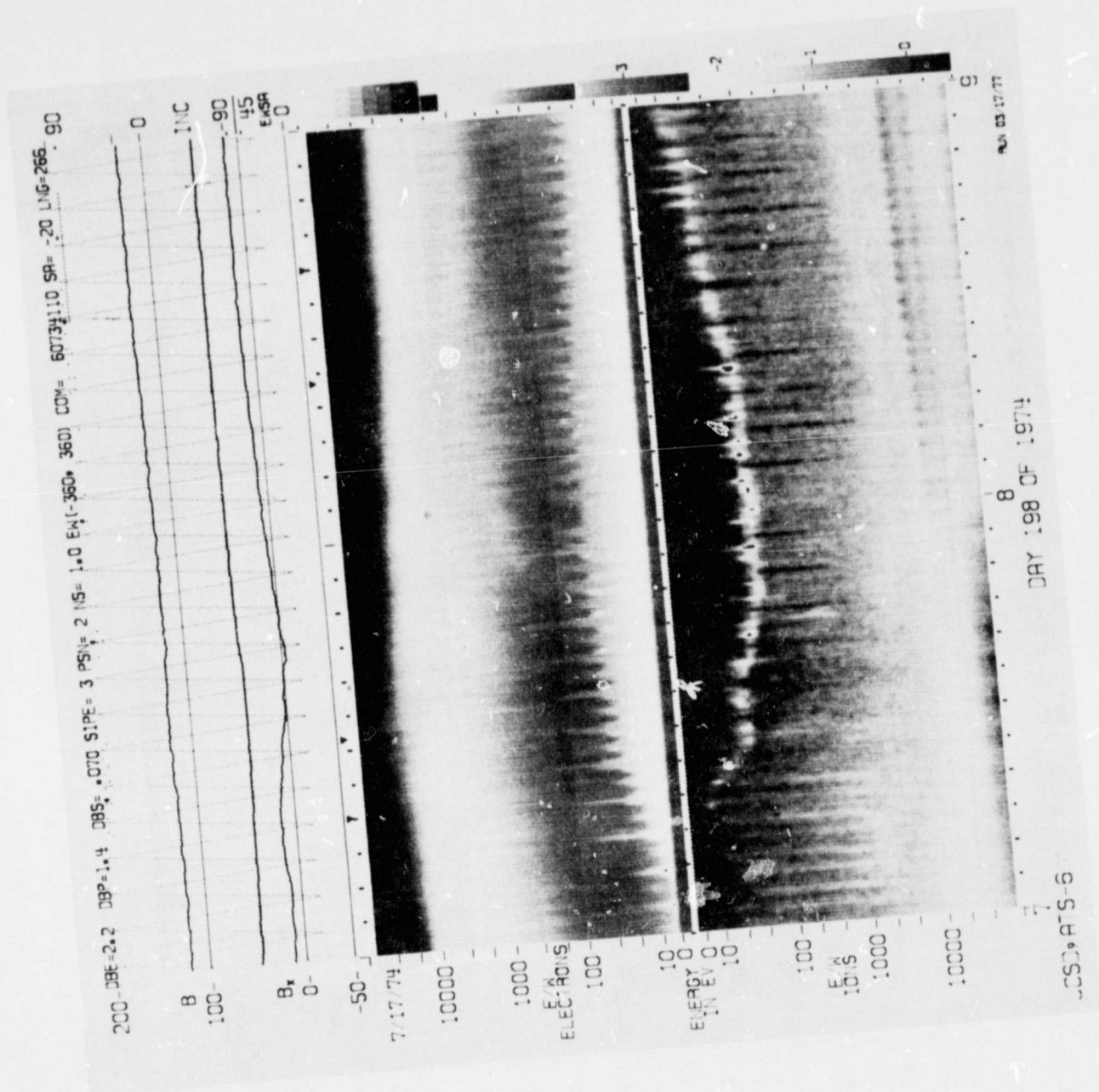


FIGURE 24

ORIGINAL PAGE IS
OF POOR QUALITY

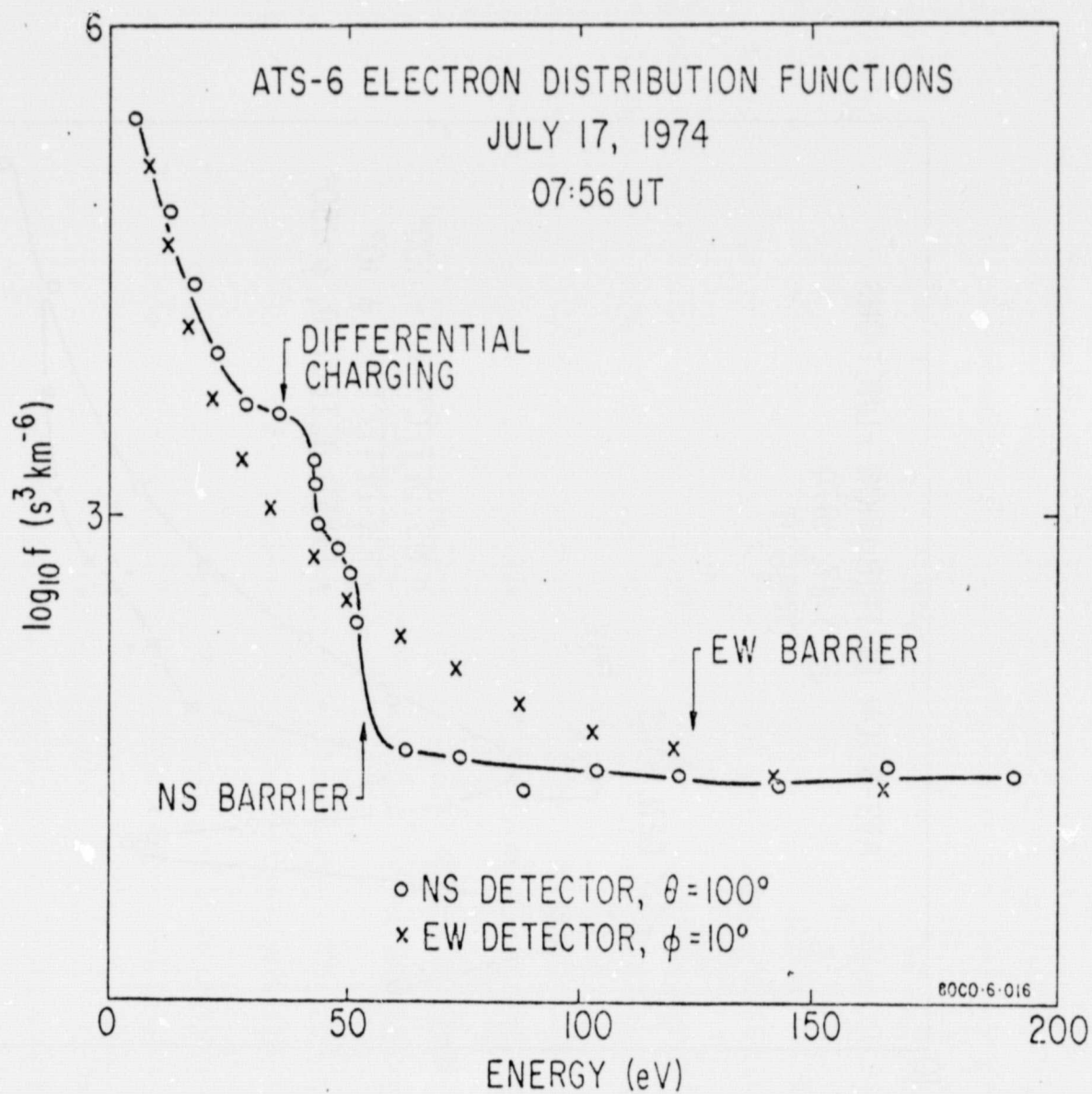


FIGURE 25

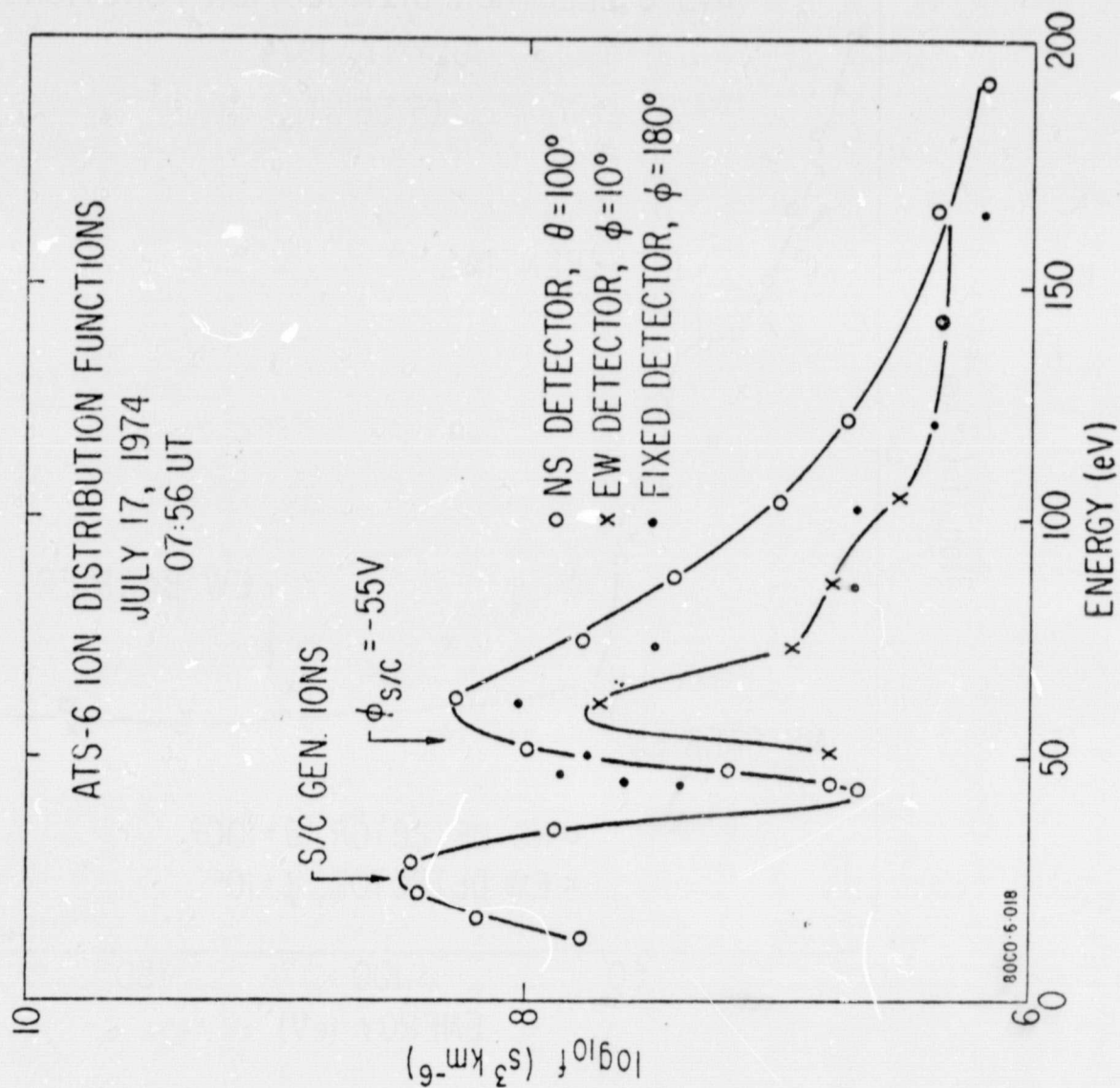


FIGURE 26

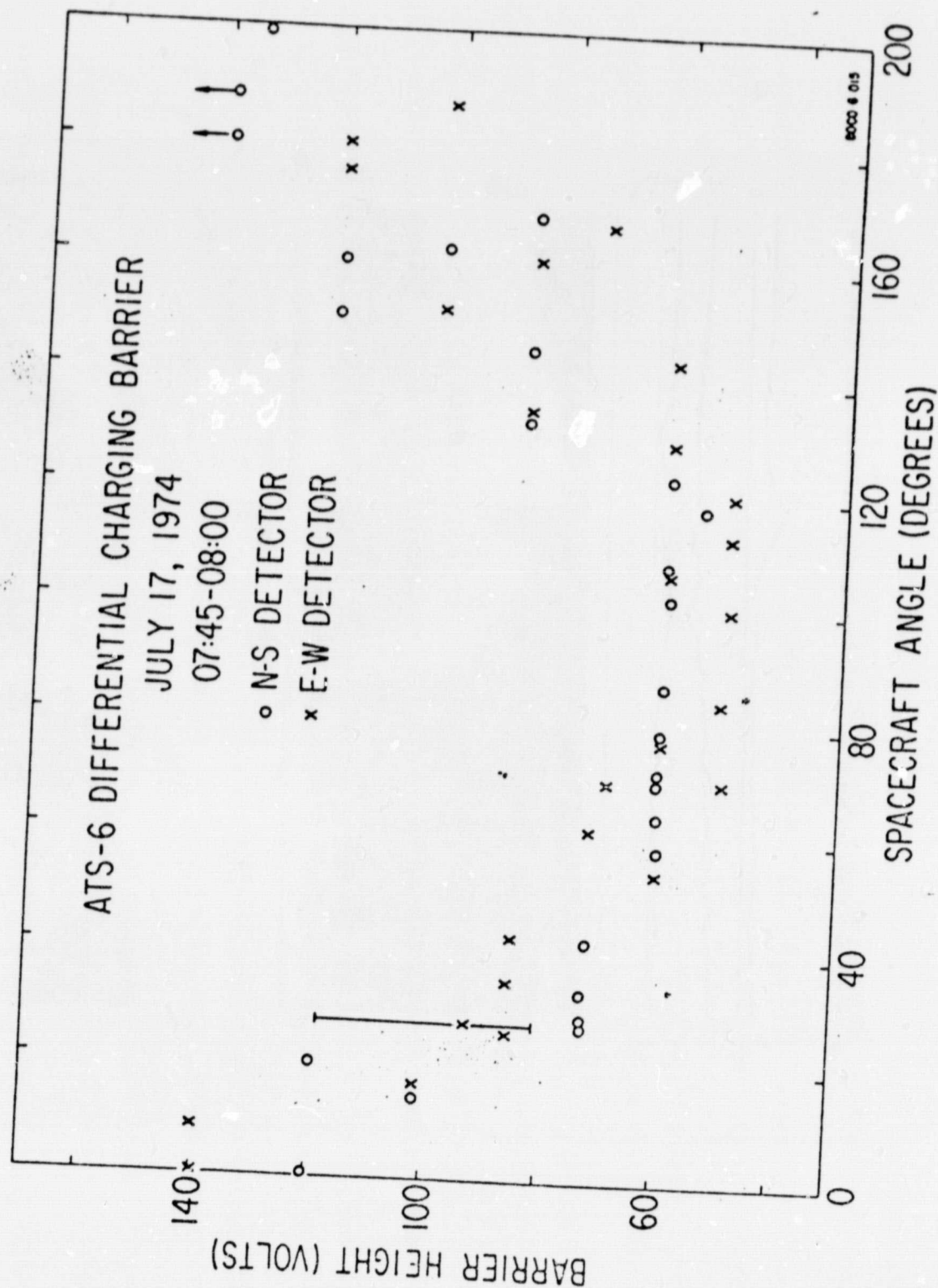


FIGURE 27

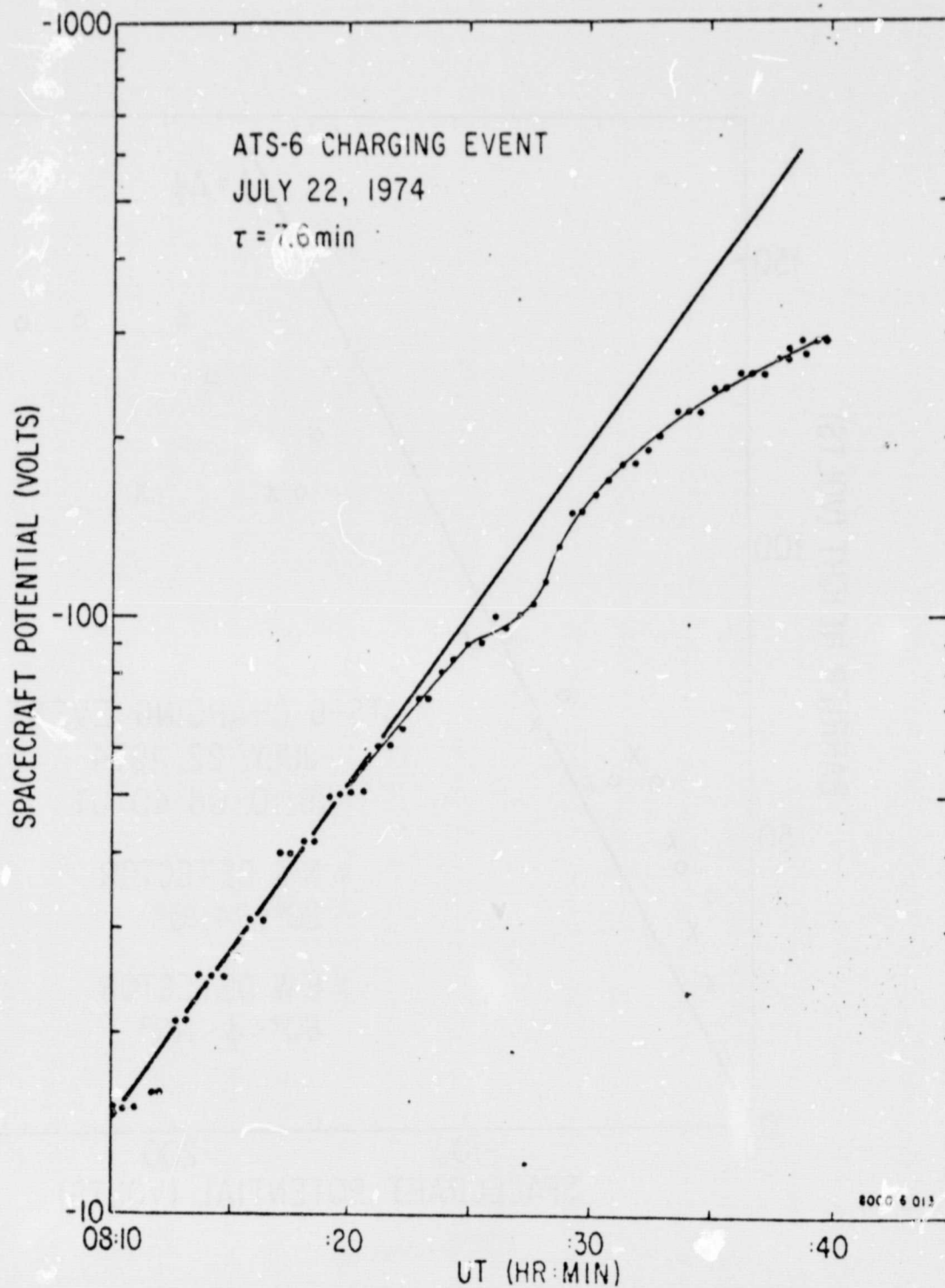


FIGURE 29

ORIGINAL PAGE IS
OF POOR QUALITY

c-2

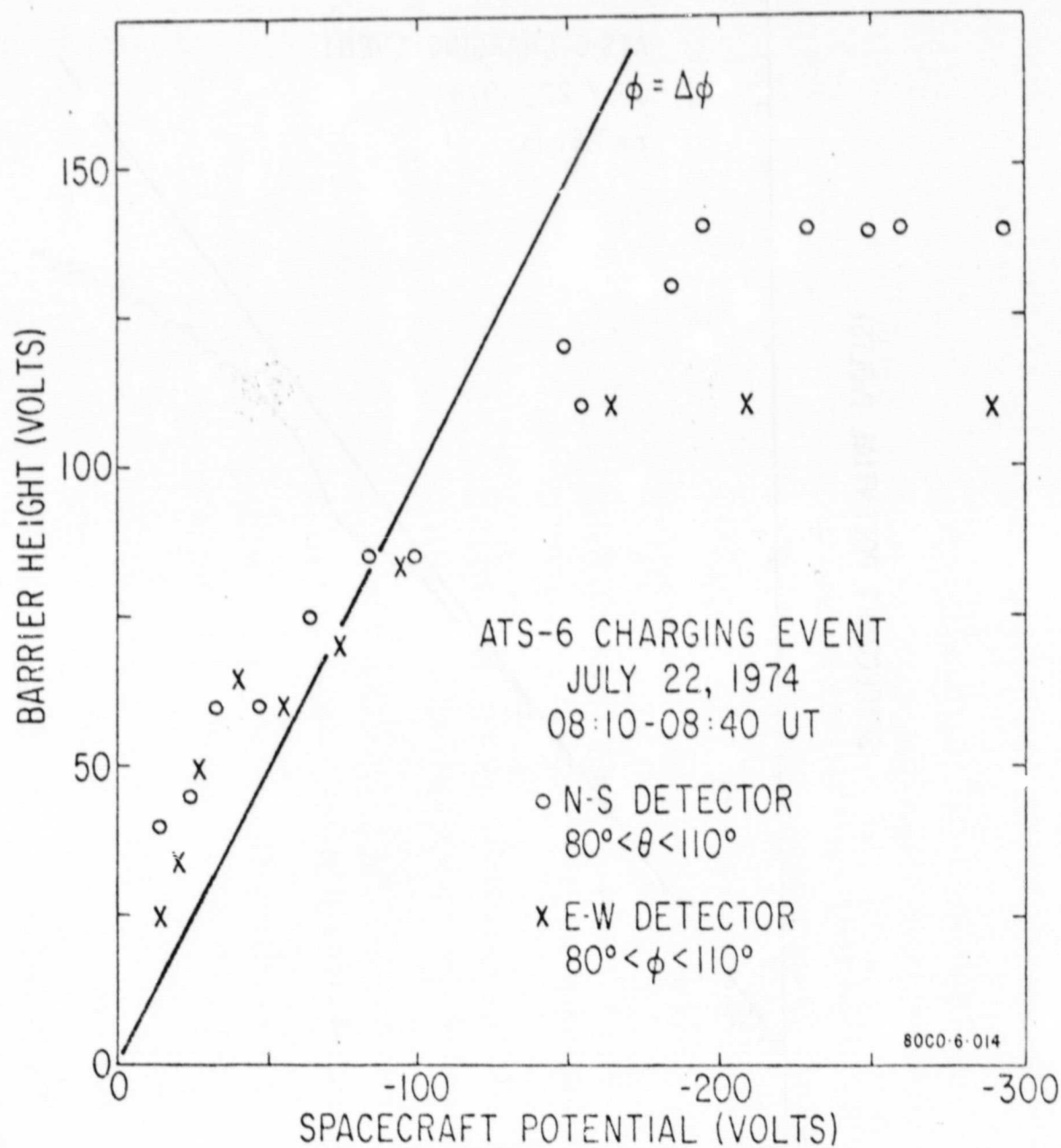


FIGURE 30

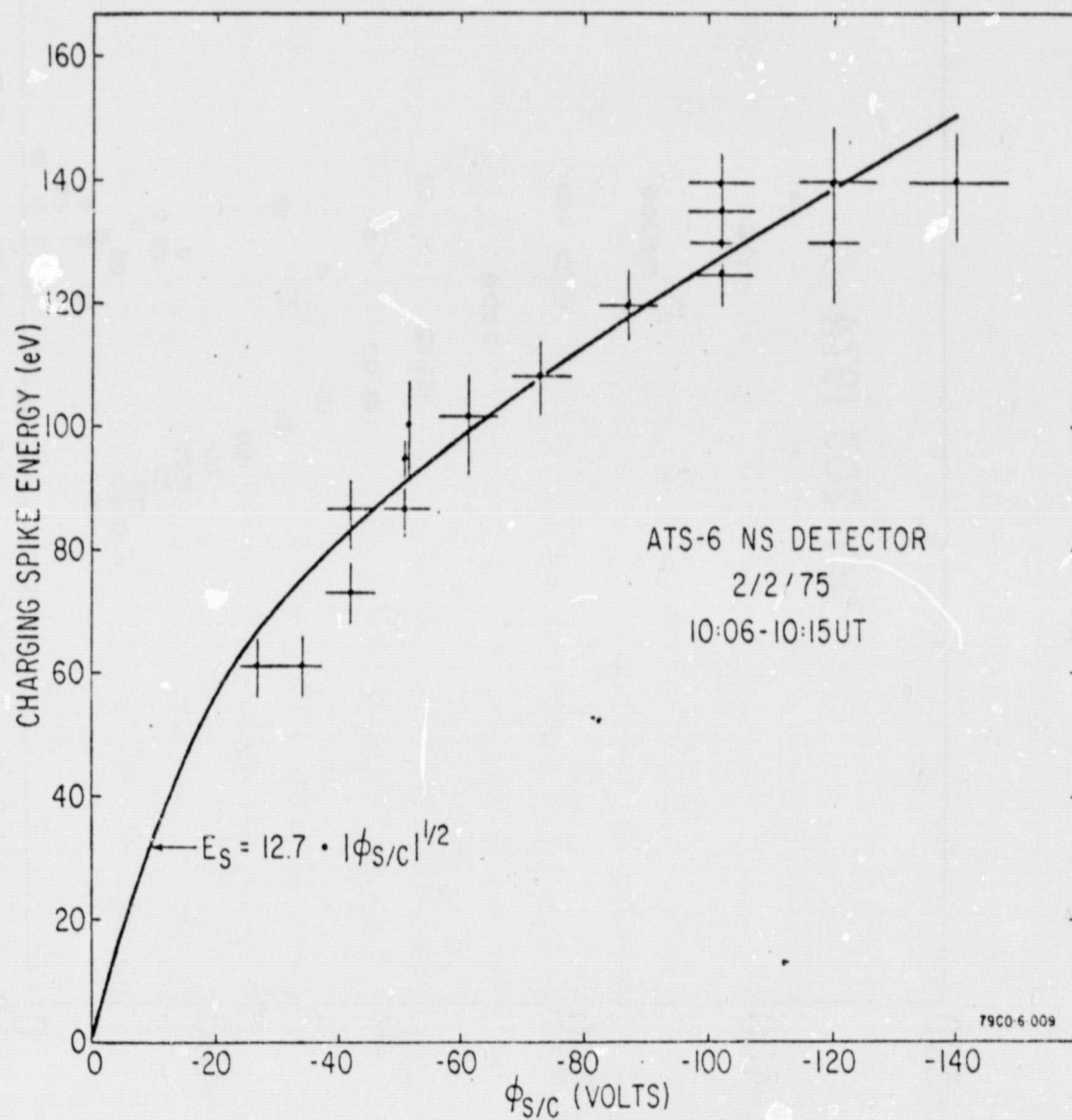
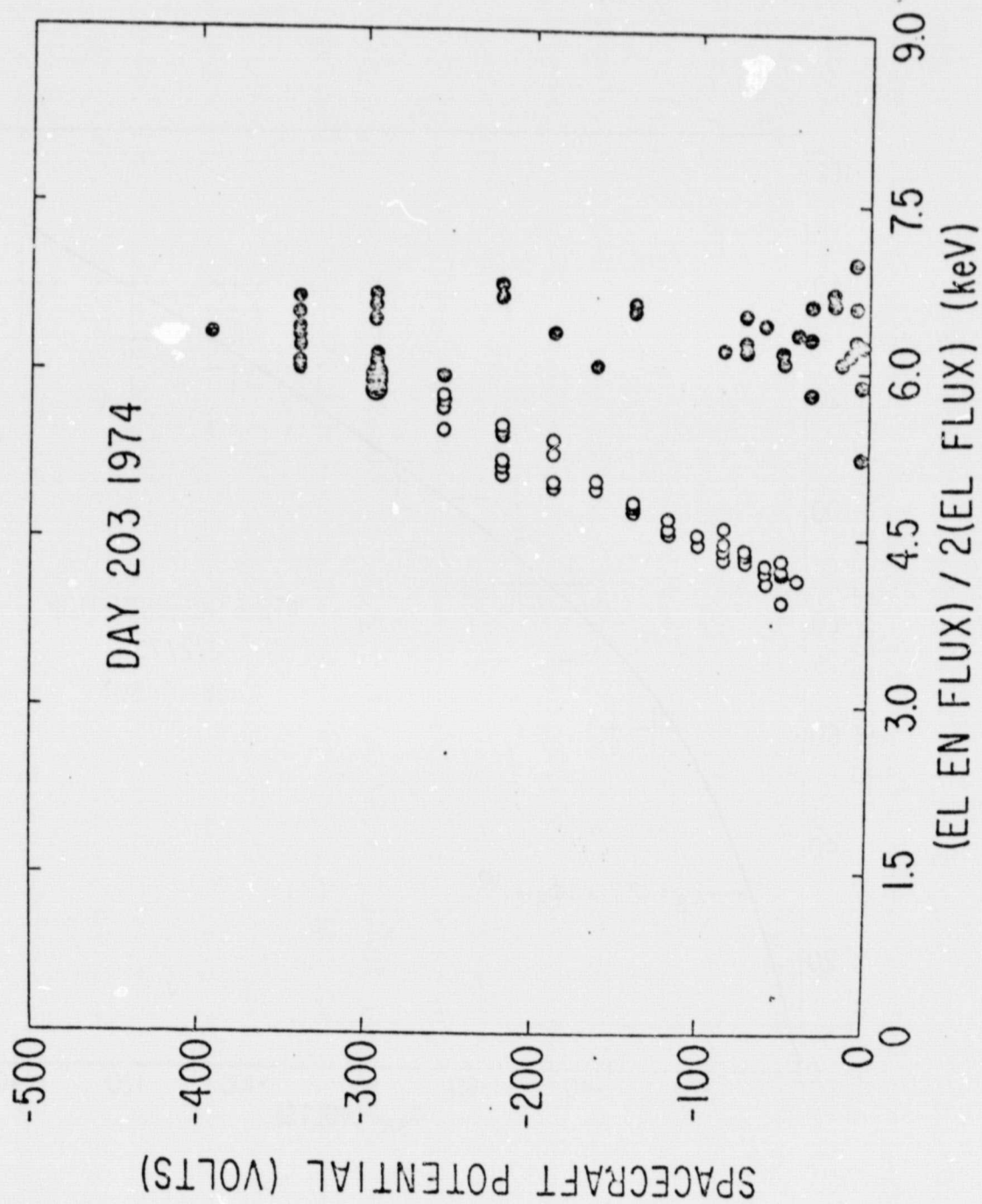


FIGURE 31



77JQ 6-026

FIGURE 32

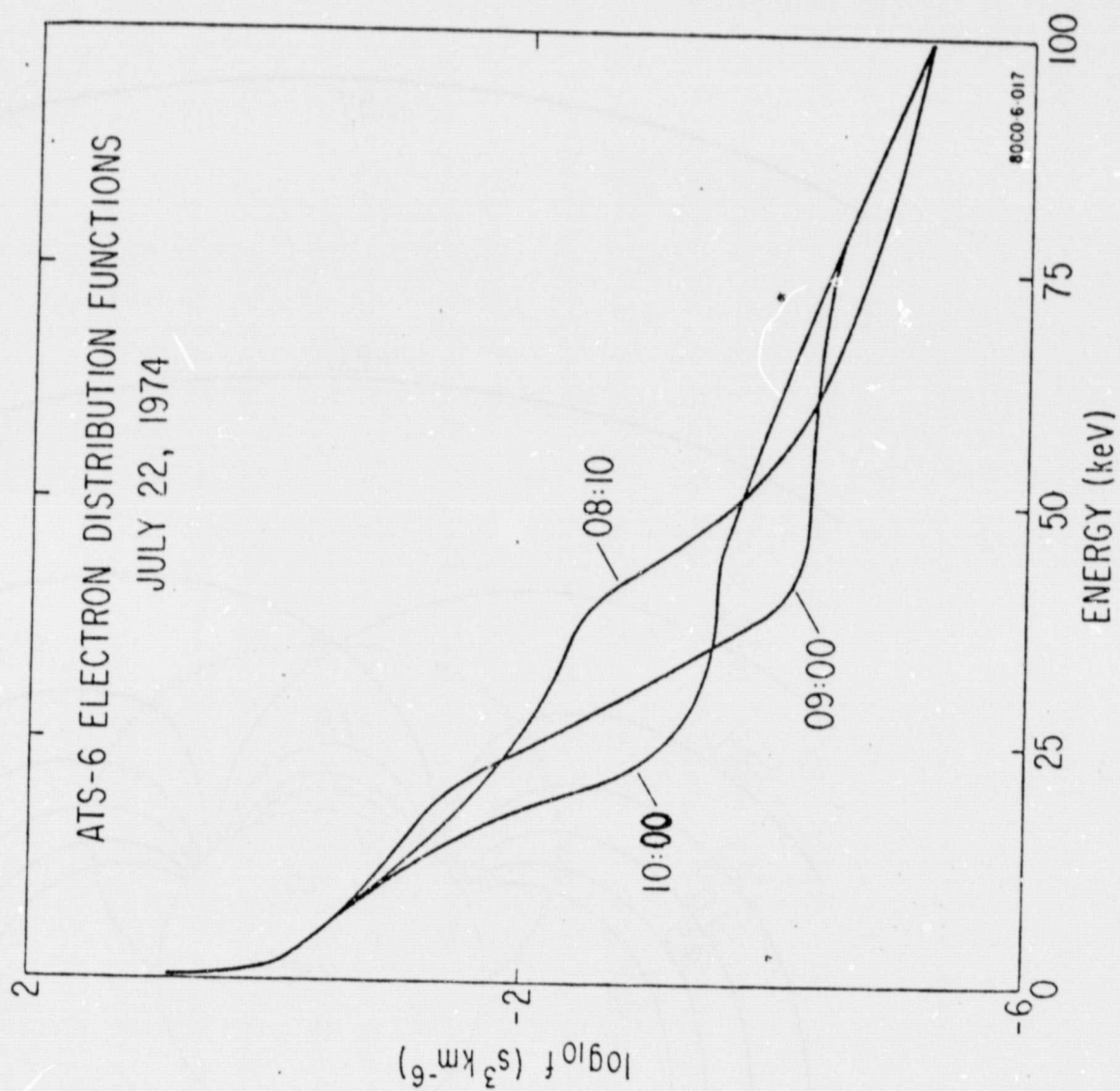
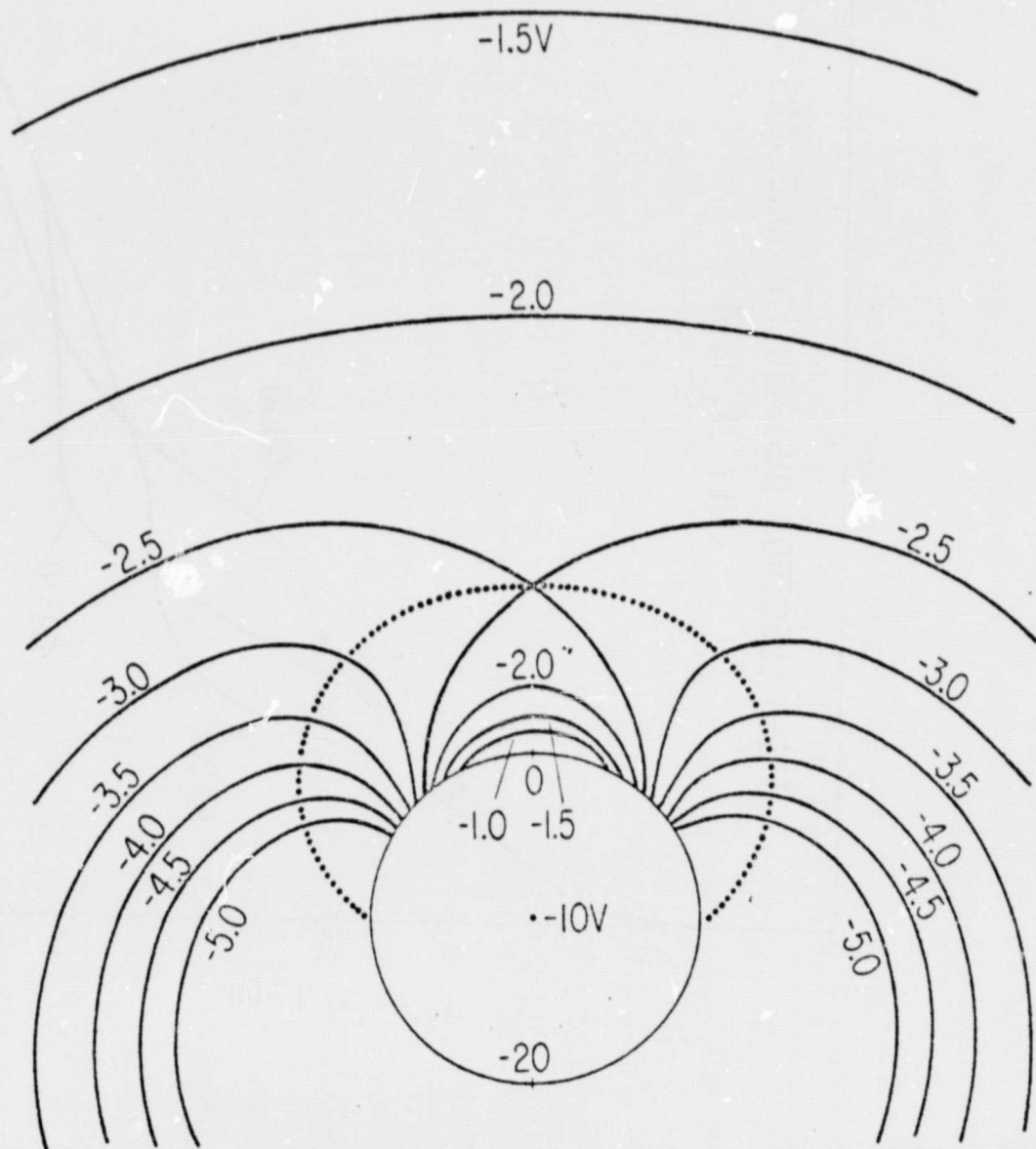


FIGURE 33

MONOPOLE + DIPOLE MODEL
POTENTIAL CONTOURS
 $V_{\text{MONOPOLE}} = -10\text{V}$, $V_{\text{DIPOLE}} = +10\text{V}$



80C0 6 030

FIGURE 34

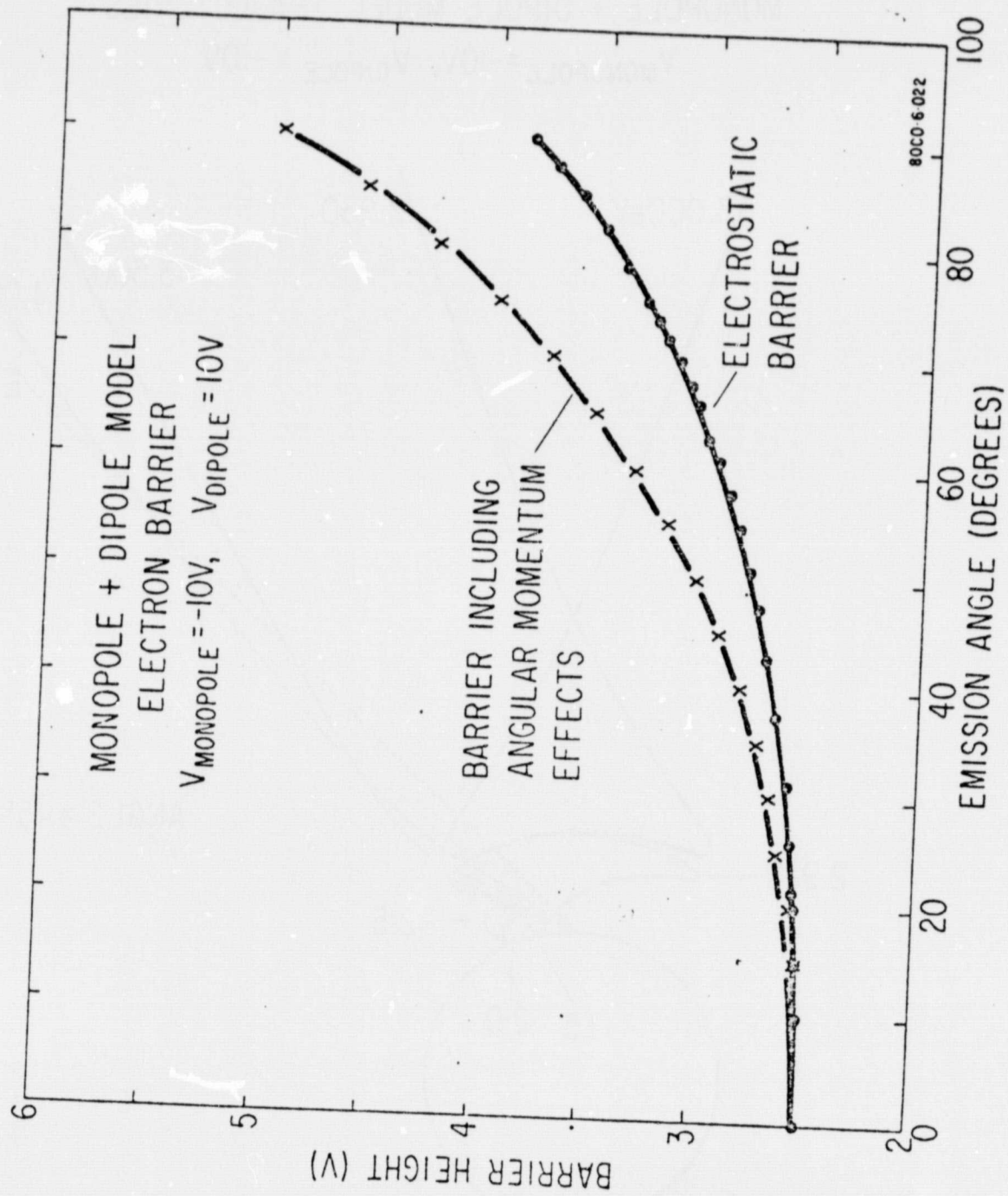
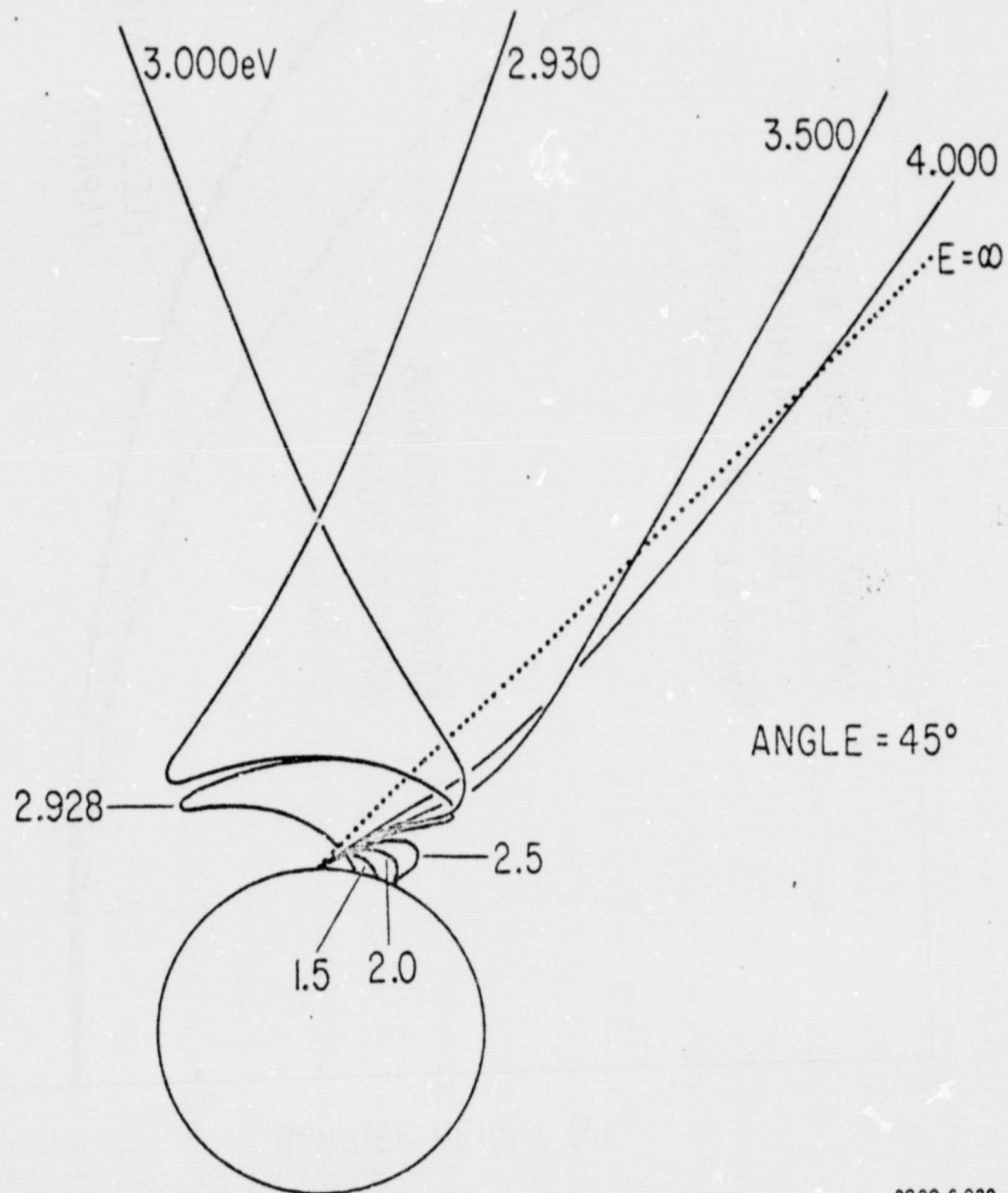


FIGURE 35

MONOPOLE + DIPOLE MODEL TRAJECTORIES

$$V_{\text{MONOPOLE}} = -10\text{V}, V_{\text{DIPOLE}} = +10\text{V}$$



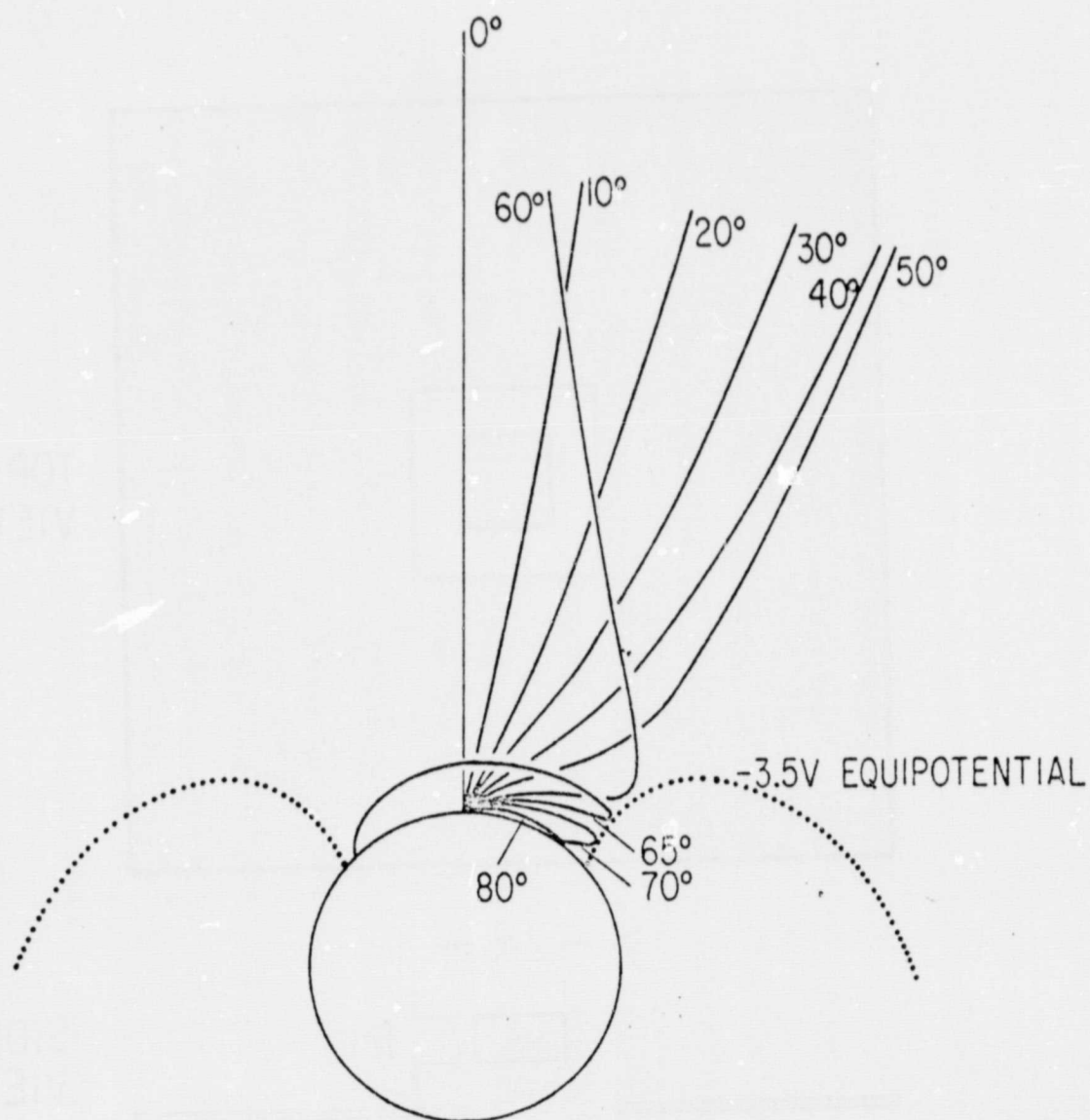
80CO-6-029

FIGURE 36

MONOPOLE + DIPOLE MODEL TRAJECTORIES

$V_{\text{MONOPOLE}} = -10\text{V}$, $V_{\text{DIPOLE}} = +10\text{V}$

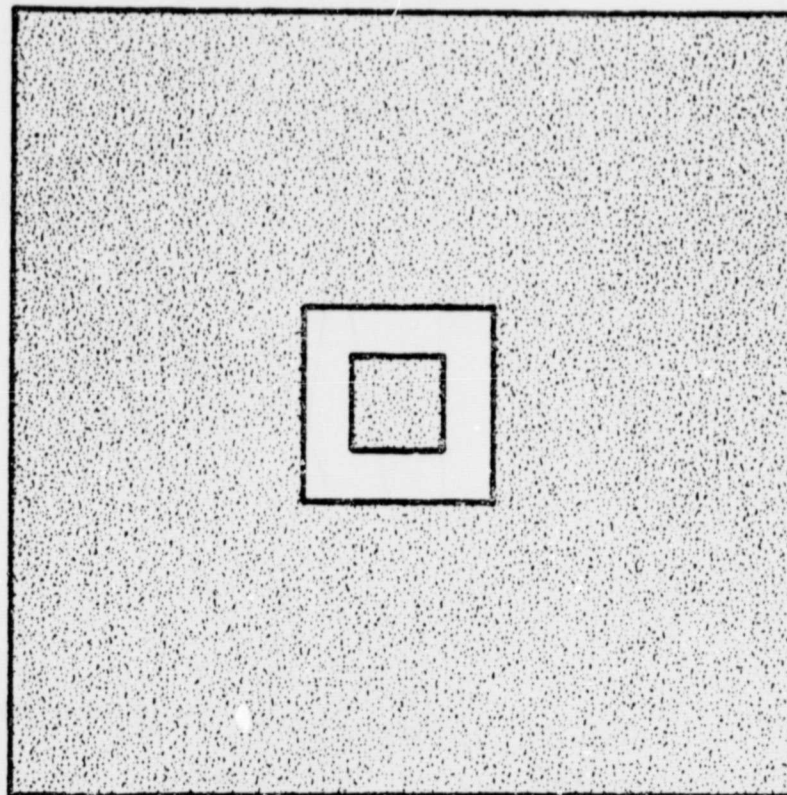
ENERGY = 3.5eV



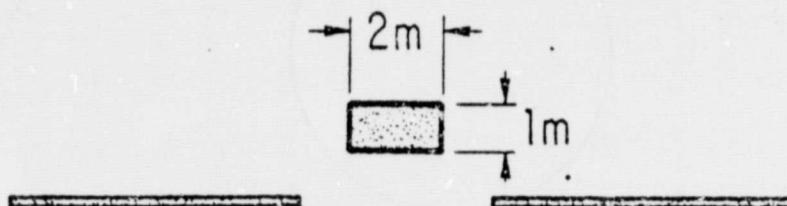
80C0-6-028

FIGURE 37

NASCAP/ATS-6 ANTENNA OBJECT



TOP
VIEW



SIDE
VIEW

80CO-6-031

FIGURE 38

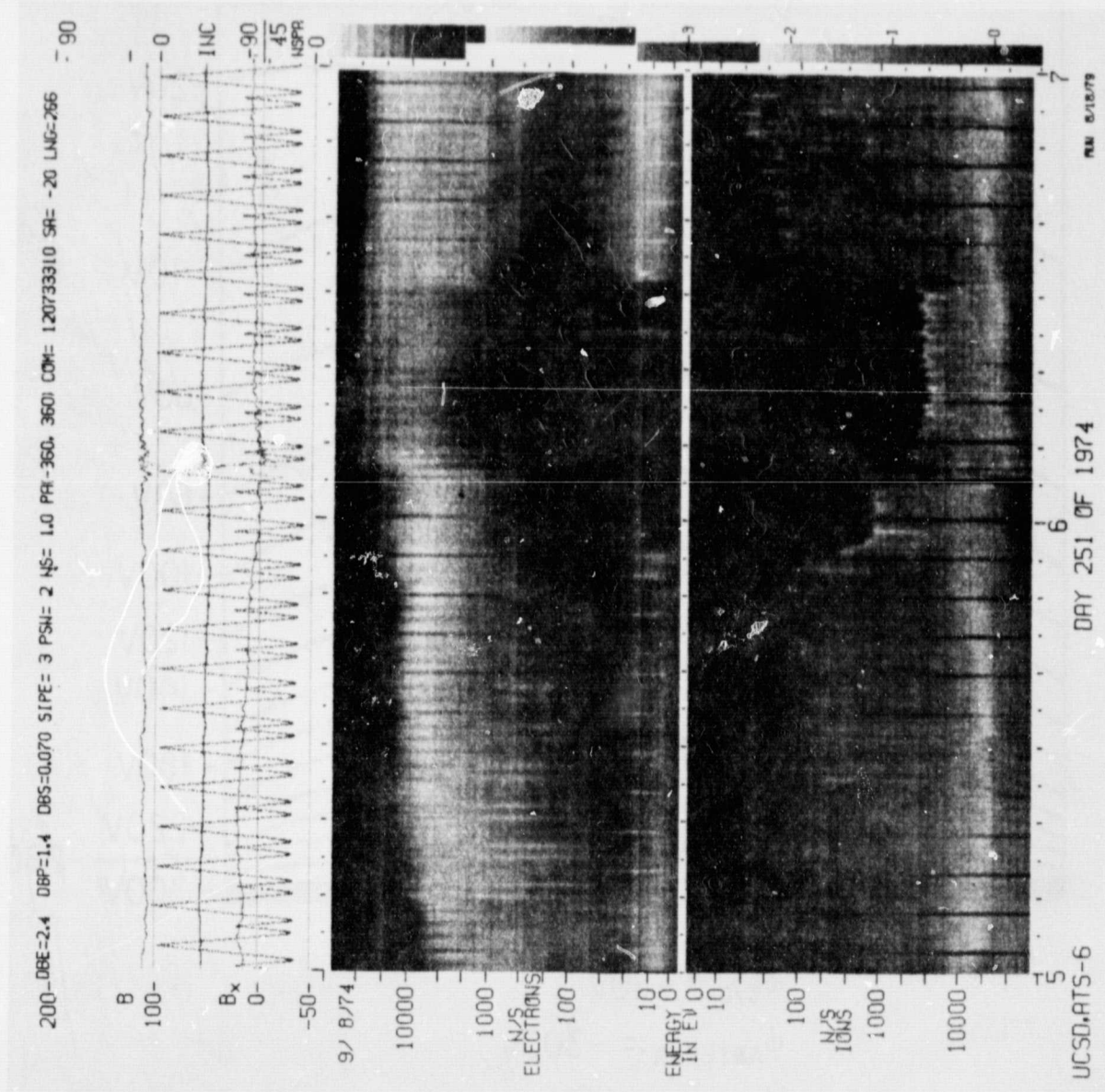
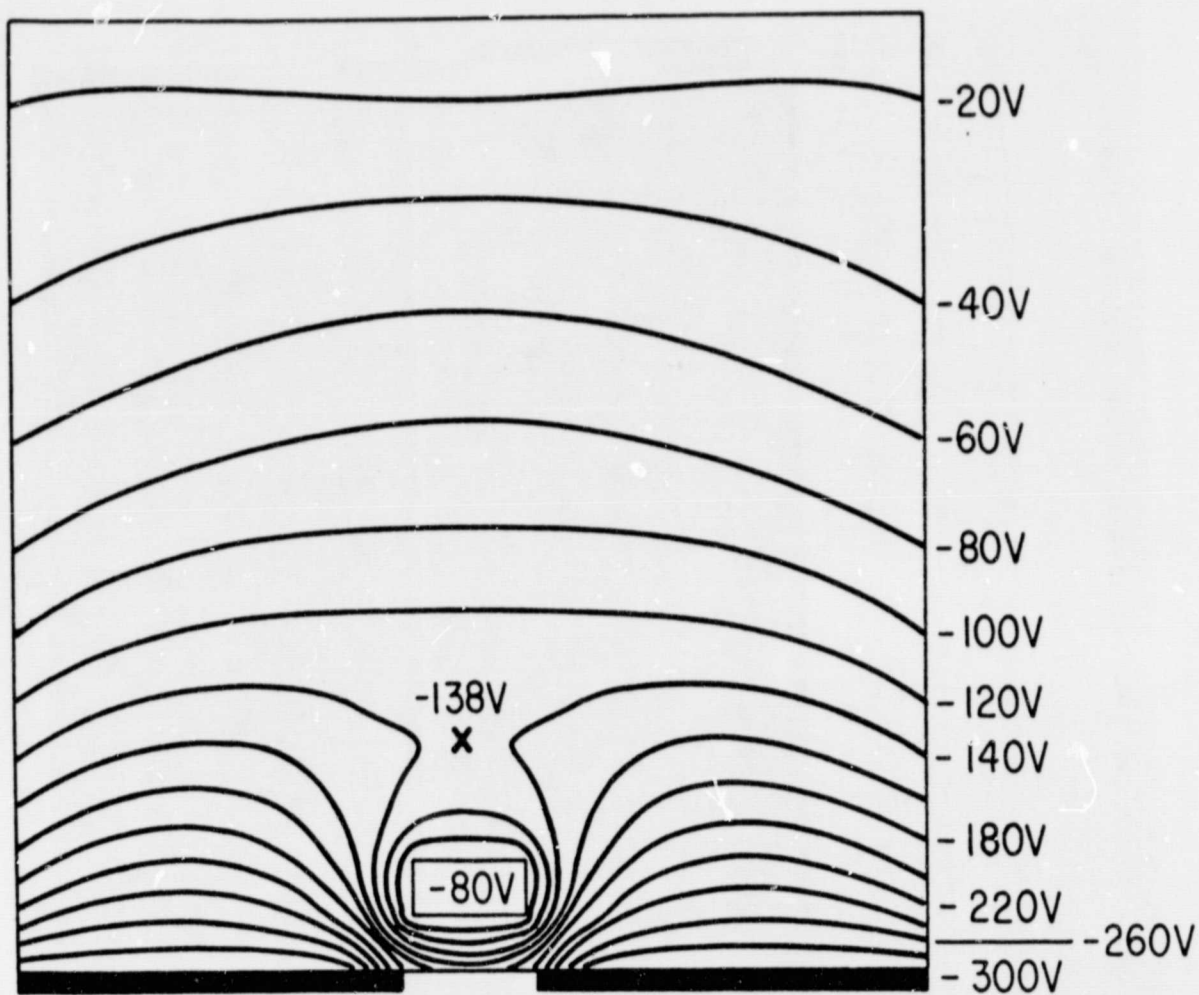


FIGURE 39

ORIGINAL PAGE IS
OF POOR QUALITY

ATS-6 POTENTIAL CONTOURS



$$\phi_{s/c} = -80V$$

$$\phi_{\text{ANTENNA}} = -300V$$

$$V_{\text{BARRIER}} = 58V$$

FIGURE 40

200 DBE-2.5 DBP-1.2 DBS-0.060 S1P-3 PSN-2 NS-1.0 PRI-360.3601 COW-124373210 SR- -20 LAG-265 -90

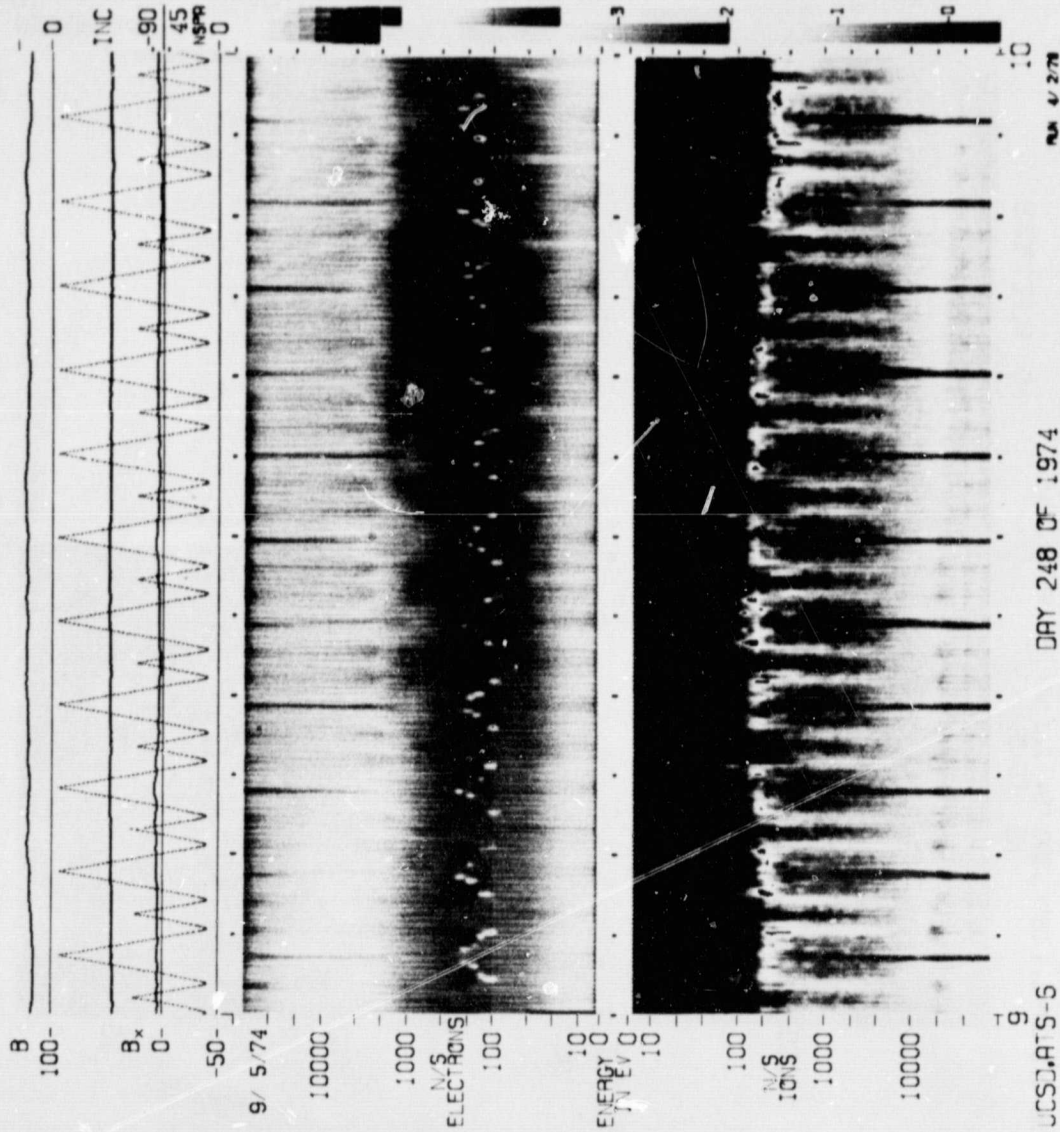


FIGURE 41

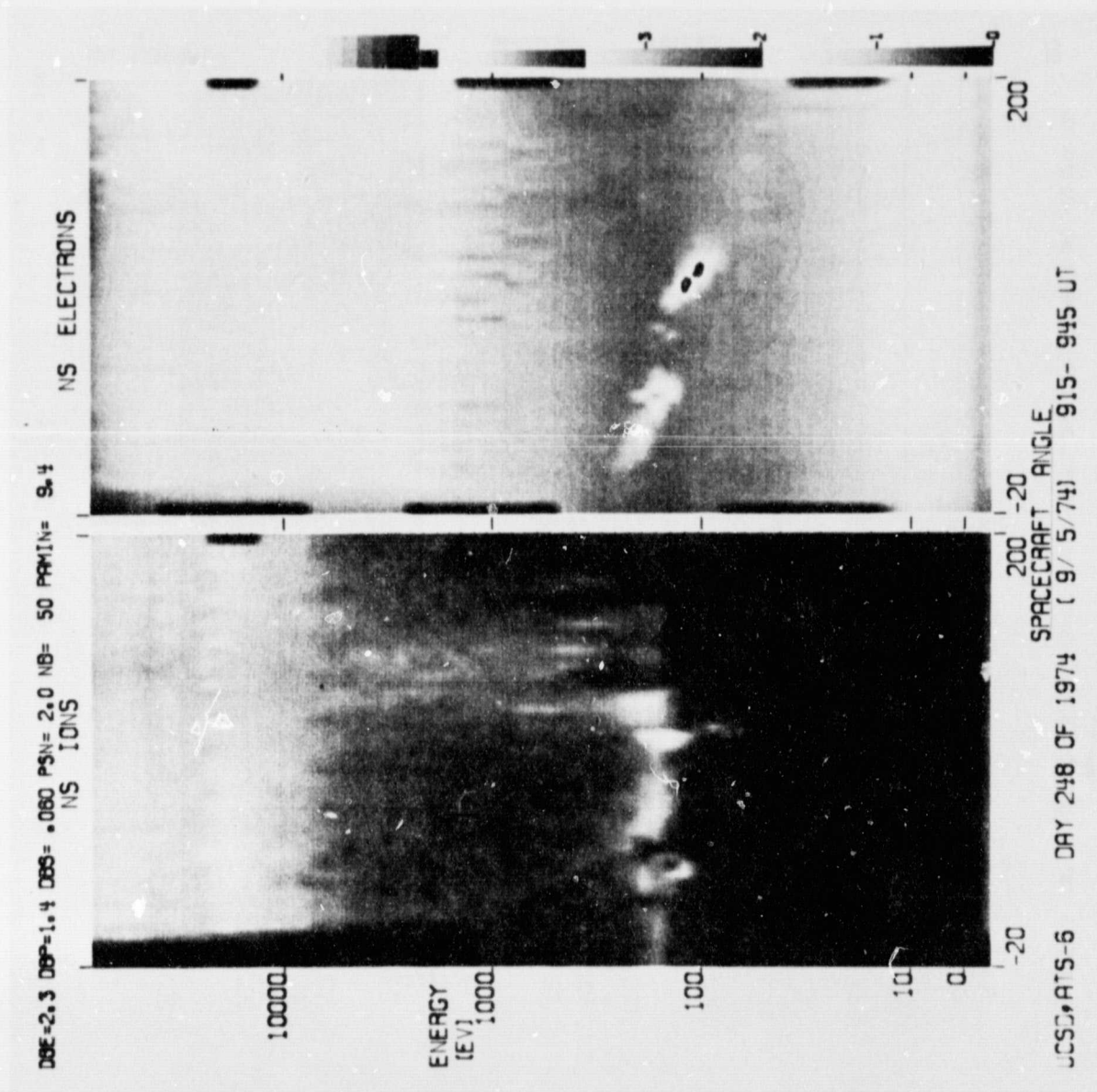


FIGURE 42

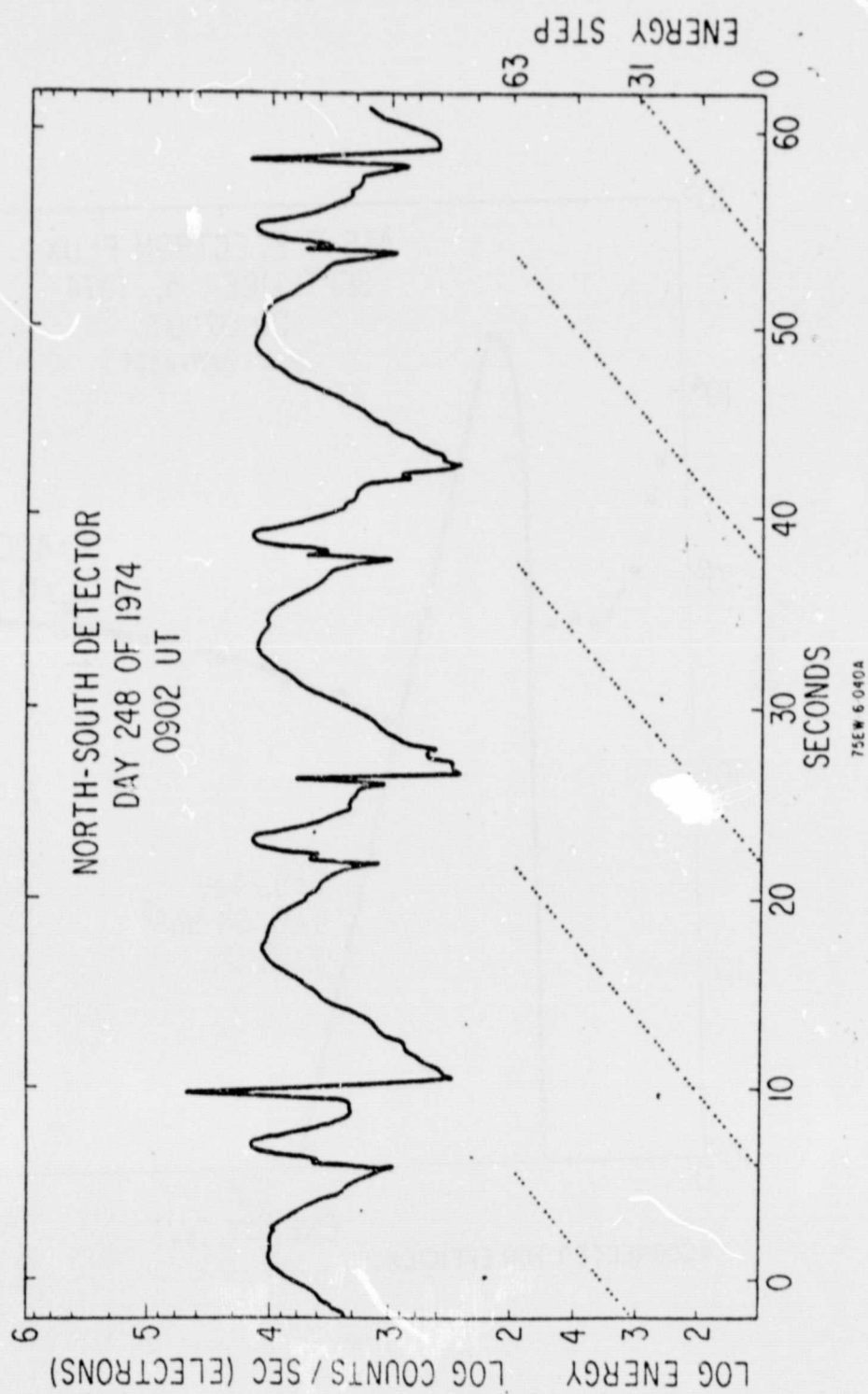


FIGURE 43

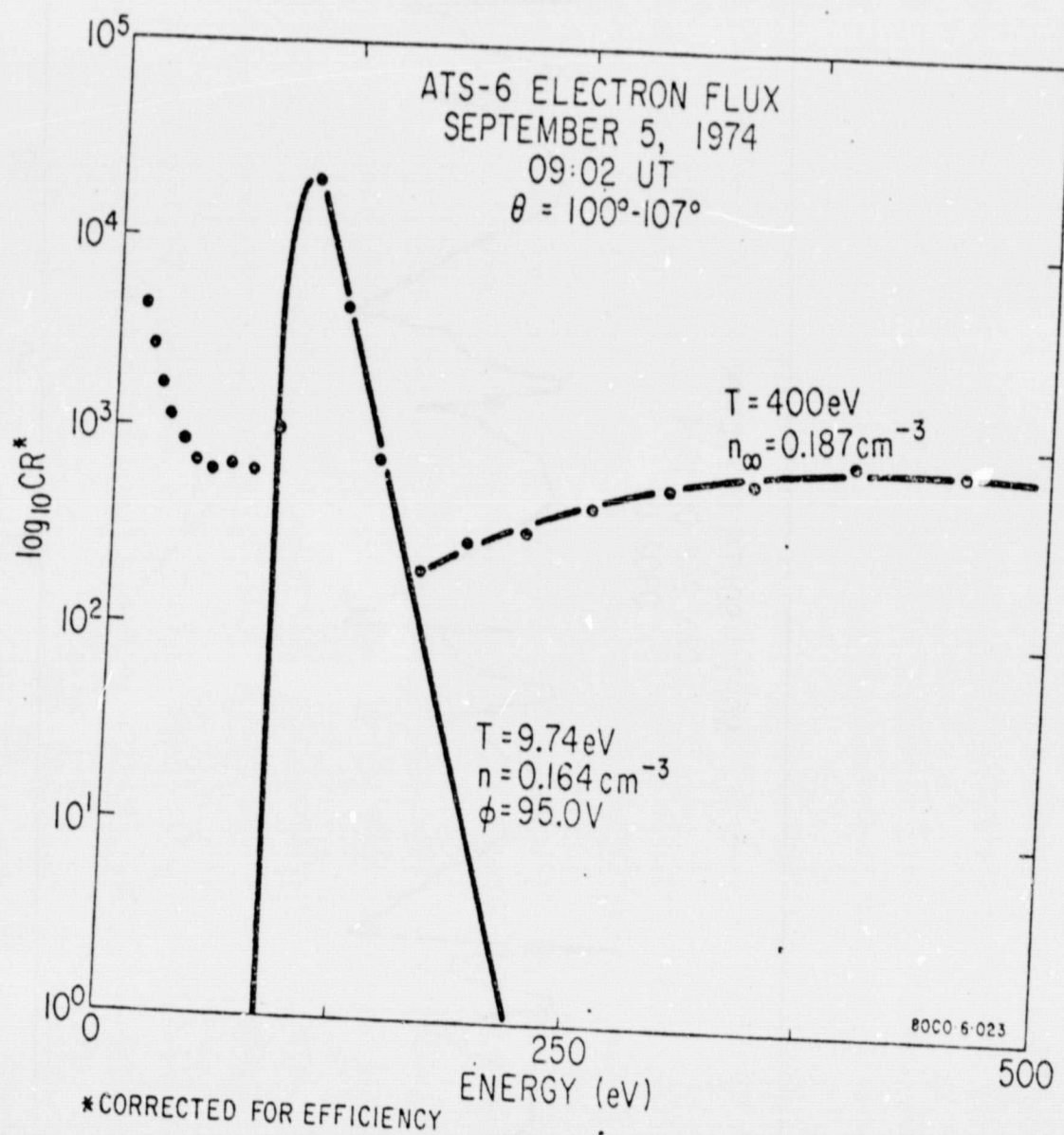


FIGURE 44

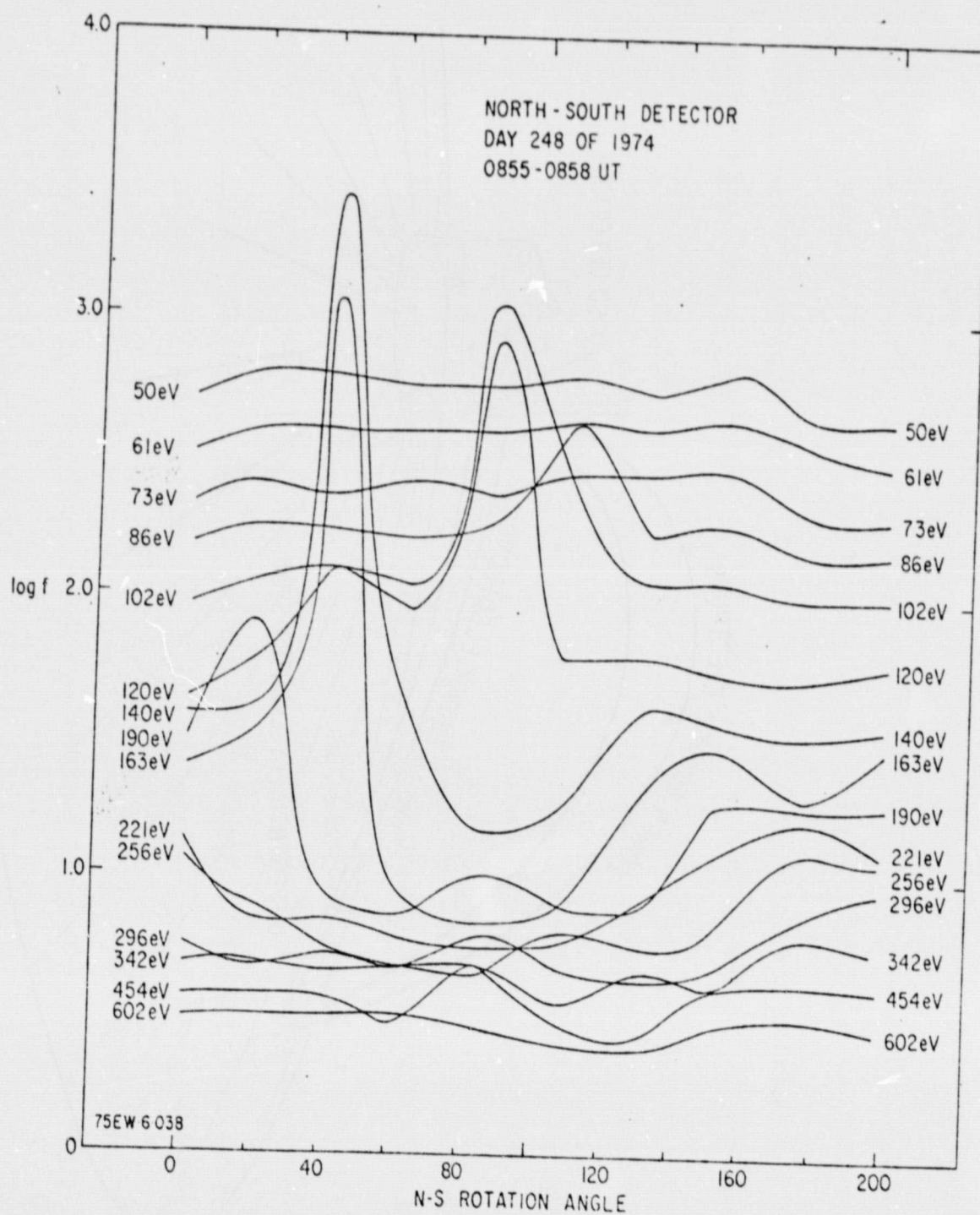


FIGURE 45

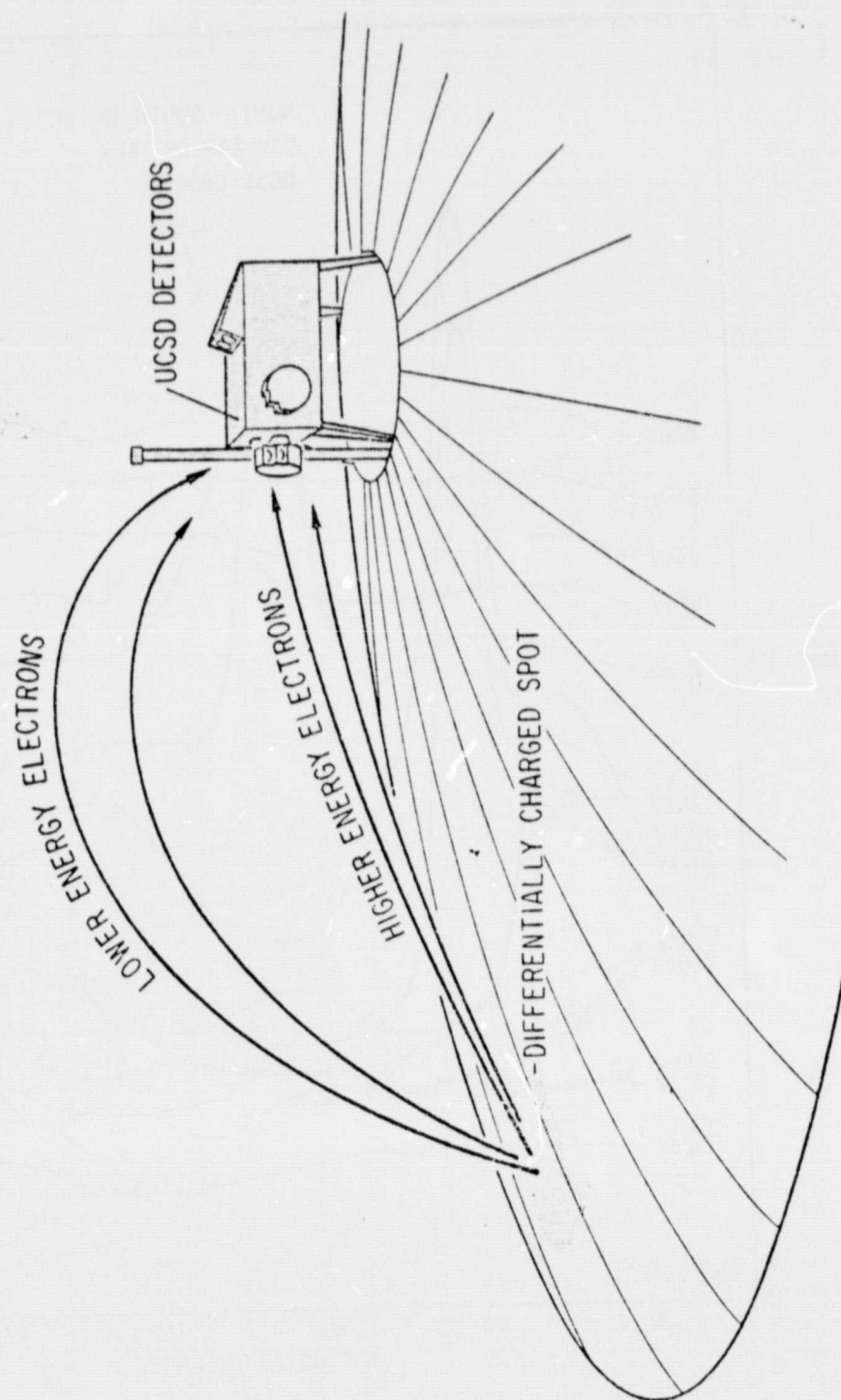


FIGURE 46

8/24/74

100-
B

100-
B*

-50-
0

10000-
1000-
100-
10-
10-
100-
1000-
10000-
IONS

ENERGY IN EV

10 100 1000 10000

0 90 45 0

1 NC

0 1 2 3 4 5 6

UCSD, ATS-6

DAY 236 OF 1974

ORIGINAL PAGE IS
OF POOR QUALITY

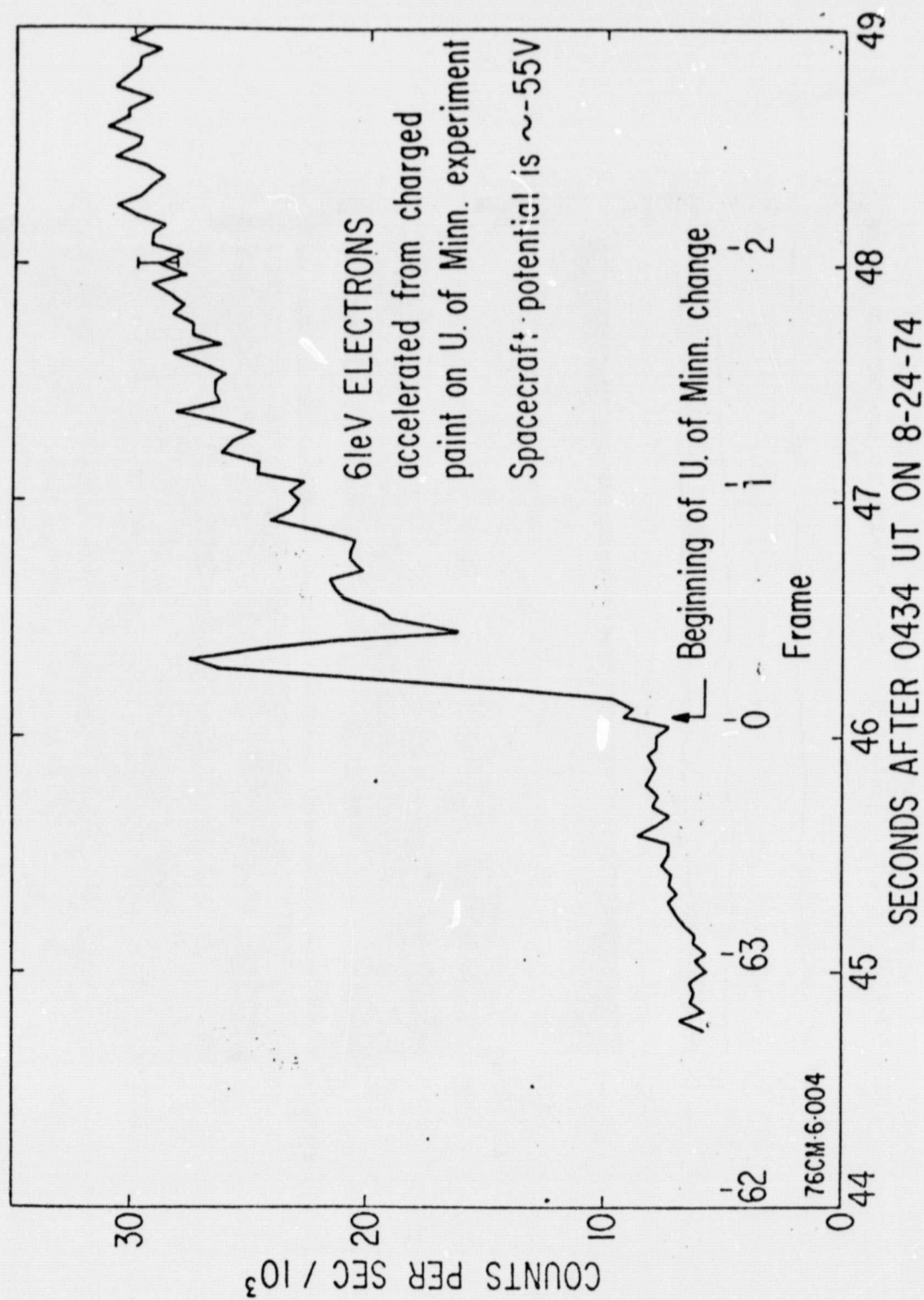


FIGURE 48

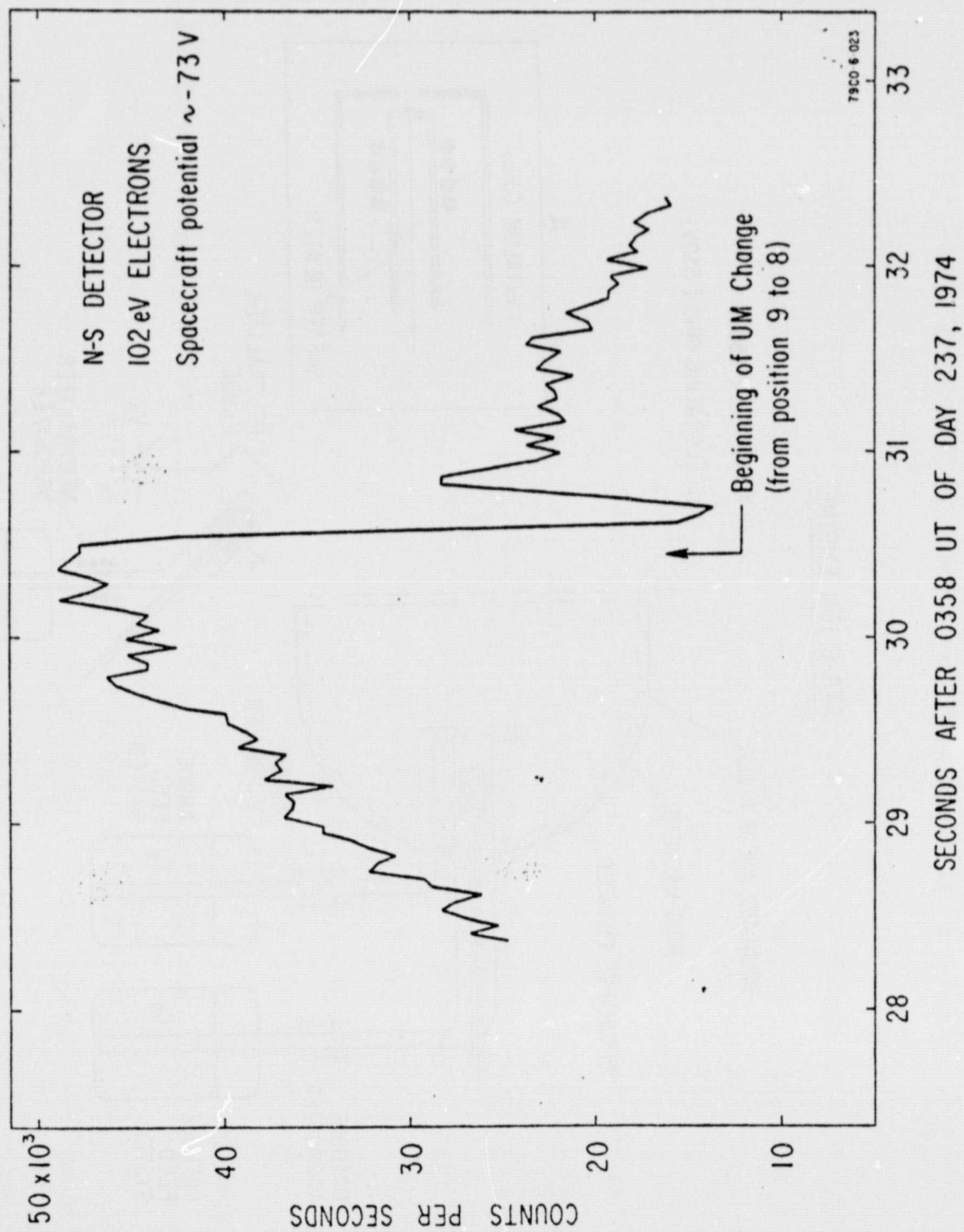


FIGURE 49

ATS-6 ION ENGINE

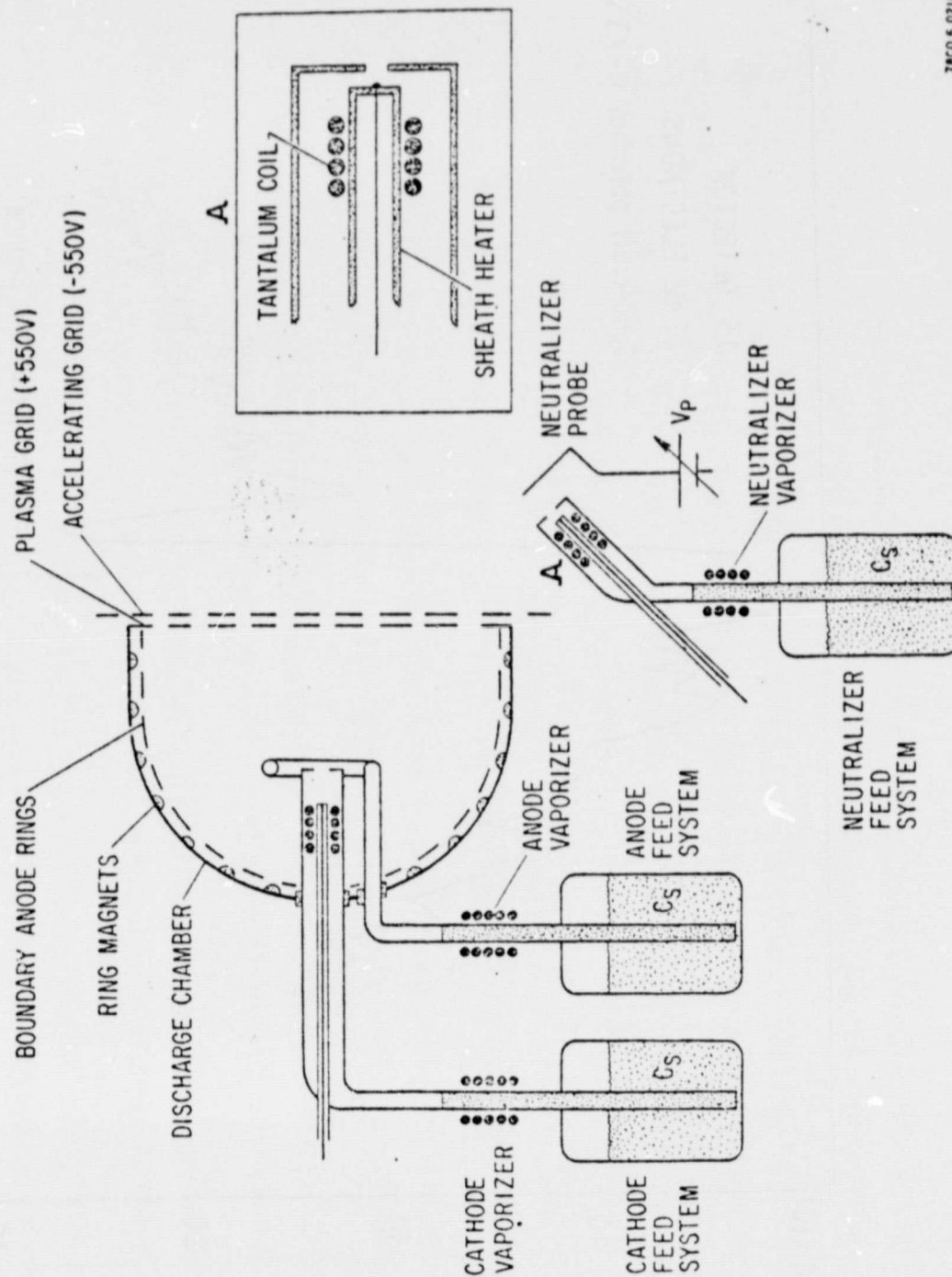
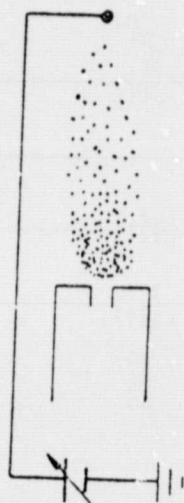
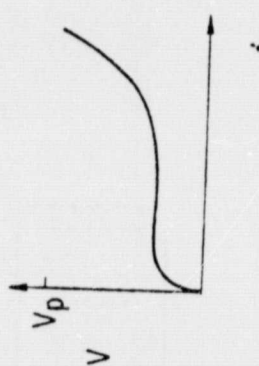
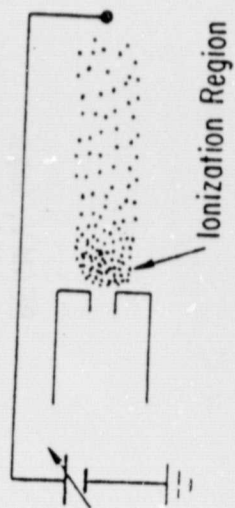


FIGURE 50

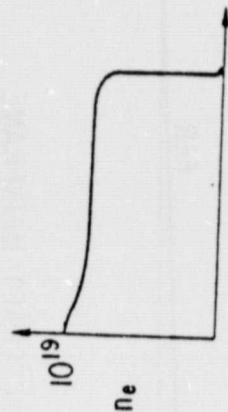
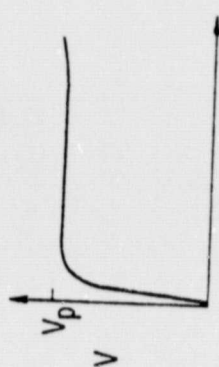
PLUME MODE



SPOT MODE



(a)

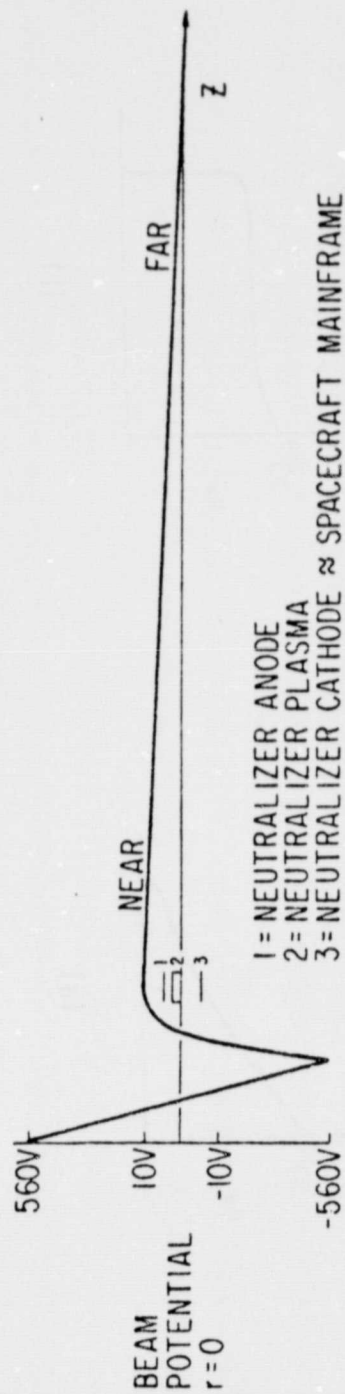


(b)

NEUTRALIZER OPERATIONAL MODES

80CO 5 036

FIGURE 51



$$n_{\text{BEAM}} = n_{\text{AMBIENT}}$$

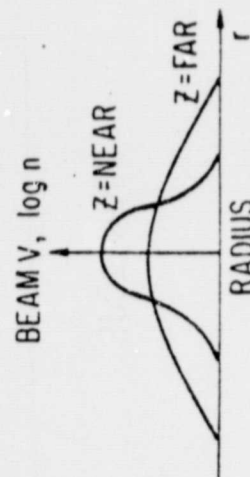
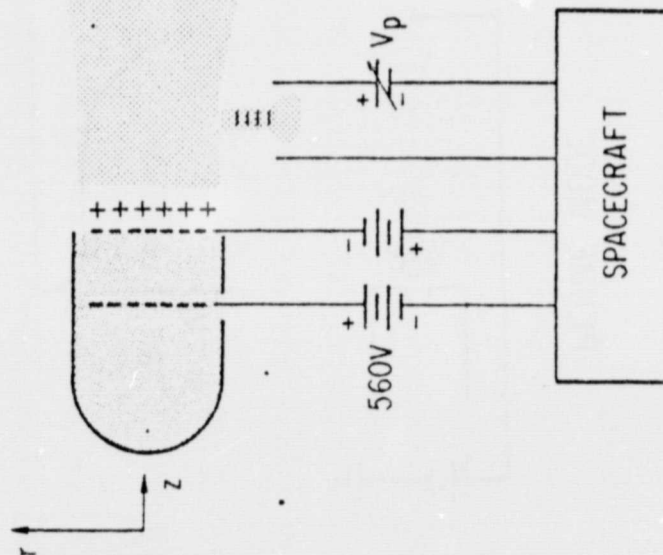


FIGURE 52

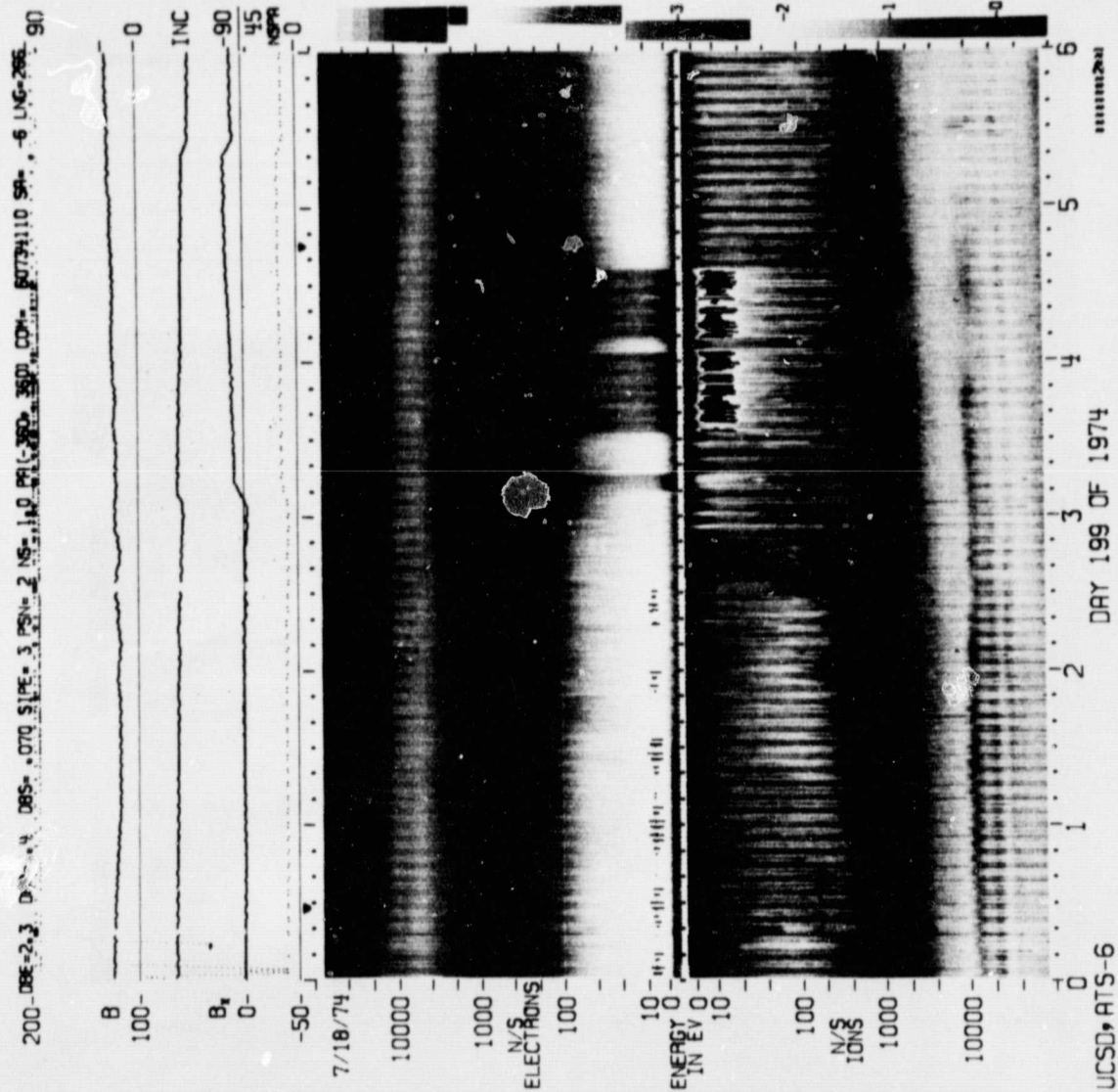


FIGURE 53

ORIGINAL PAGE IS
OF POOR QUALITY

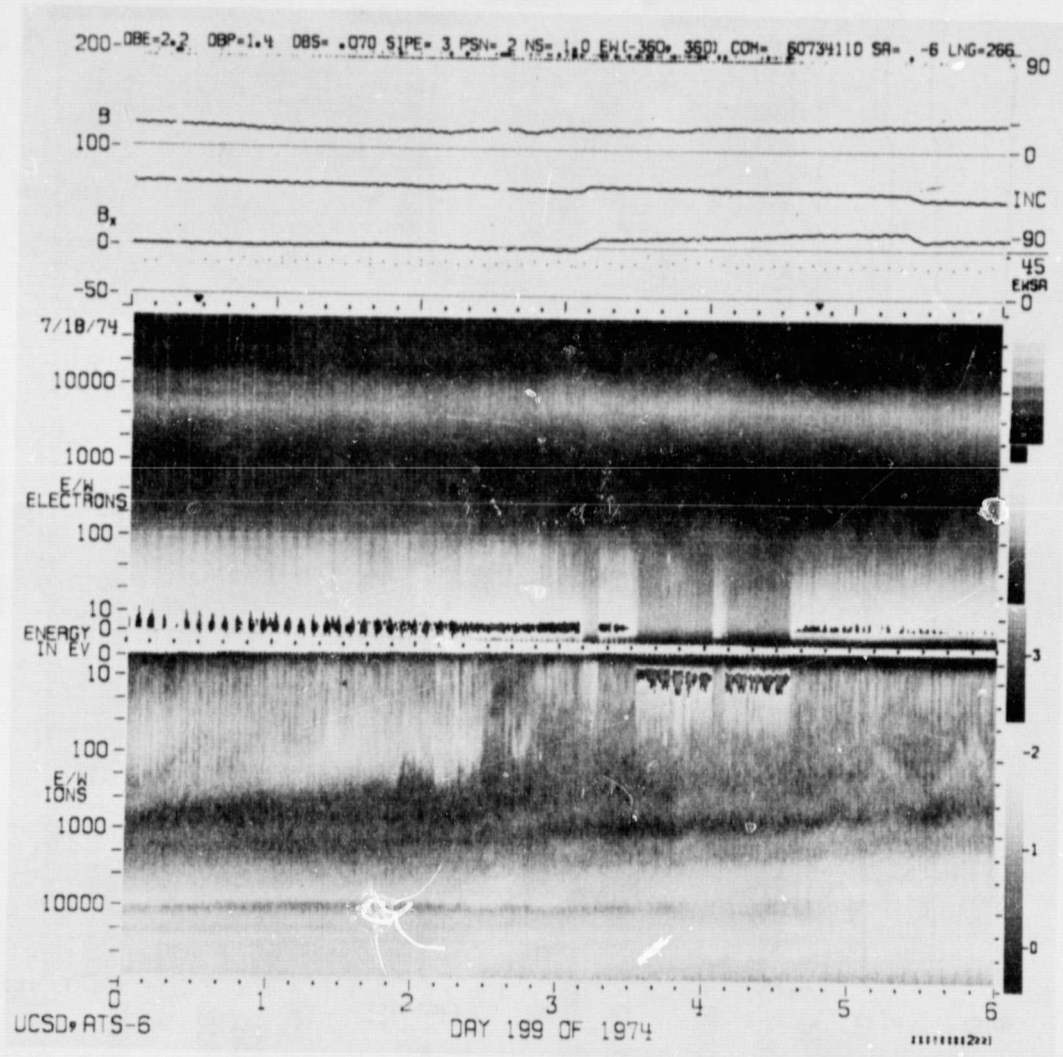


FIGURE 54

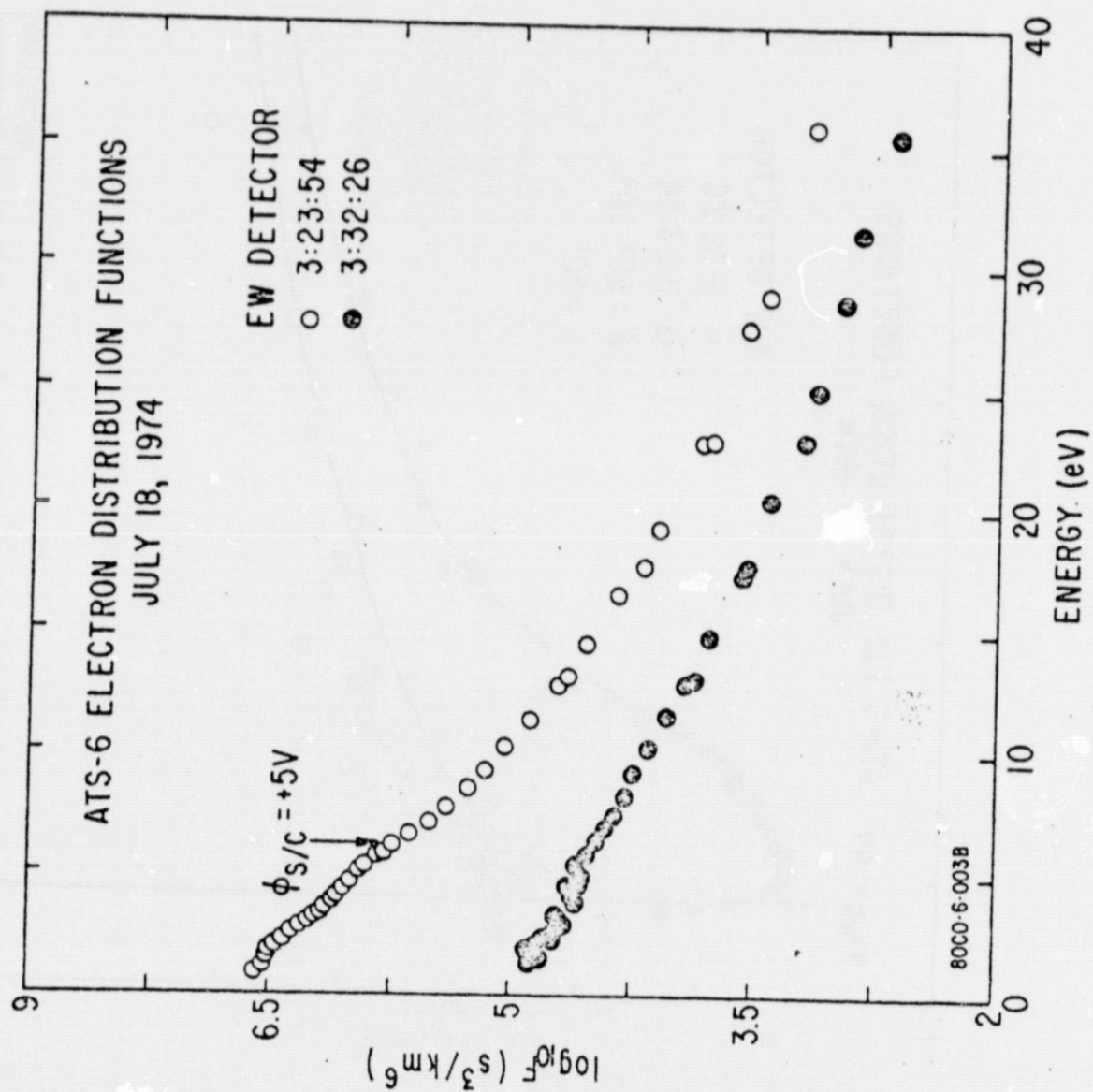


FIGURE 55

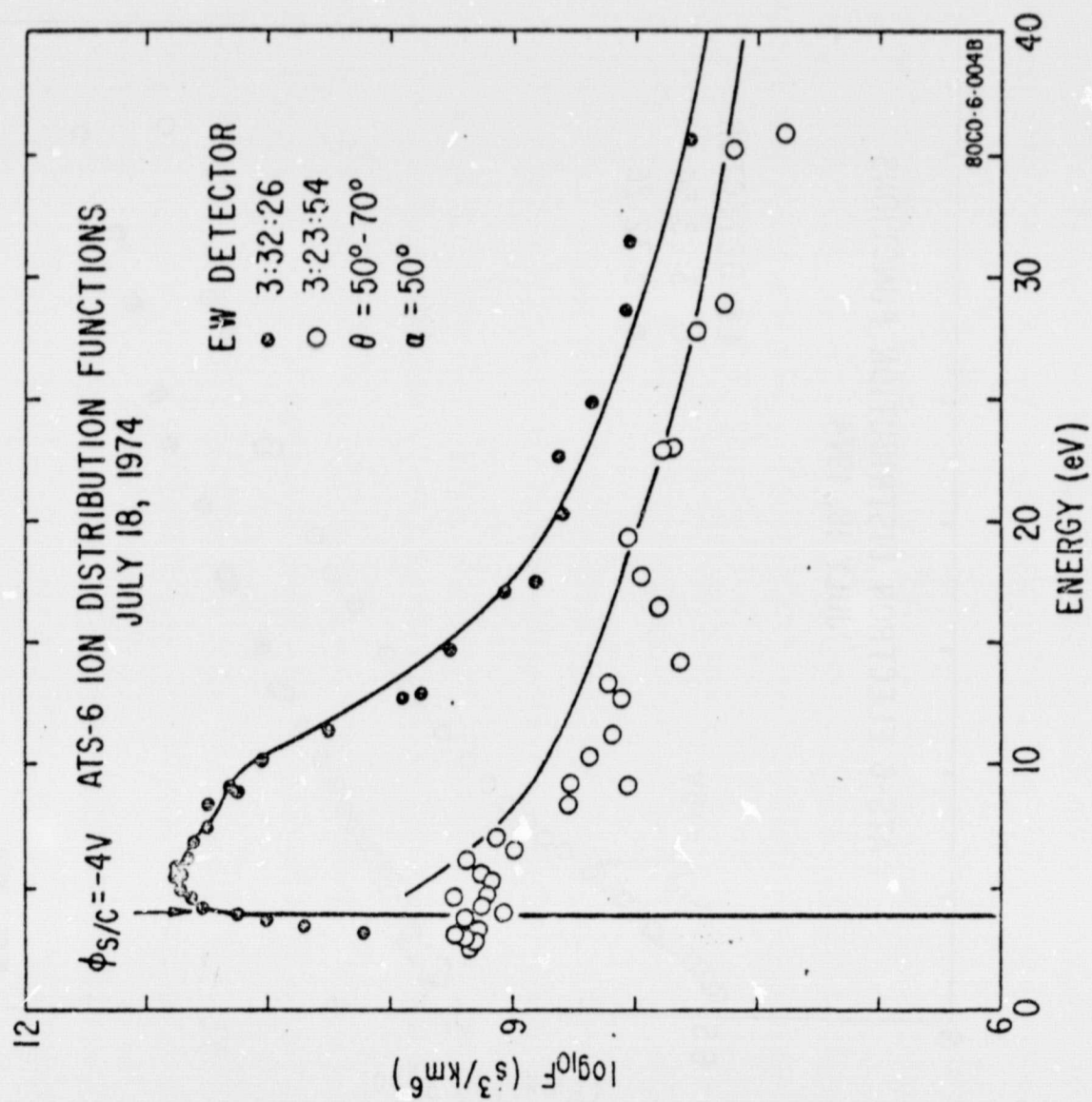


FIGURE 56

ION ENGINE OPERATION 199/74 (I.E. NO. 2)

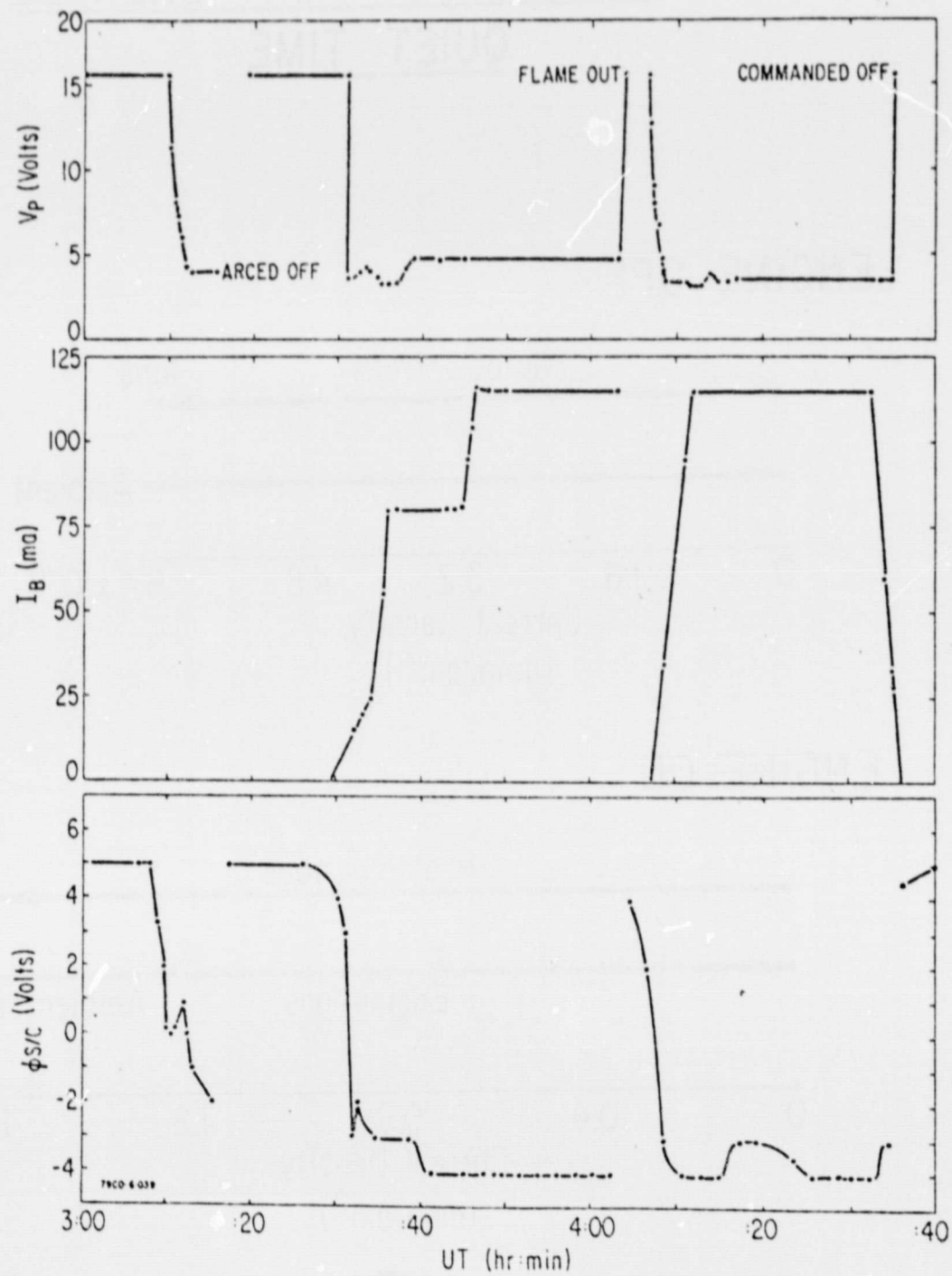
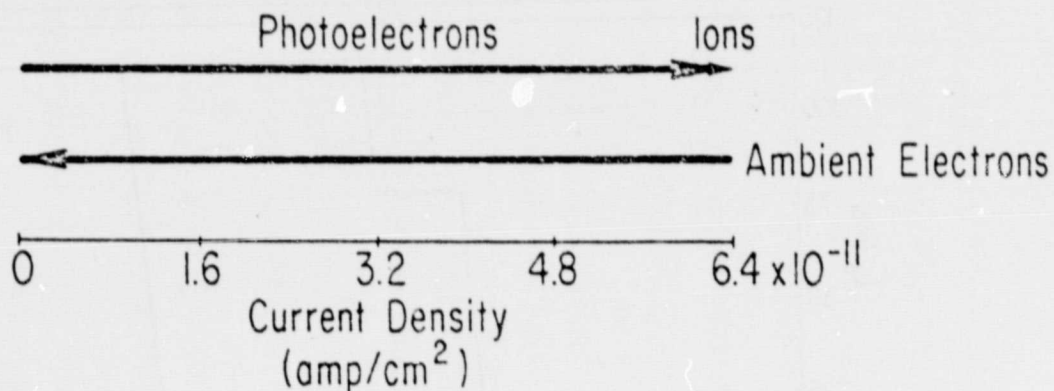


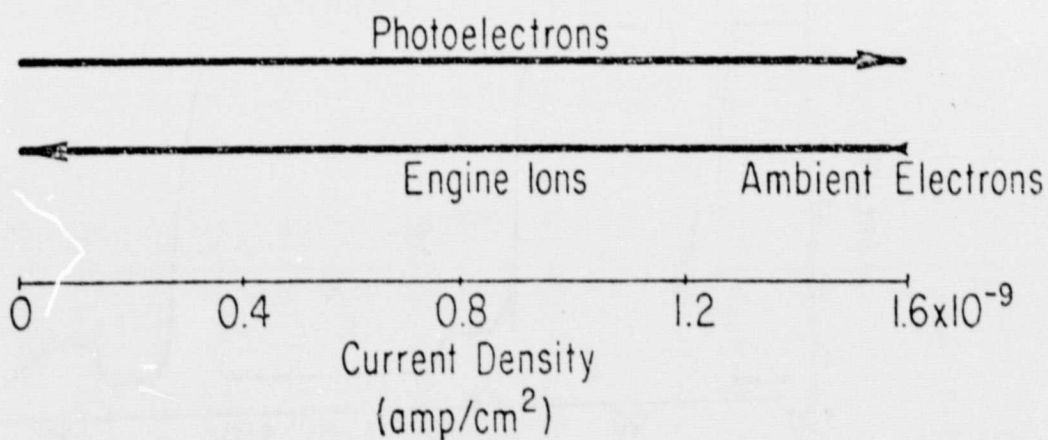
FIGURE 57

SUNLIGHT CURRENT BALANCE
QUIET TIME

ENGINE OFF



ENGINE ON



80CO-6-034

FIGURE 58

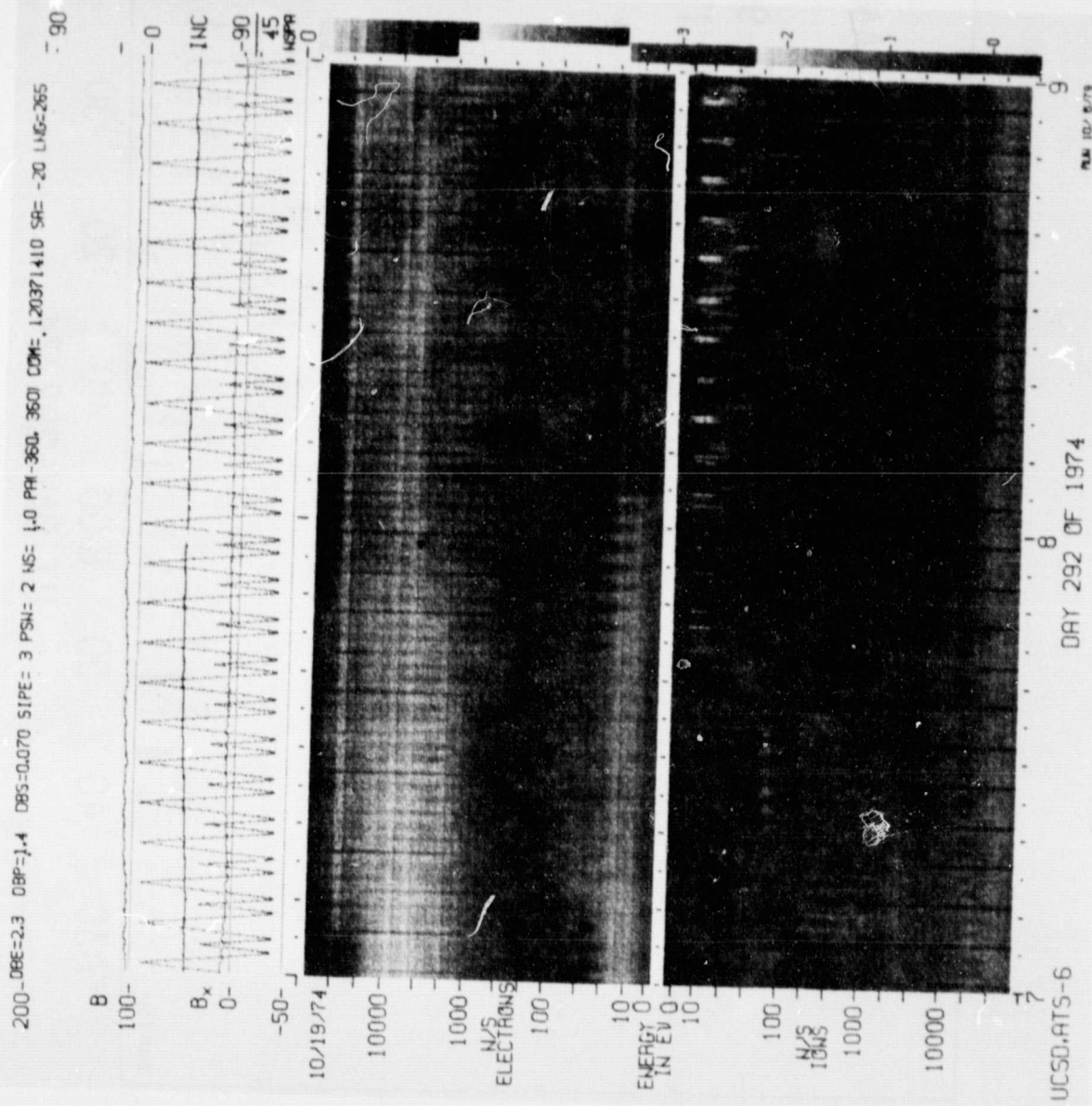


FIGURE 59

ORIGINAL PAGE IS
OF POOR QUALITY

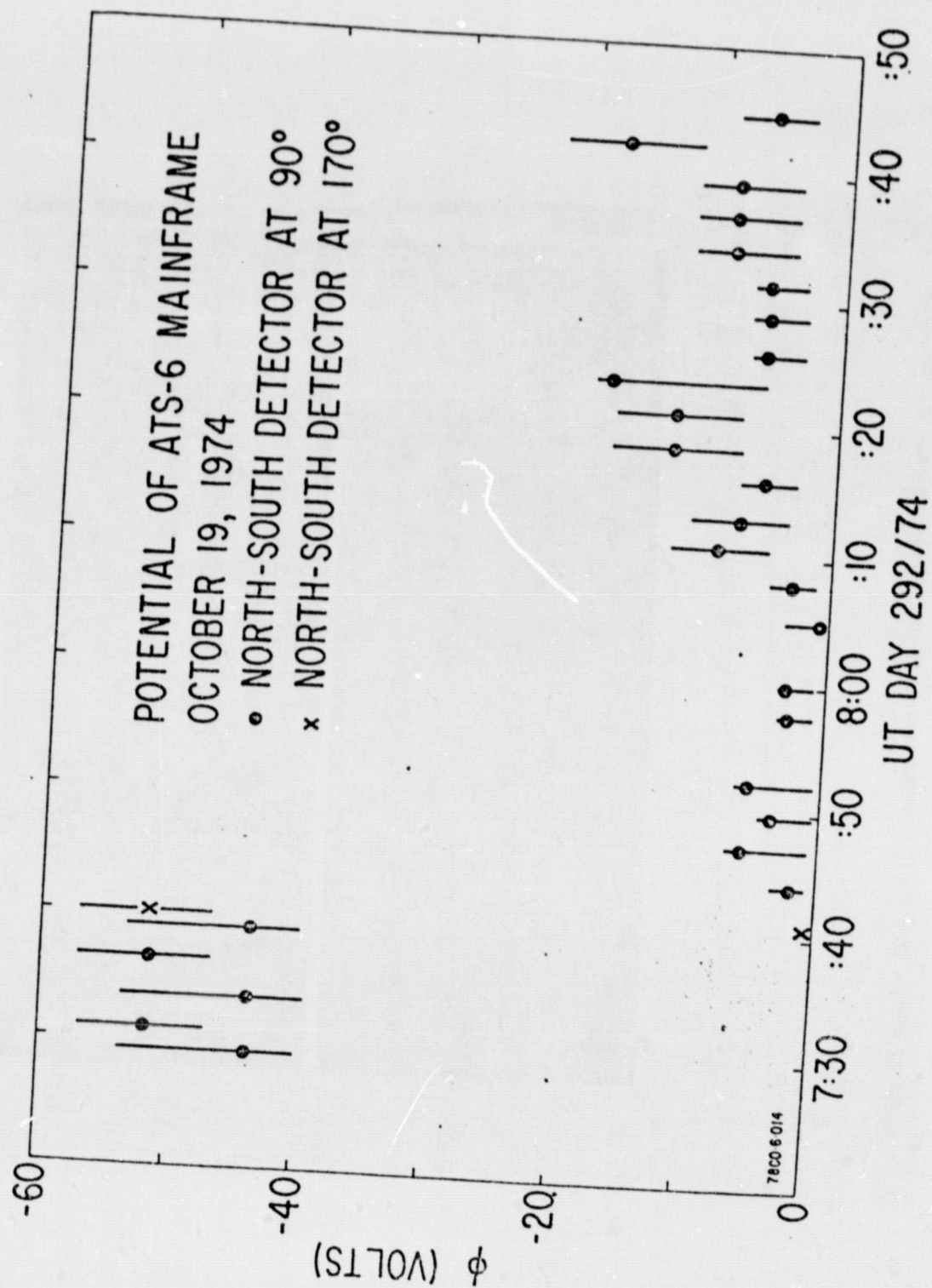


FIGURE 60

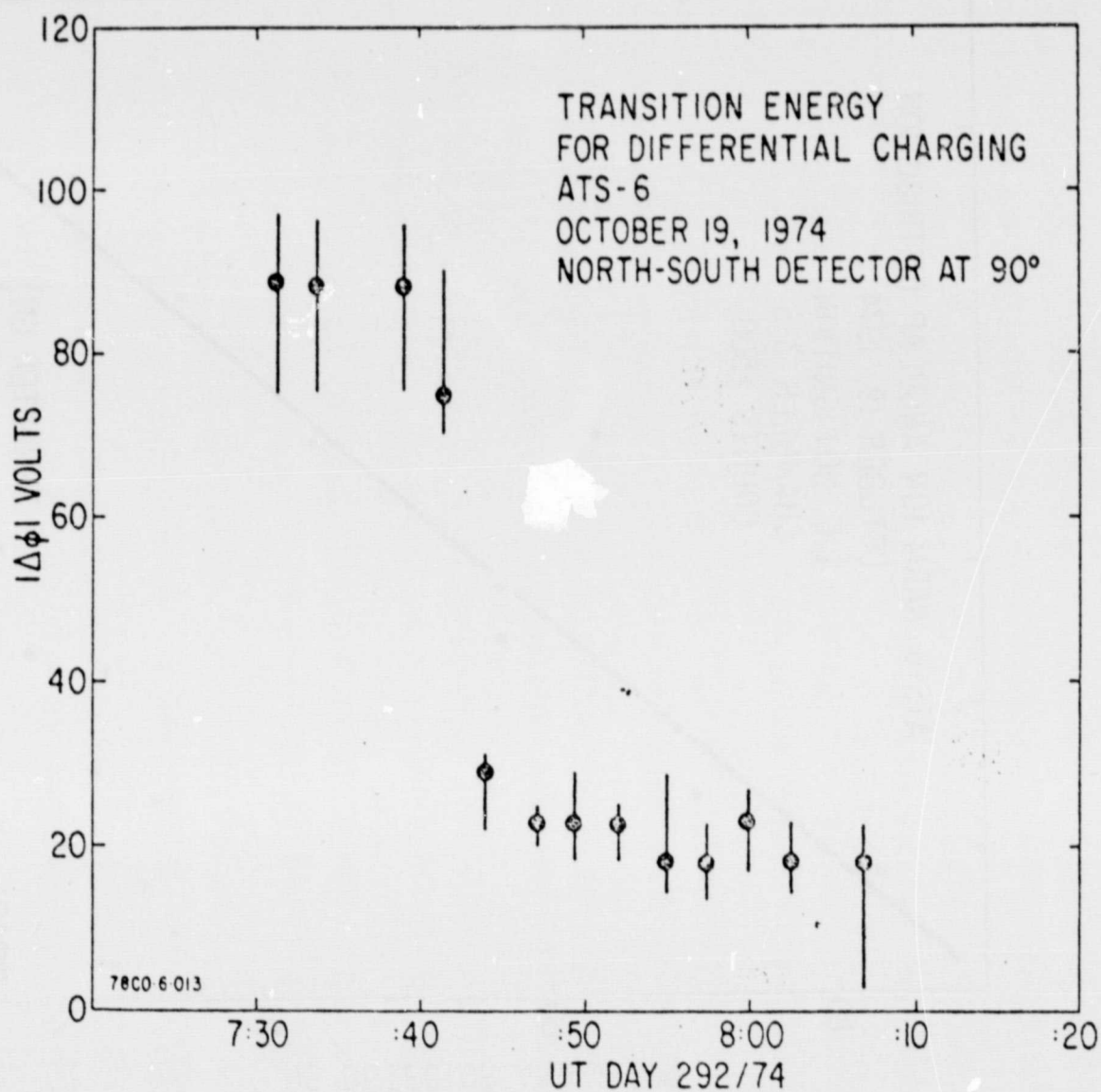


FIGURE 61

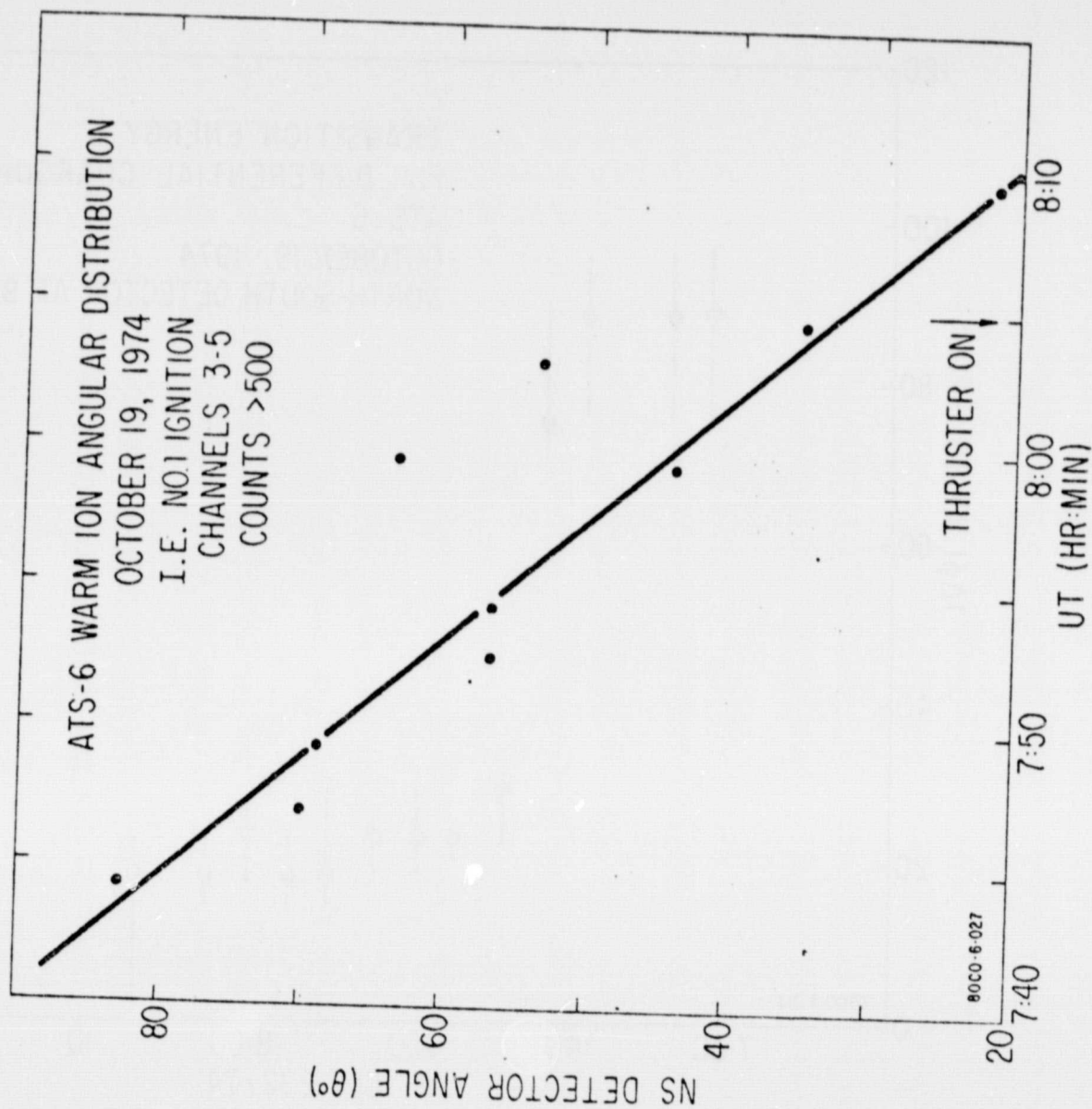


FIGURE 62

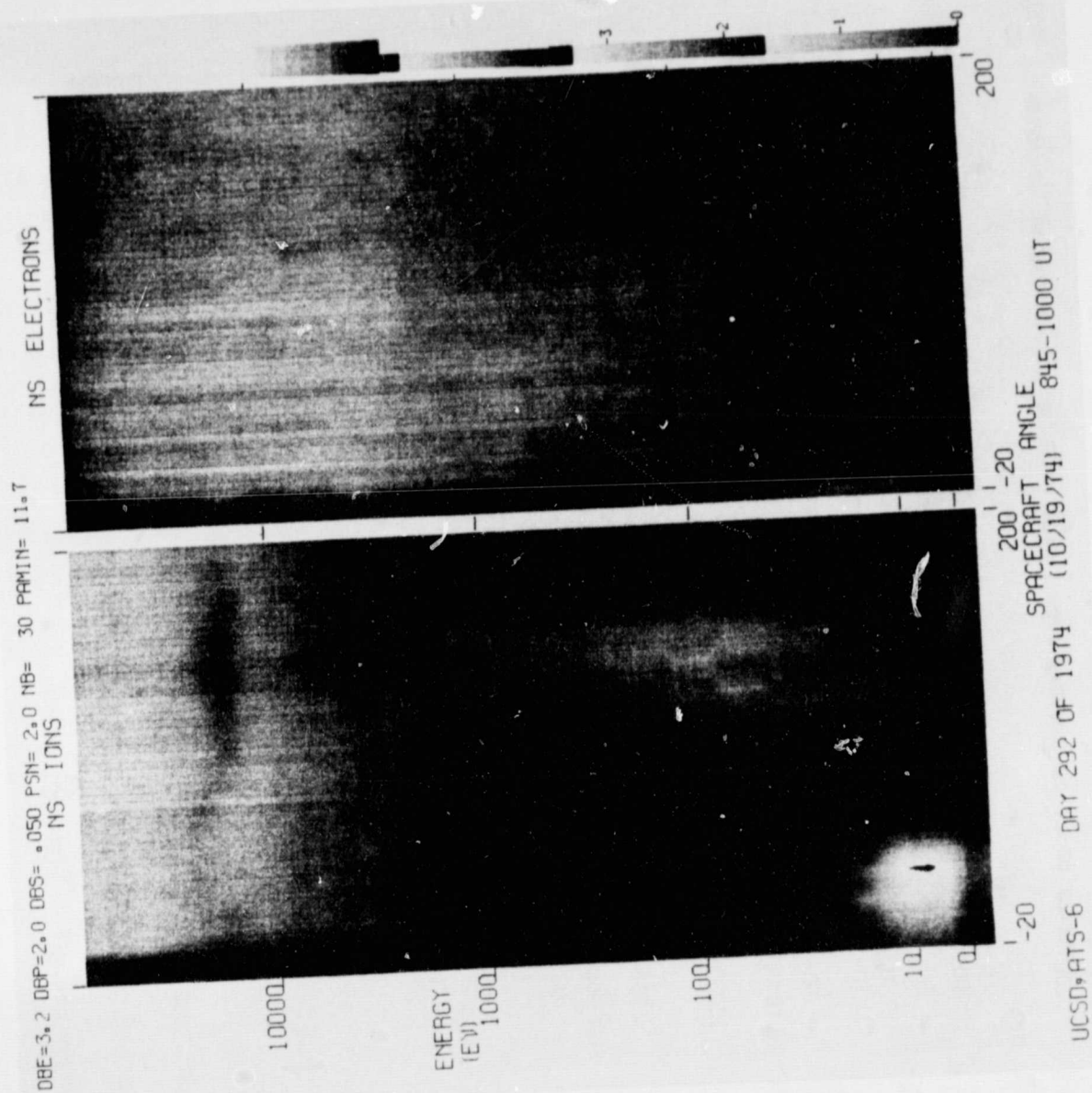


FIGURE 63

ORIGINAL PAGE IS
OF POOR QUALITY

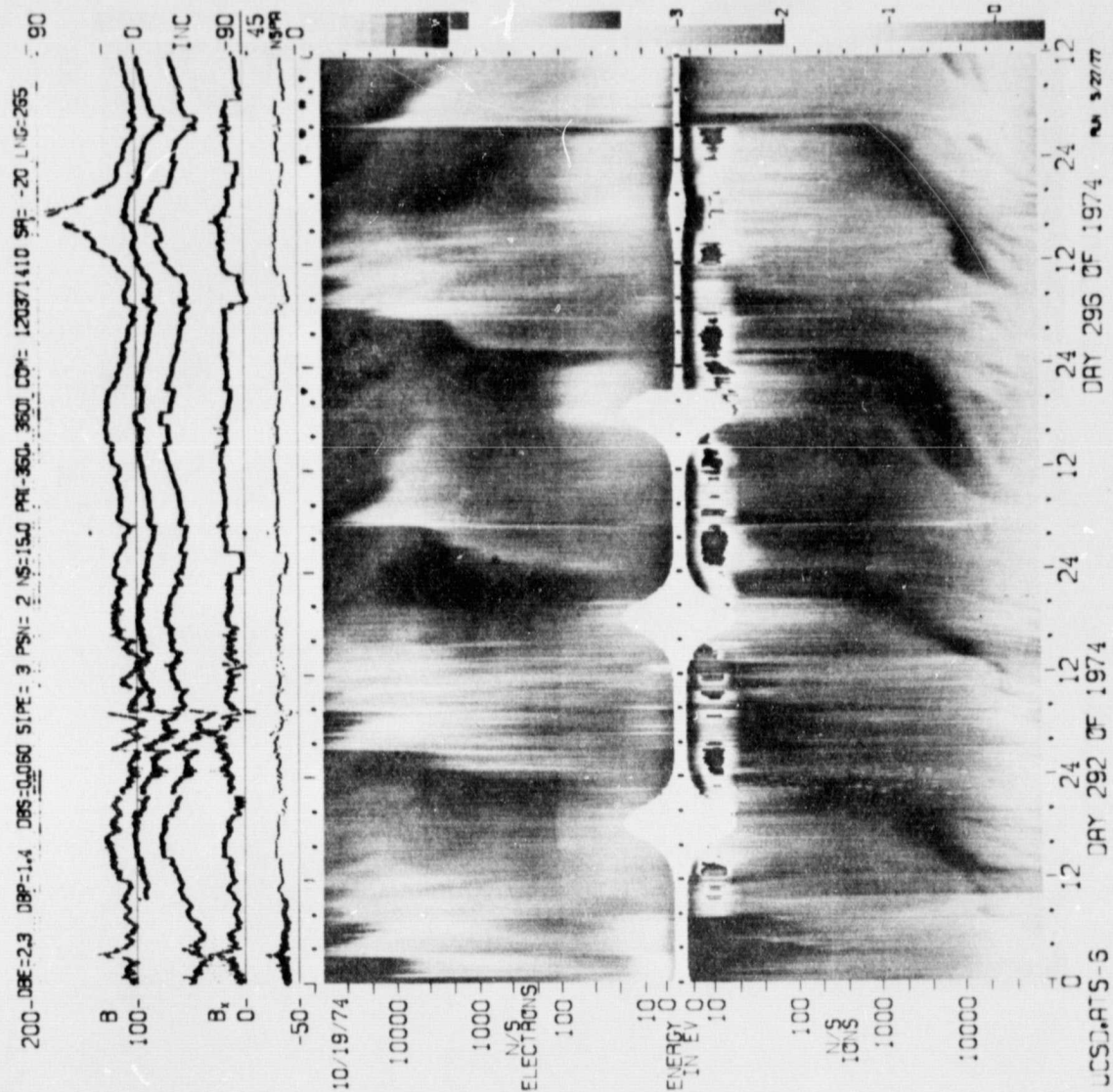


FIGURE 64

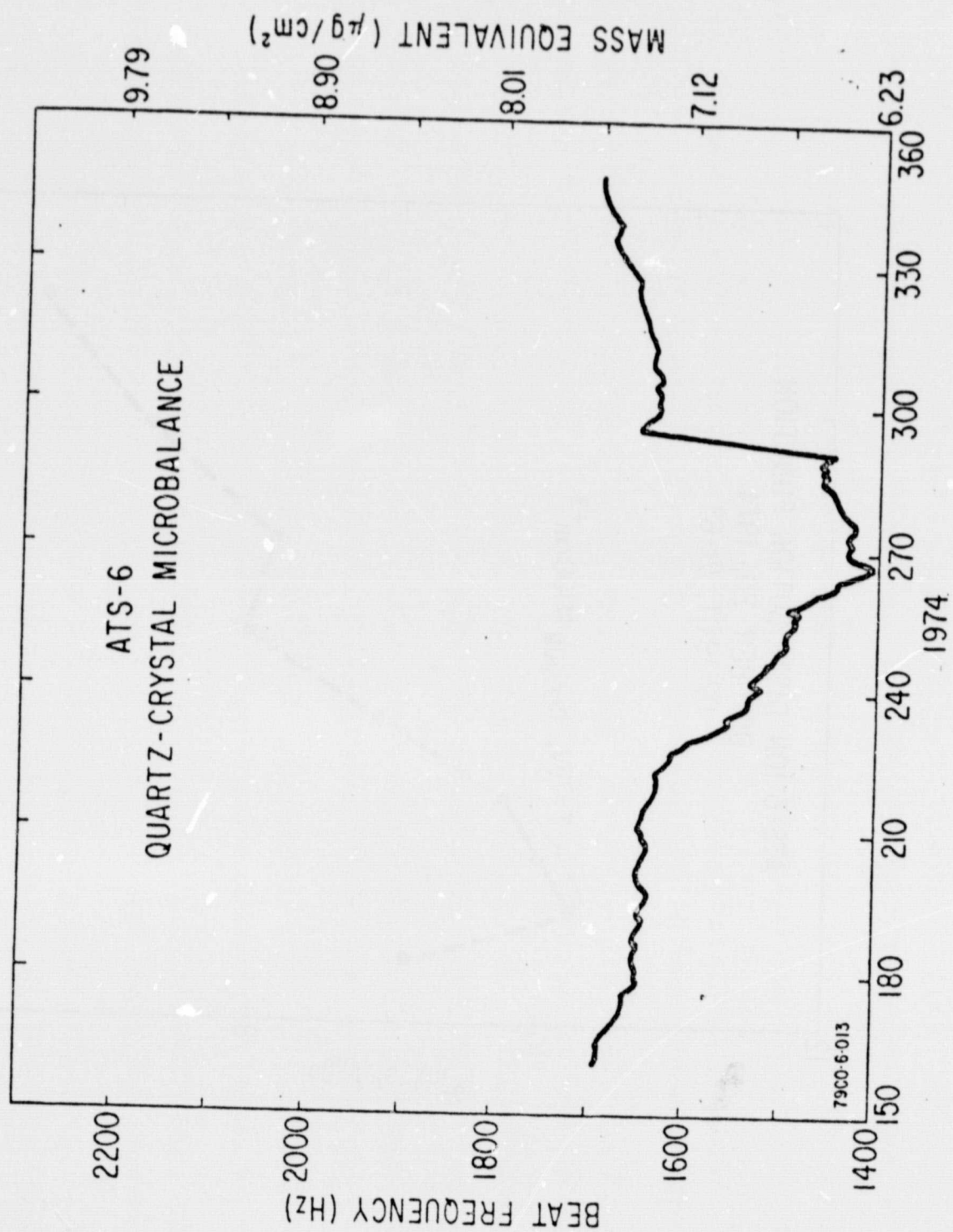


FIGURE 65

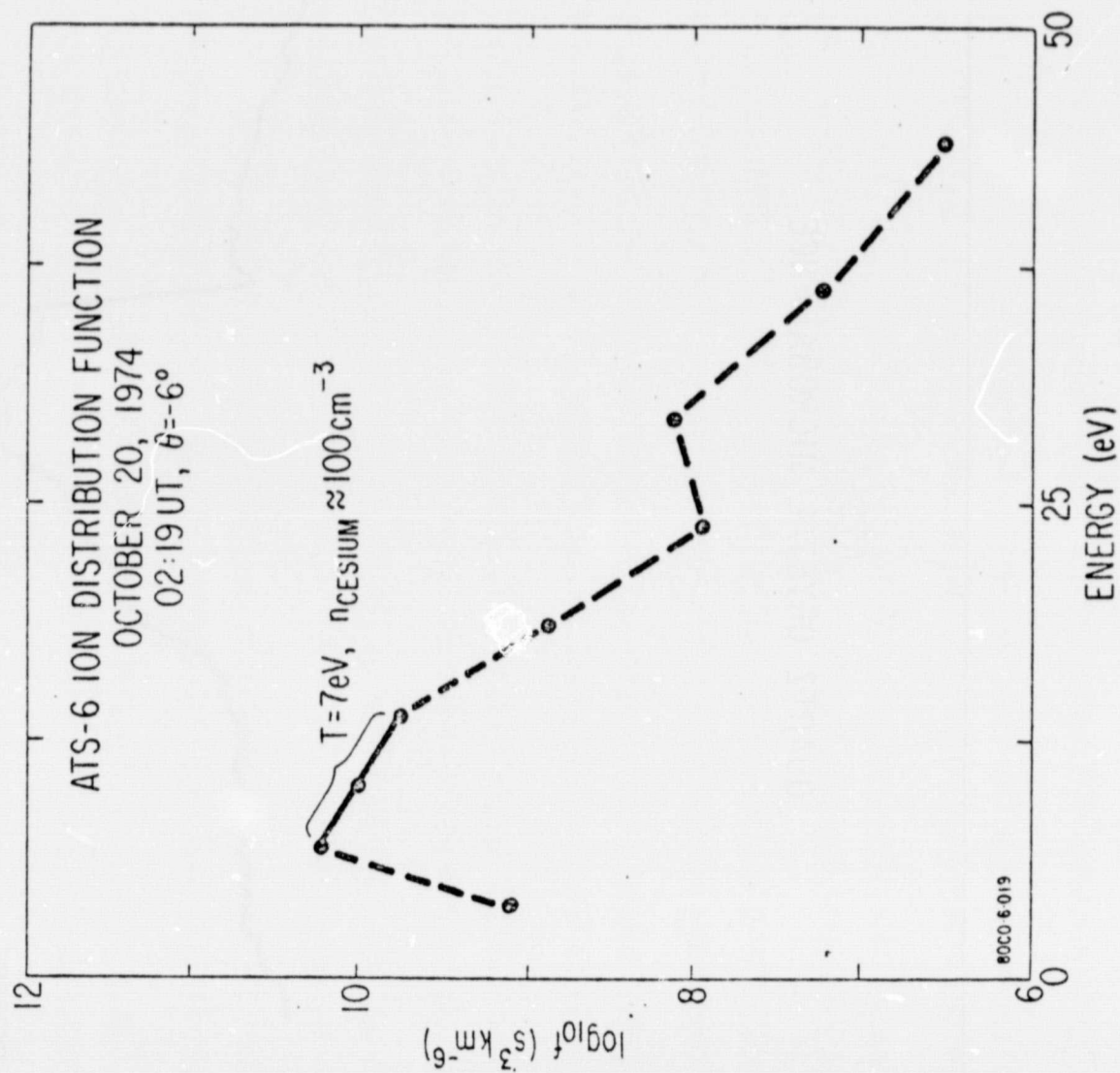


FIGURE 66

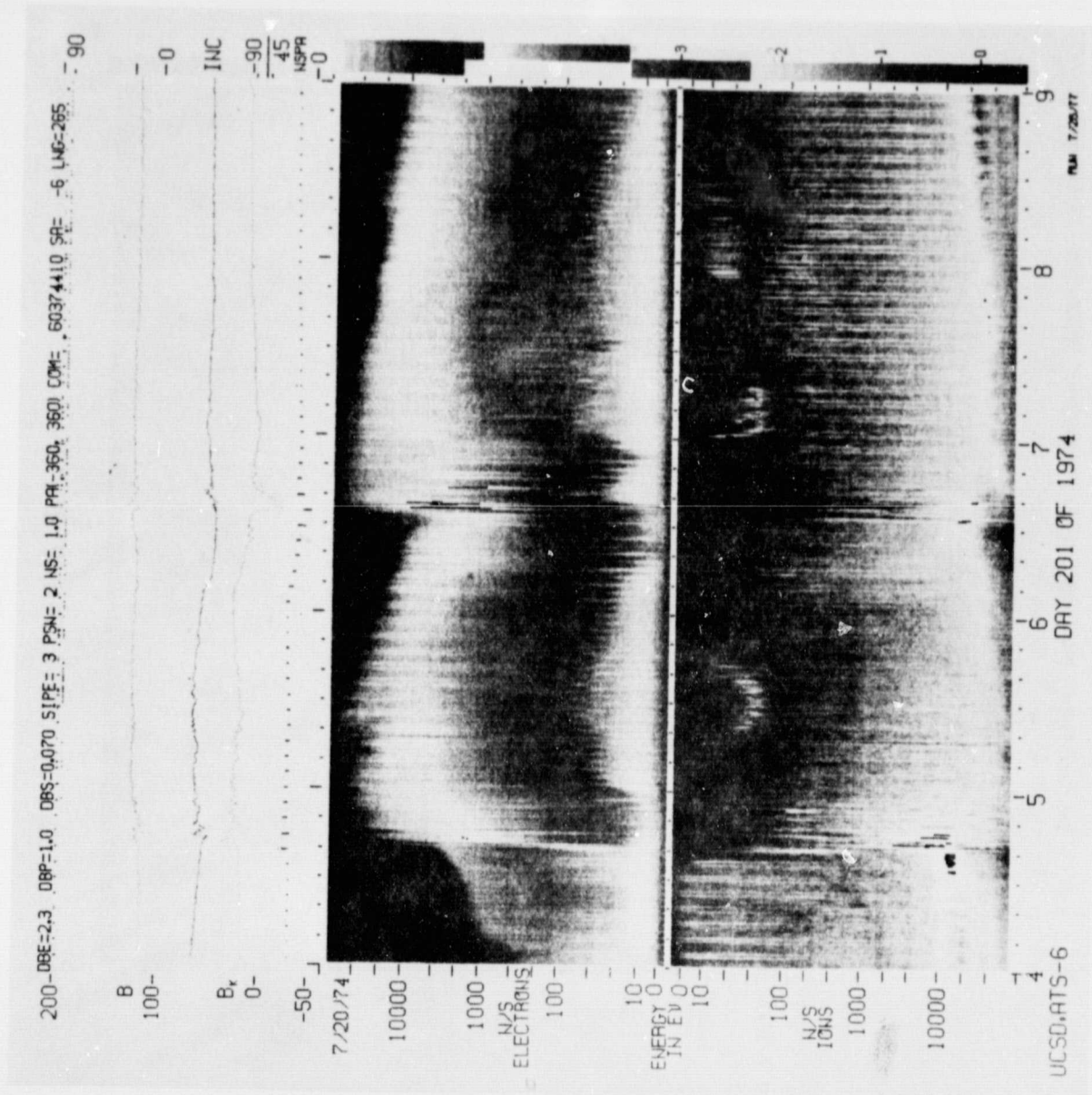


FIGURE 67

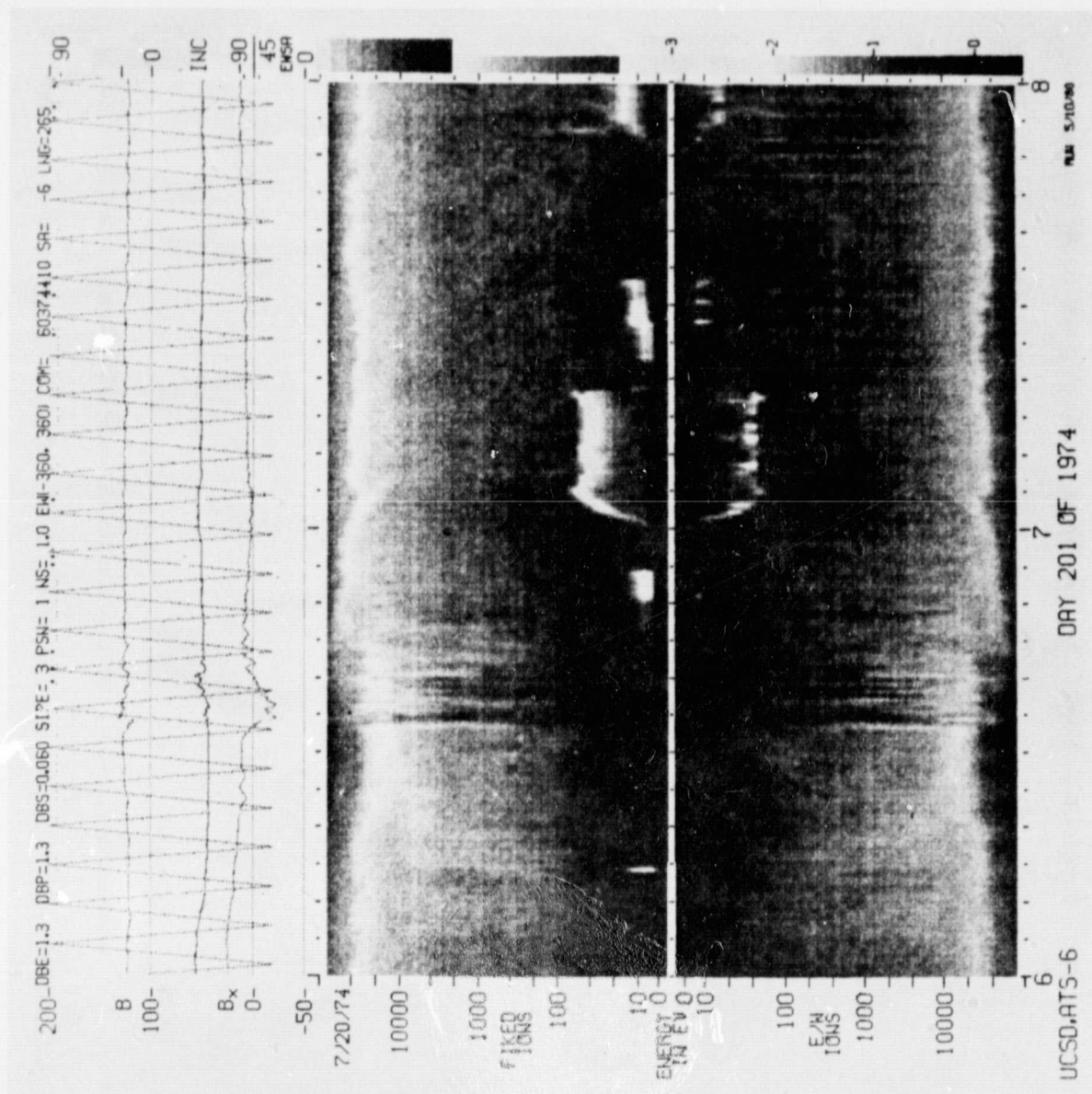


FIGURE 63

ORIGINAL PAGE IS
OF POOR QUALITY

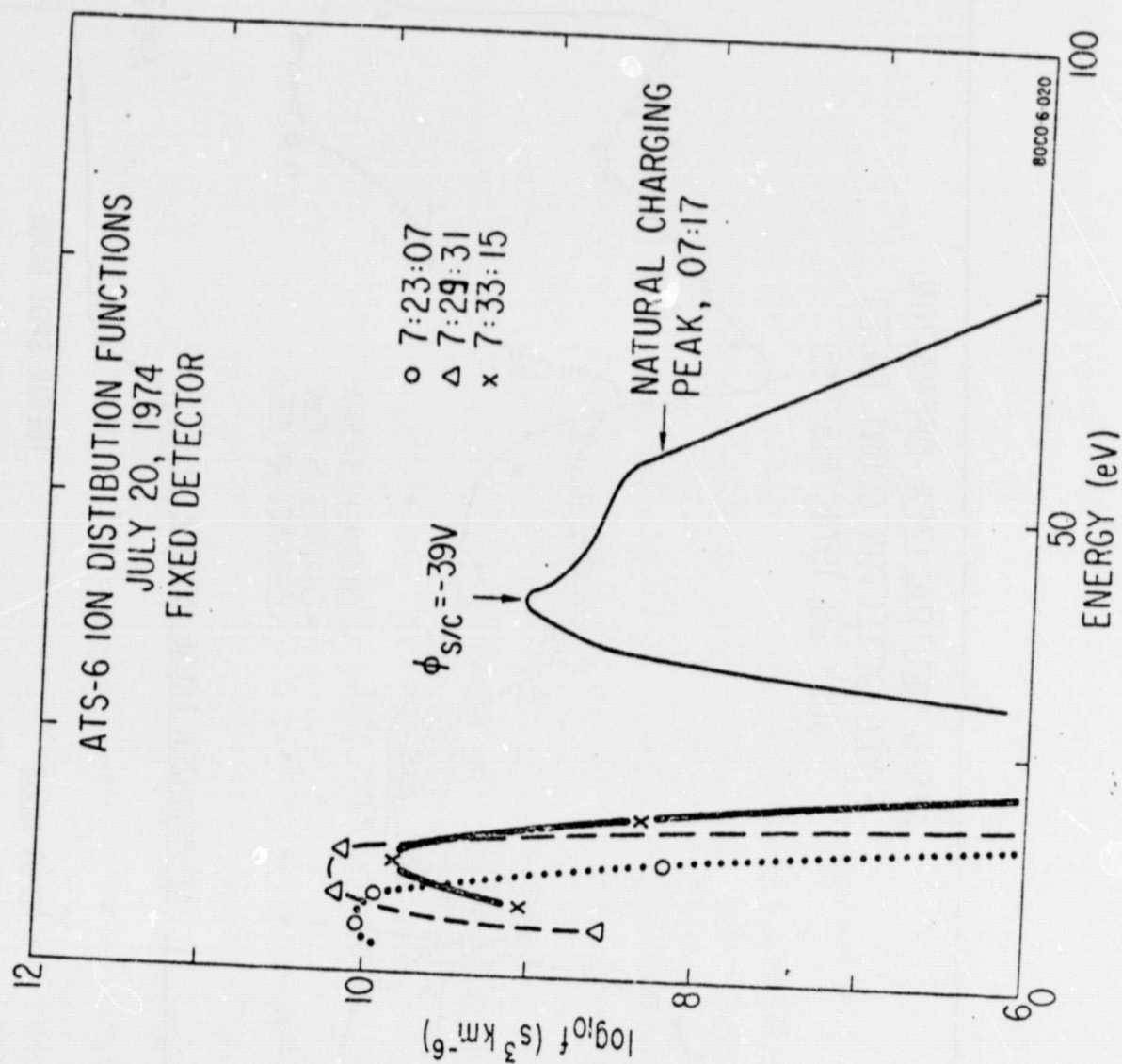


FIGURE 69

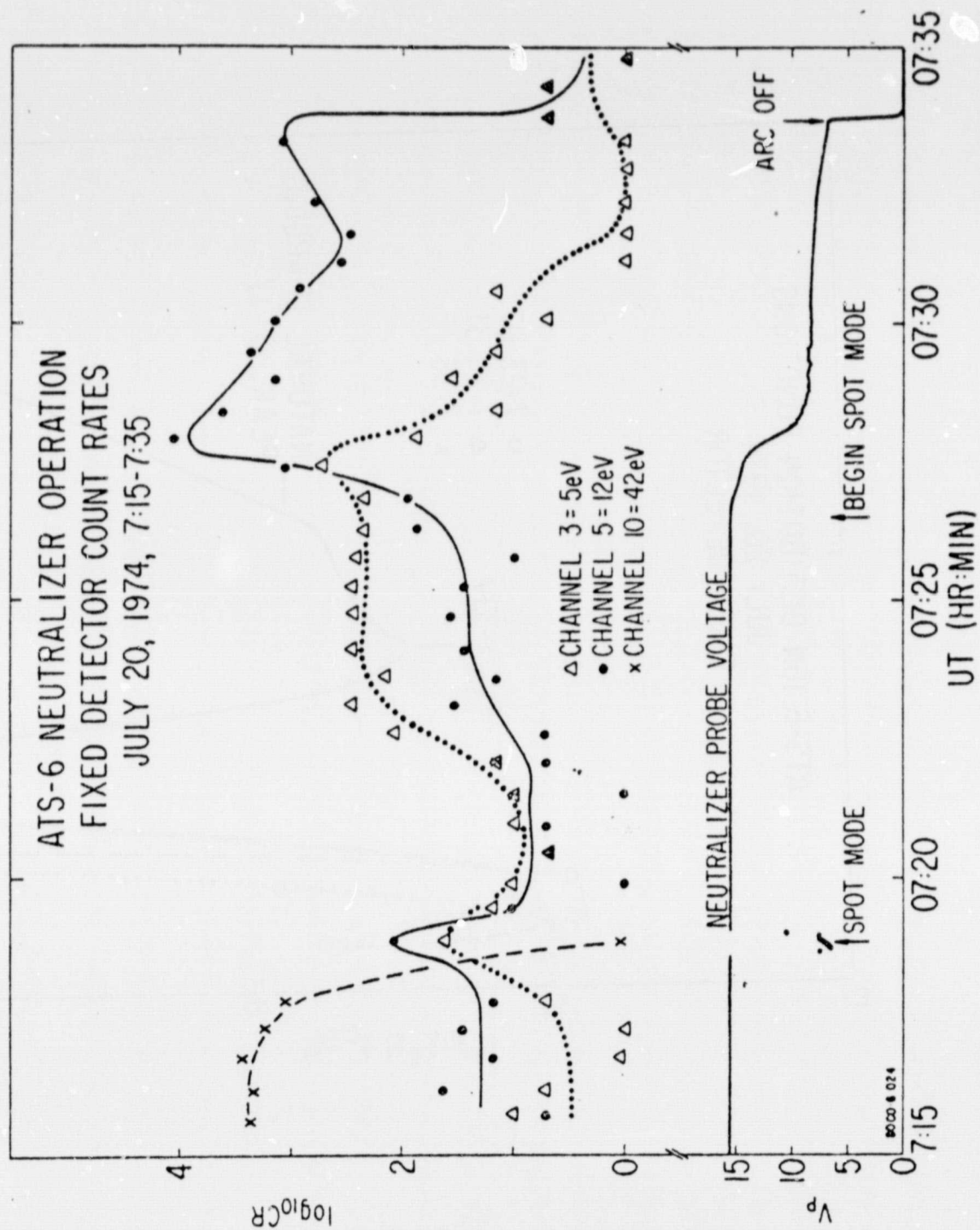


FIGURE 70

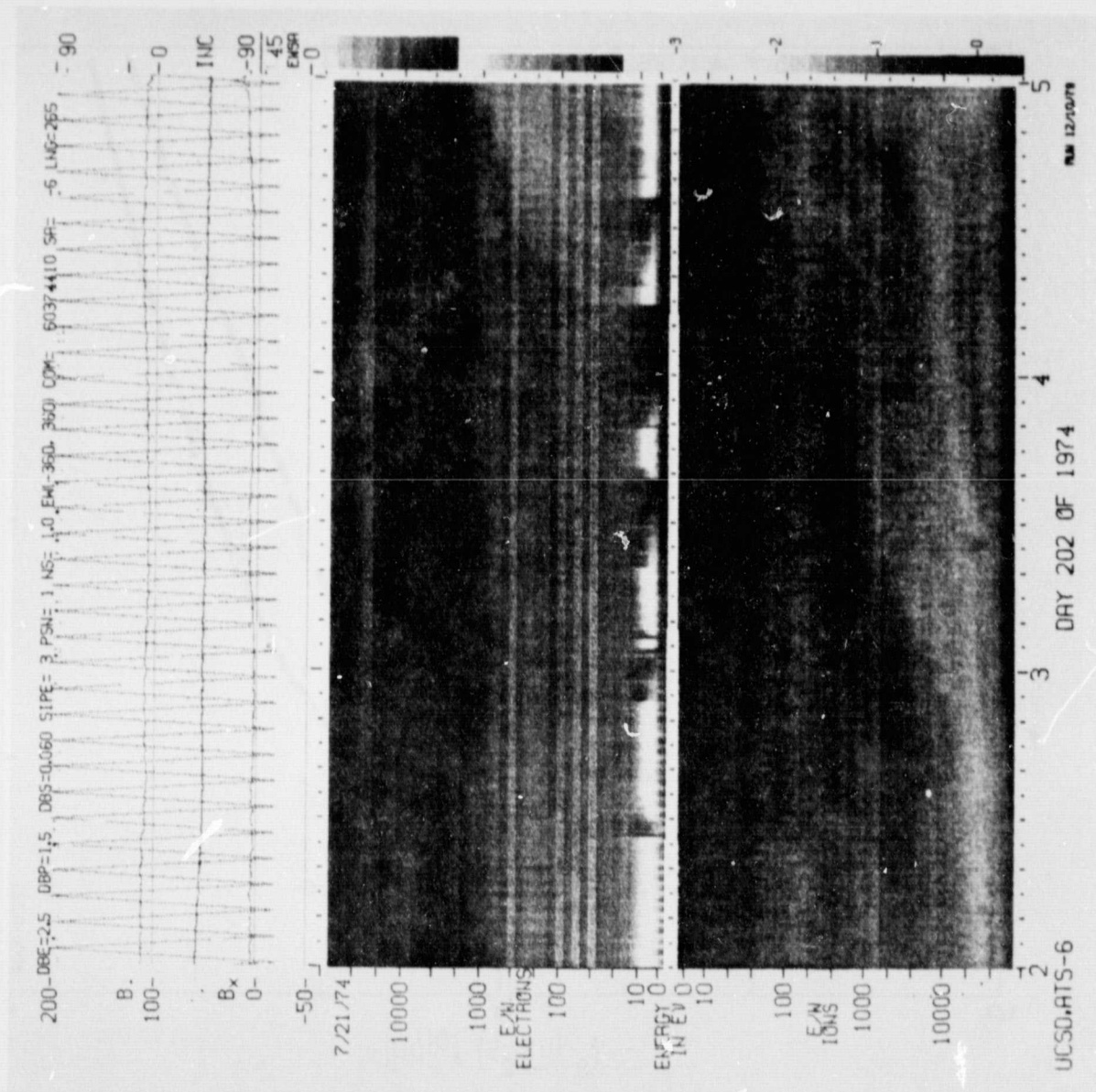


FIGURE 71

ORIGINAL PAGE IS
OF POOR QUALITY

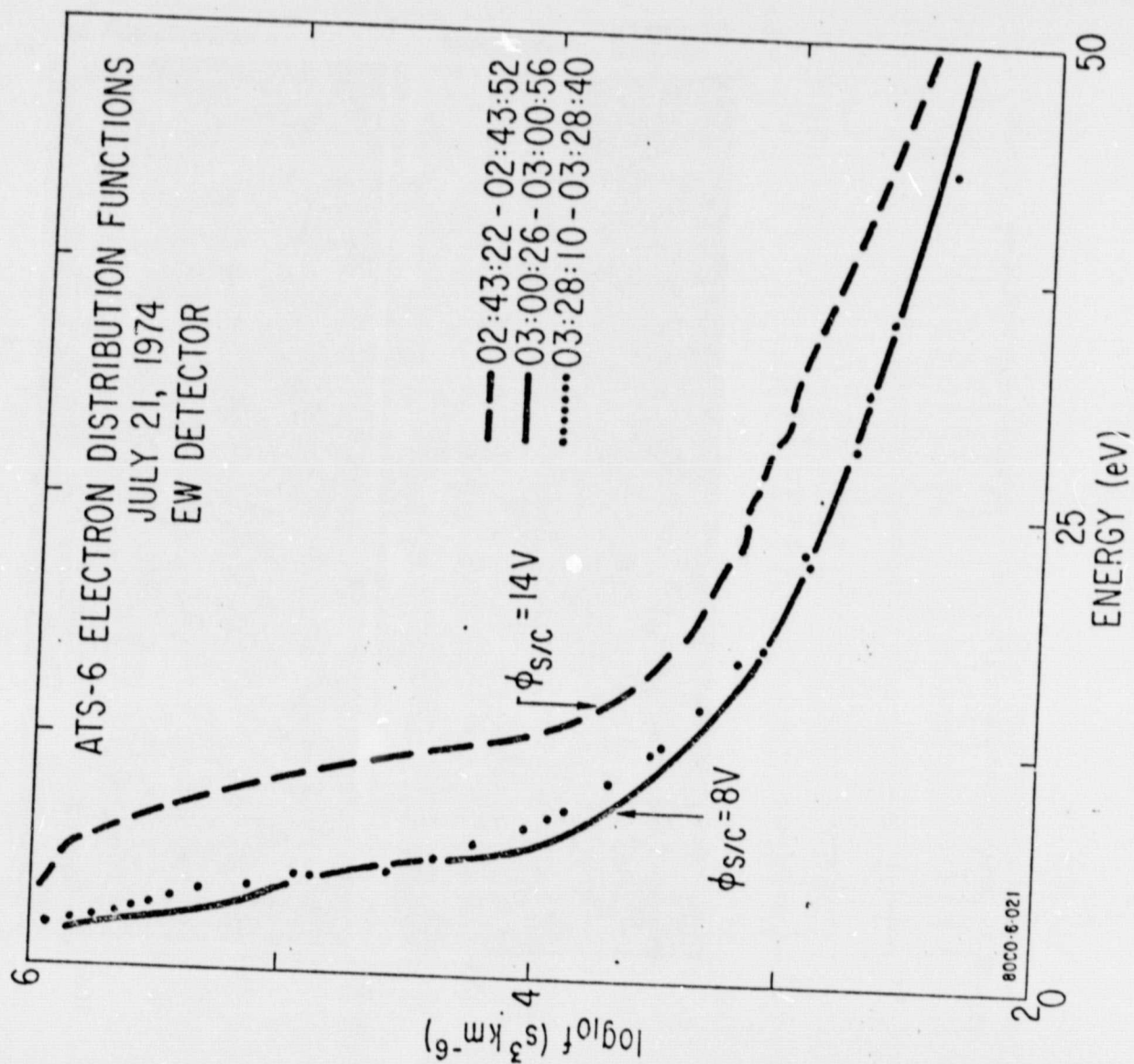


FIGURE 72

ATS-6 NEUTRALIZER OPERATION JULY 21, 1974

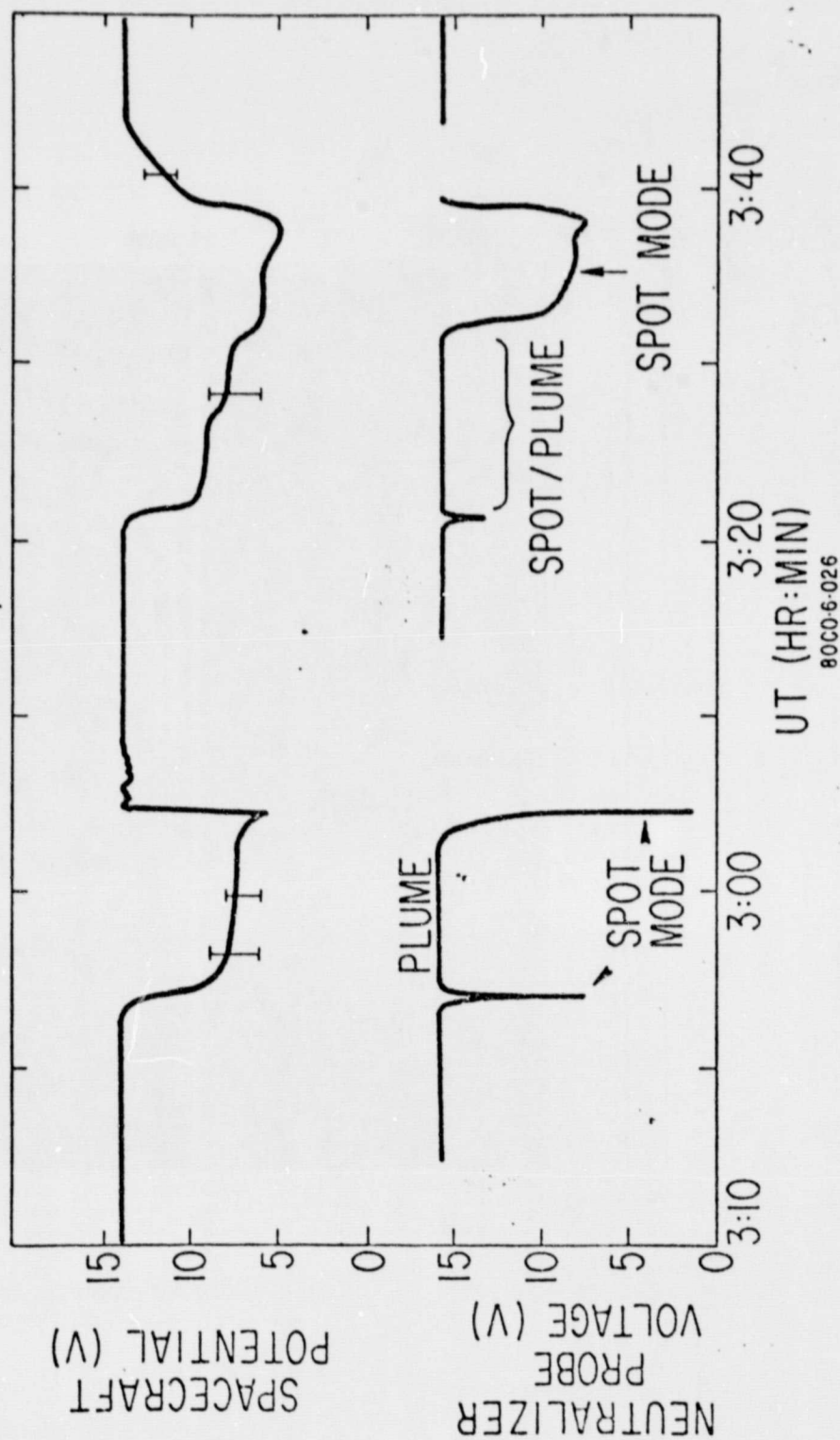


FIGURE 73

200-DBE=1.8 DBP=1.4 DBS=0.070 S1PE= 3 PSN= 2 NS= 1.0 PRI=360.360Q COM= 20572404 SR= -6 LUG=28: 90

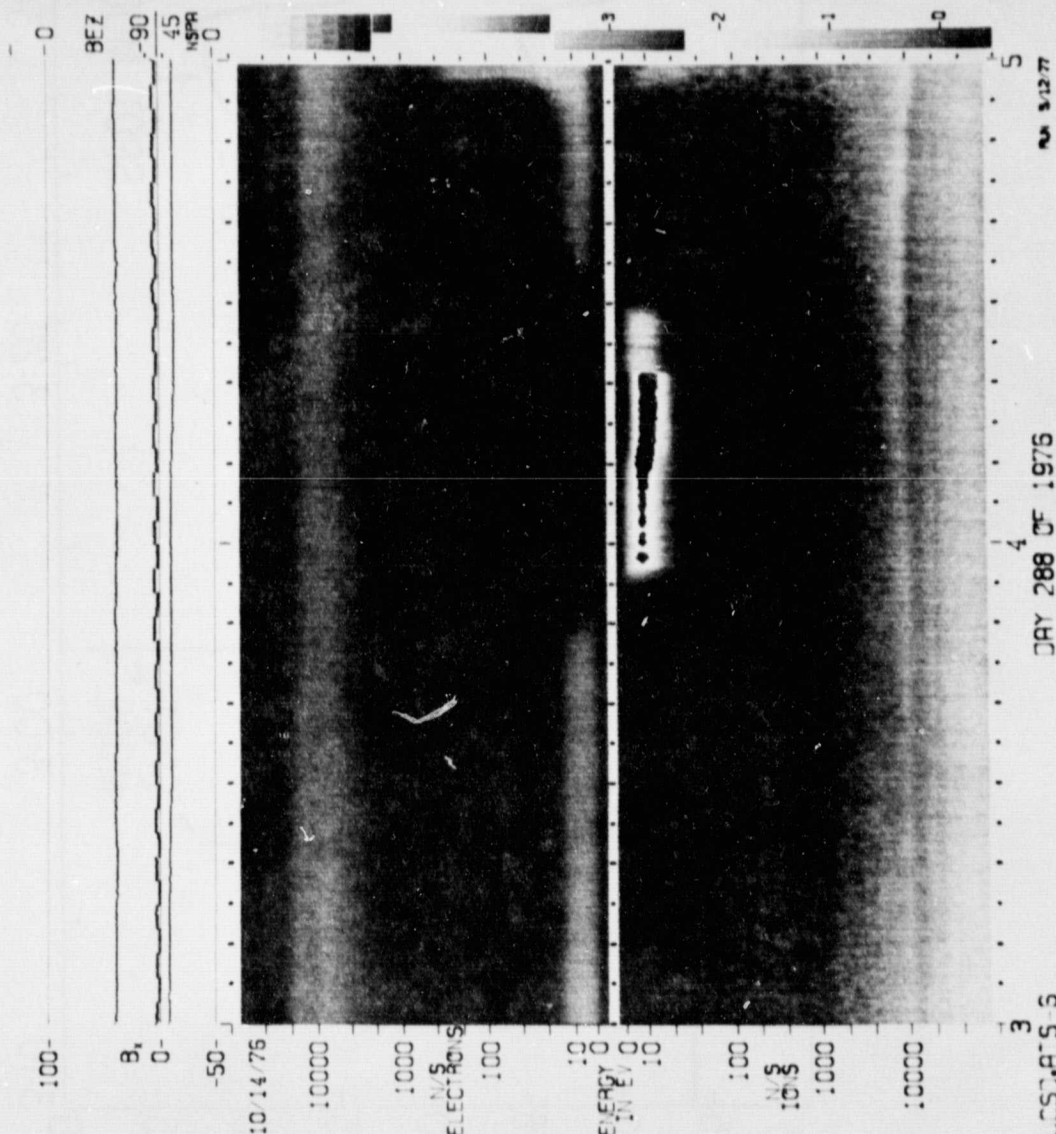


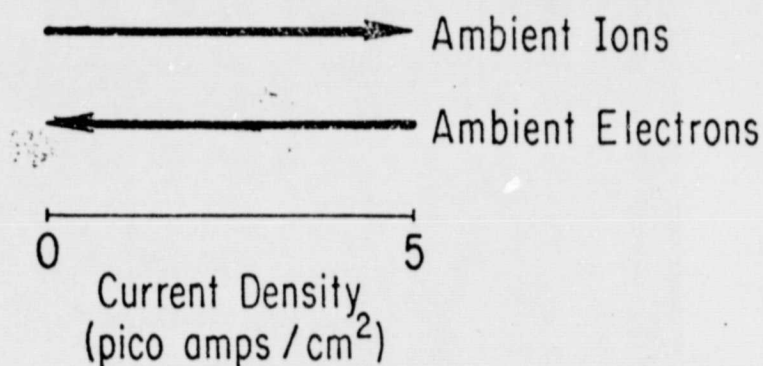
FIGURE 74

ORIGINAL PAGE IS
OF POOR QUALITY

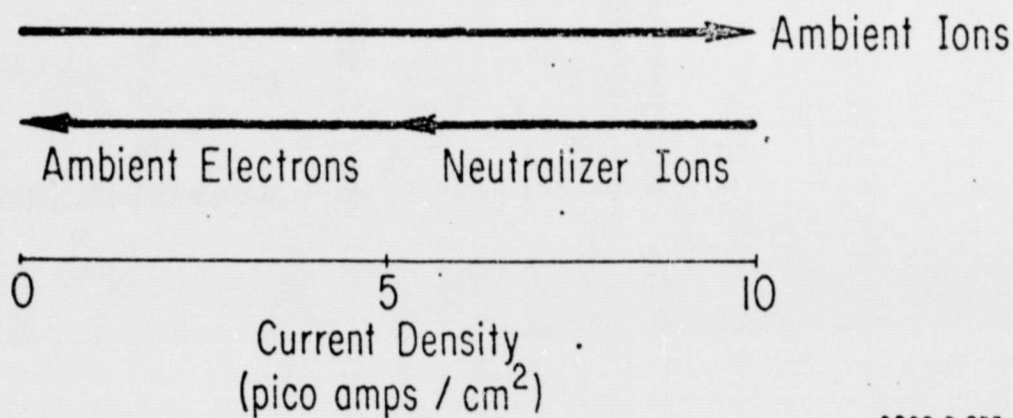
ECLIPSE CURRENT BALANCE

QUIET TIME

NEUTRALIZER OFF



NEUTRALIZER ON



80CO-6-033

FIGURE 75

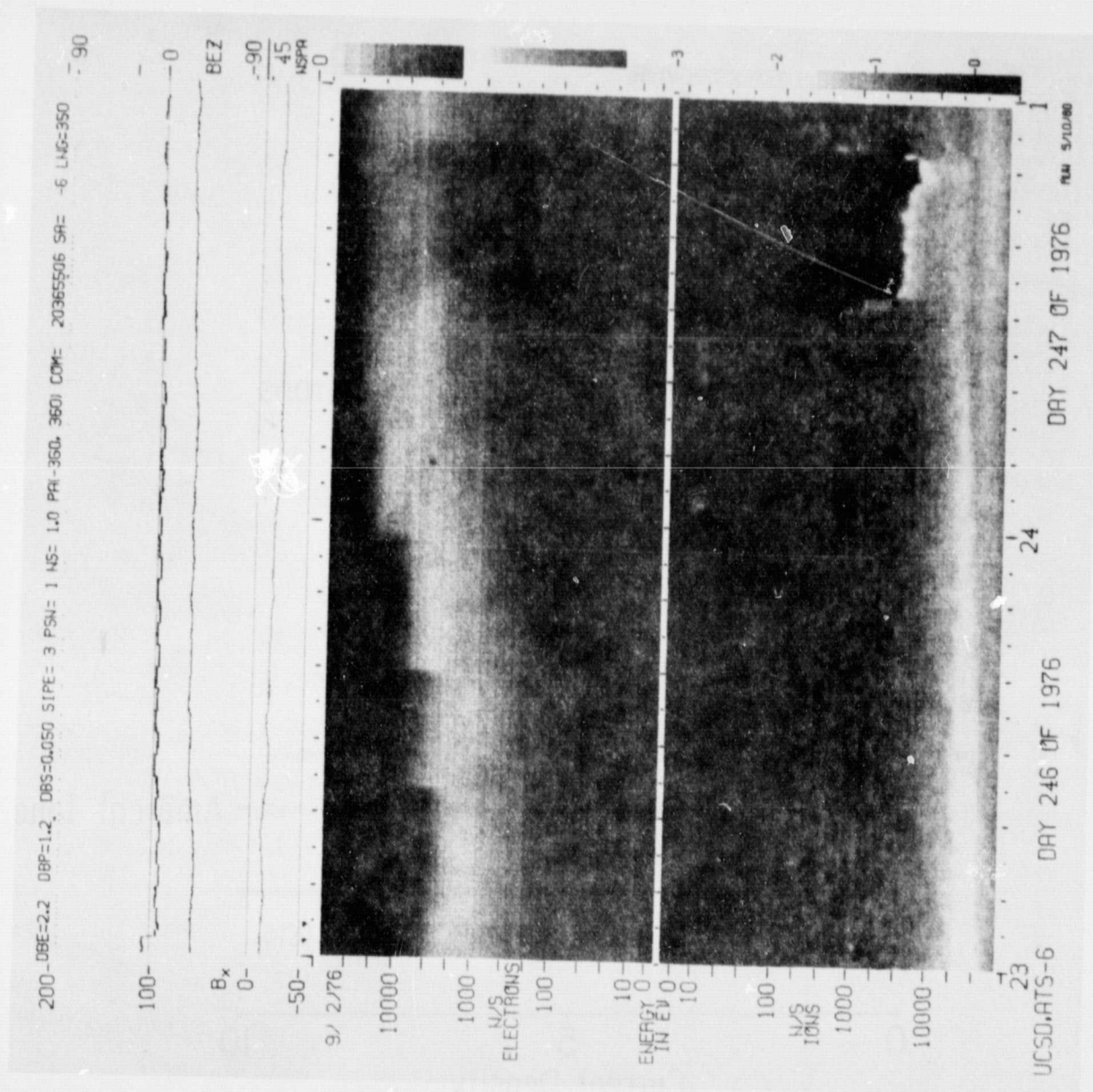


FIGURE 76

ATS-6 NEUTRALIZER/ECLIPSE OPERATION
DAY 97/77

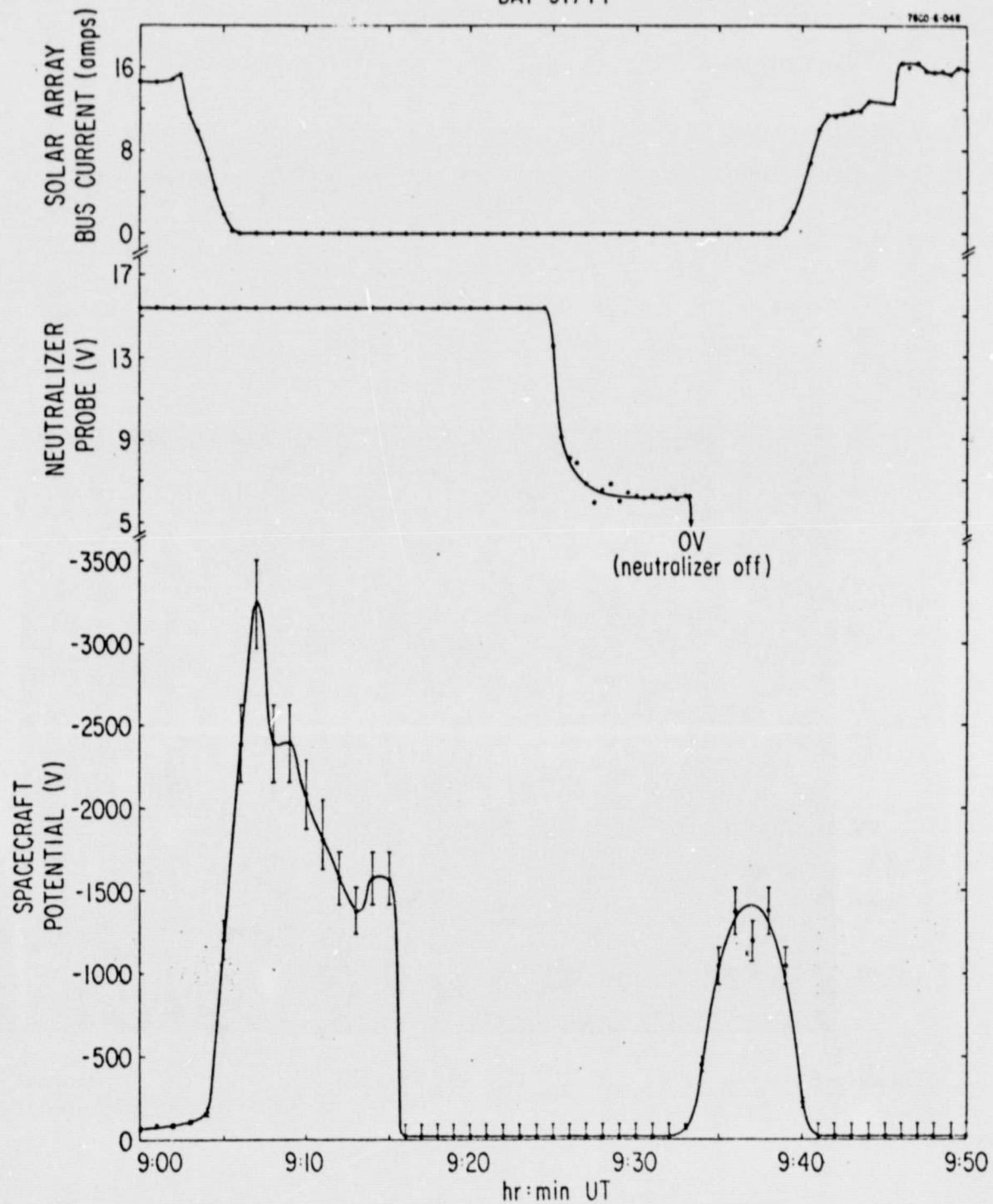


FIGURE 77

200-DBE=2.7 DBP=1.7 DBS=0.060 SIPE= 3 PSN= 1 NS= 1.0 PPI=360.360 COM= 120263310 SA= 0 LAG=265. -90

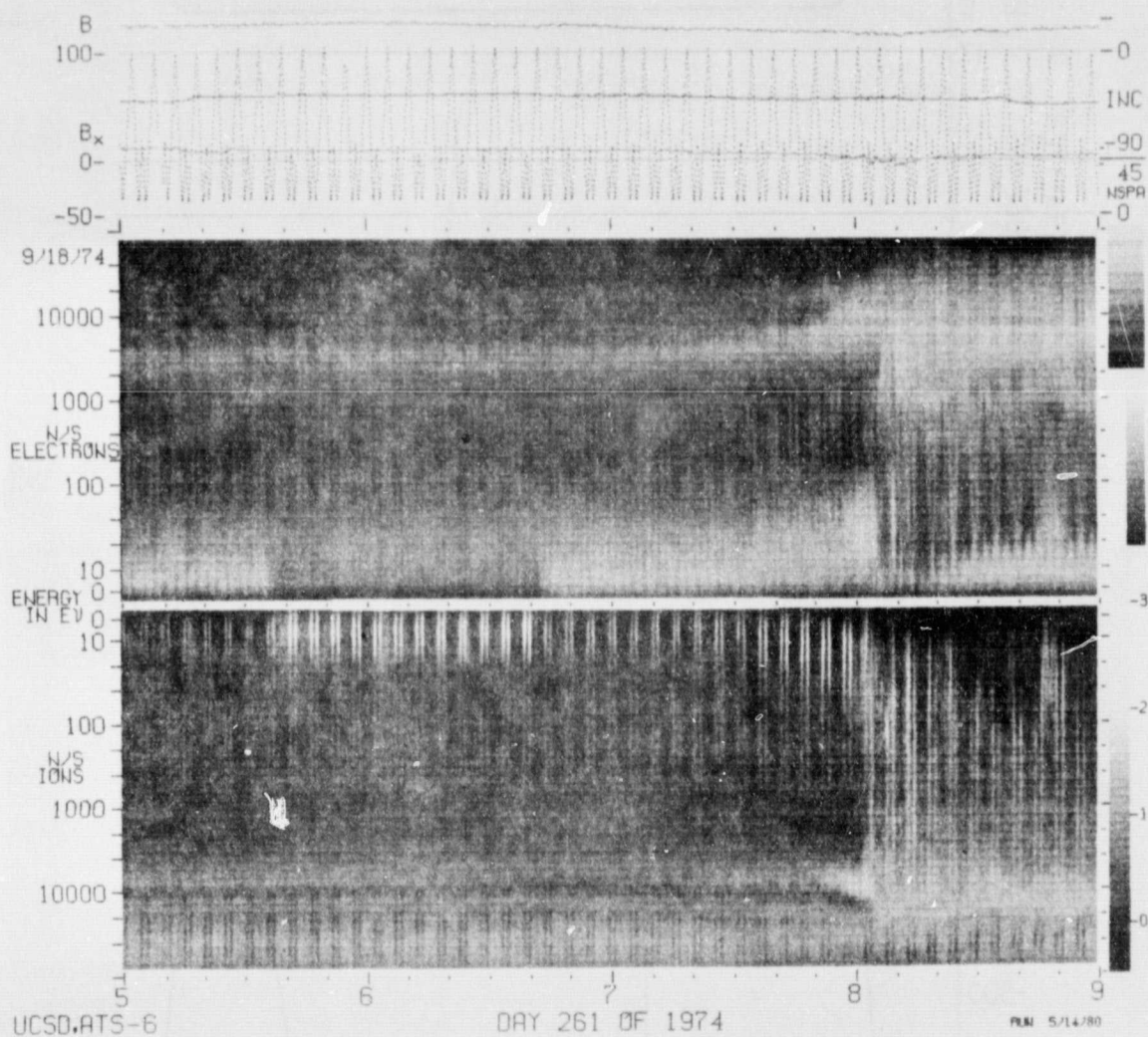


FIGURE 78

ORIGINAL PAGE IS
OF POOR QUALITY

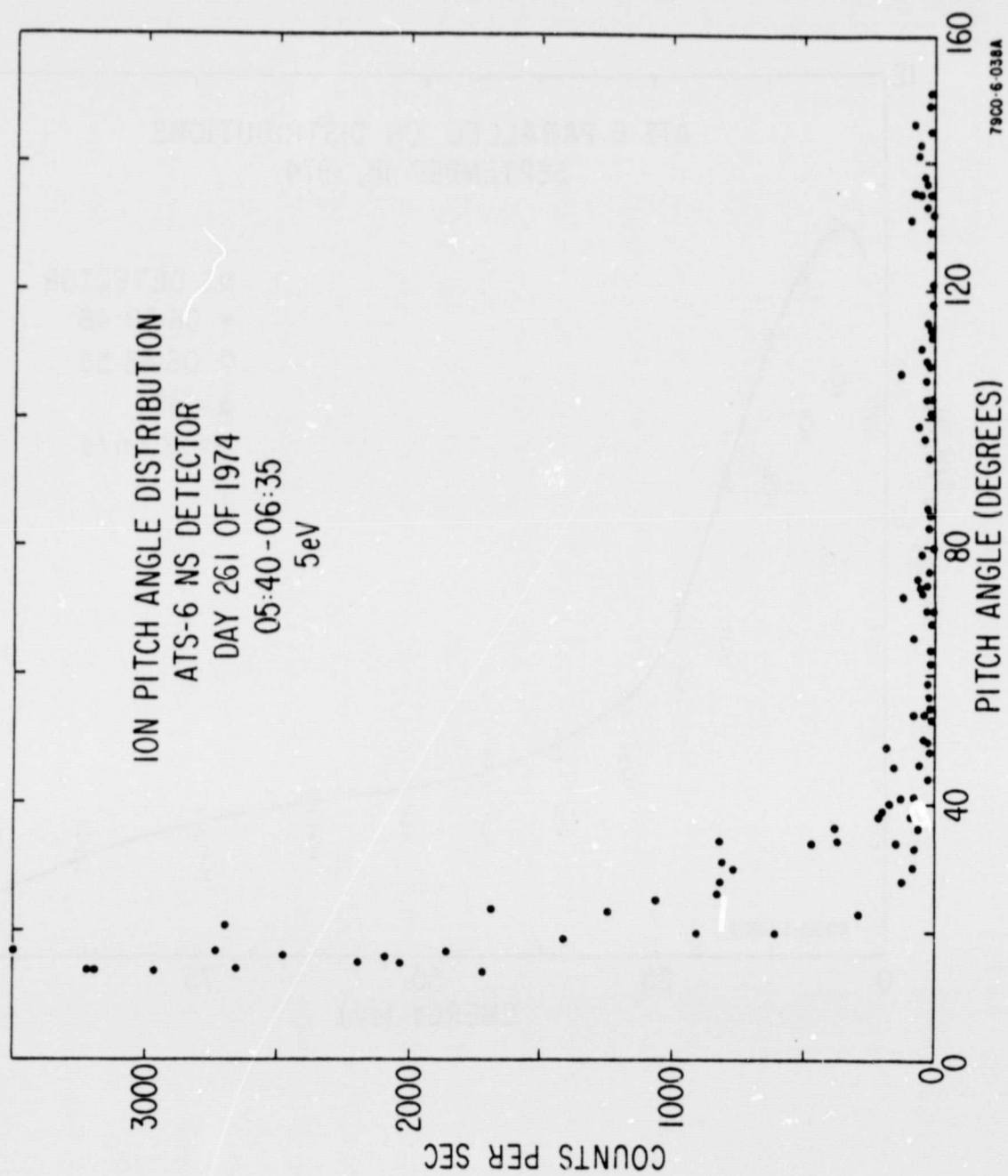


FIGURE 79

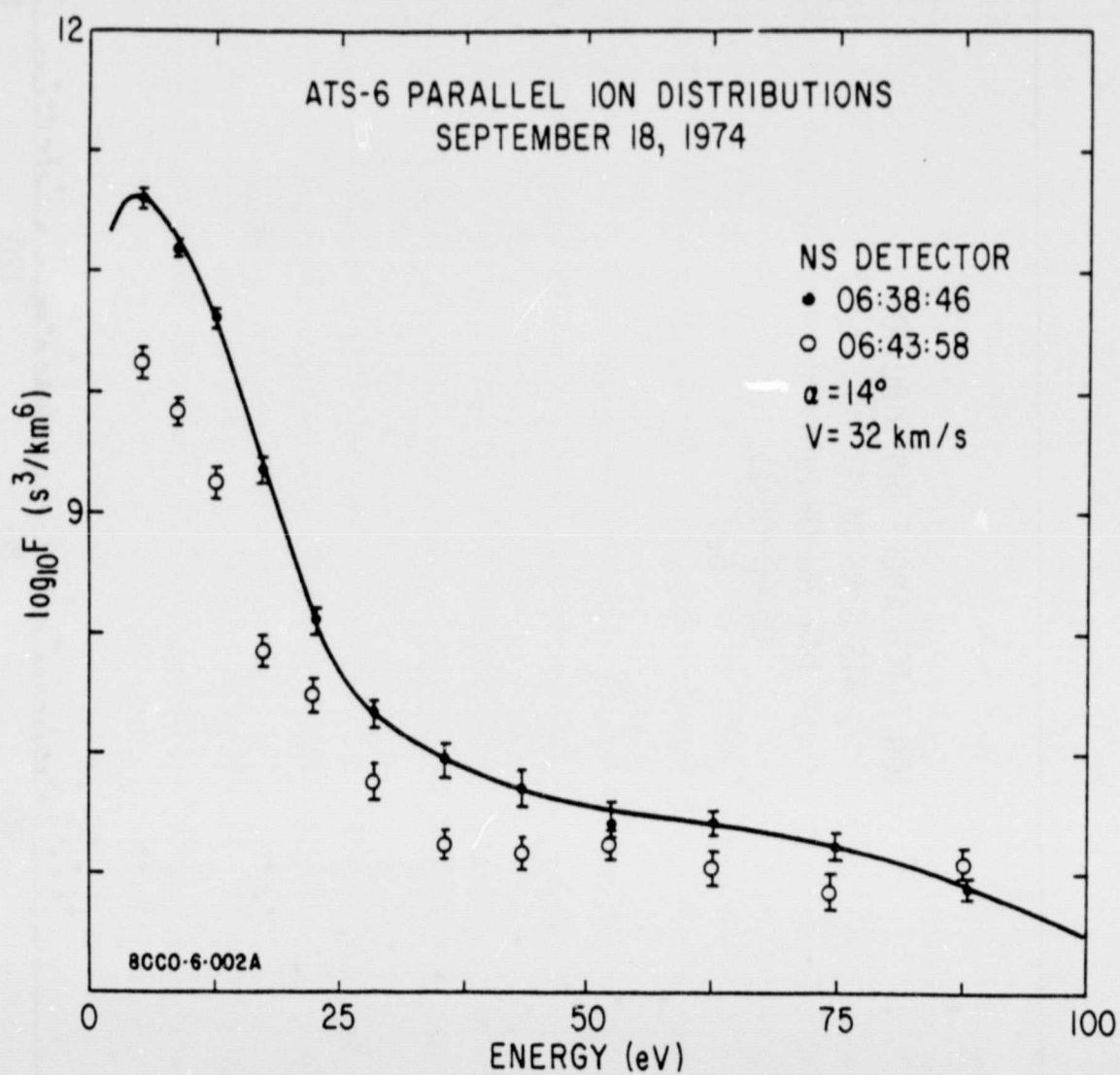


FIGURE 8 0

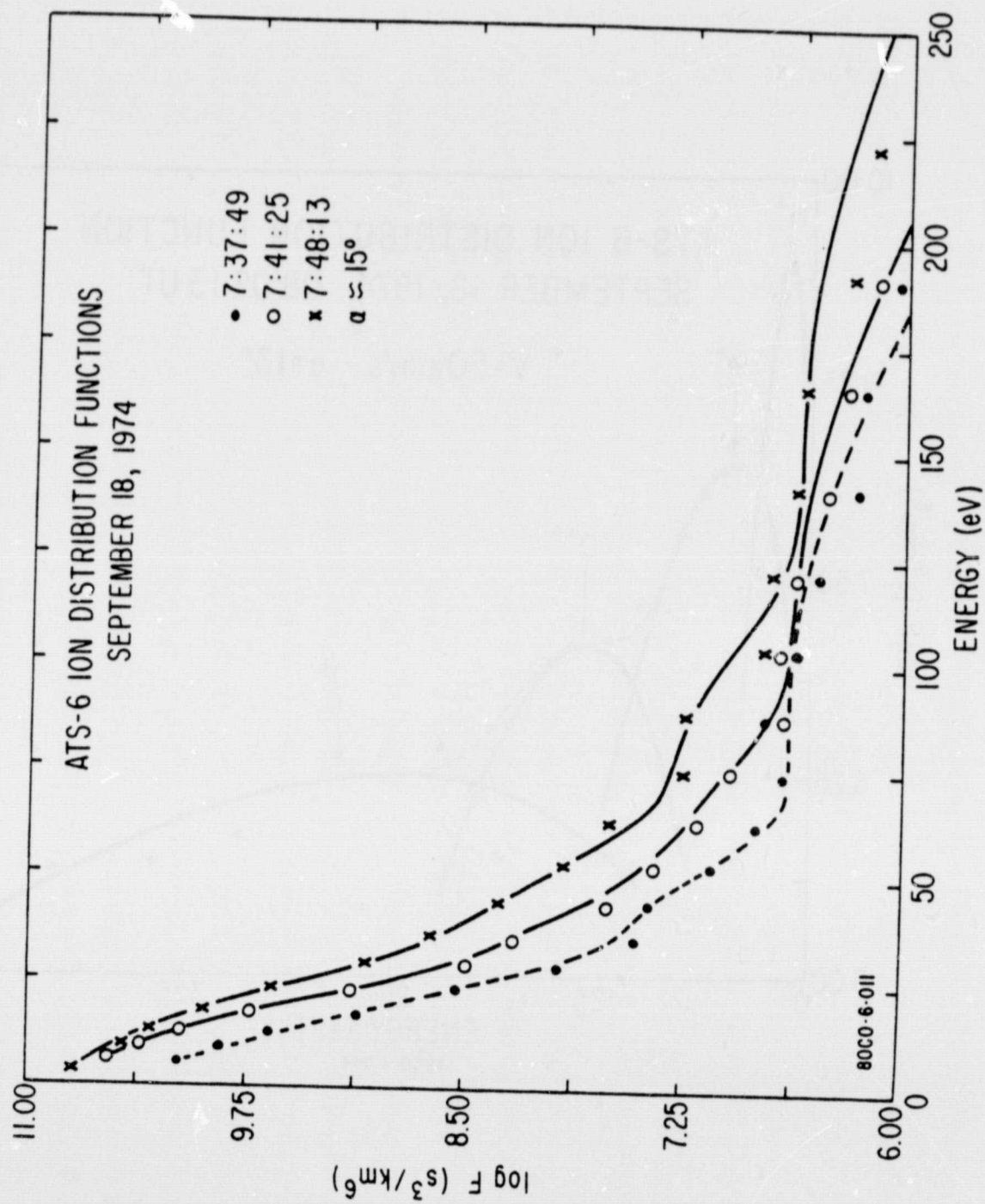


FIGURE 81

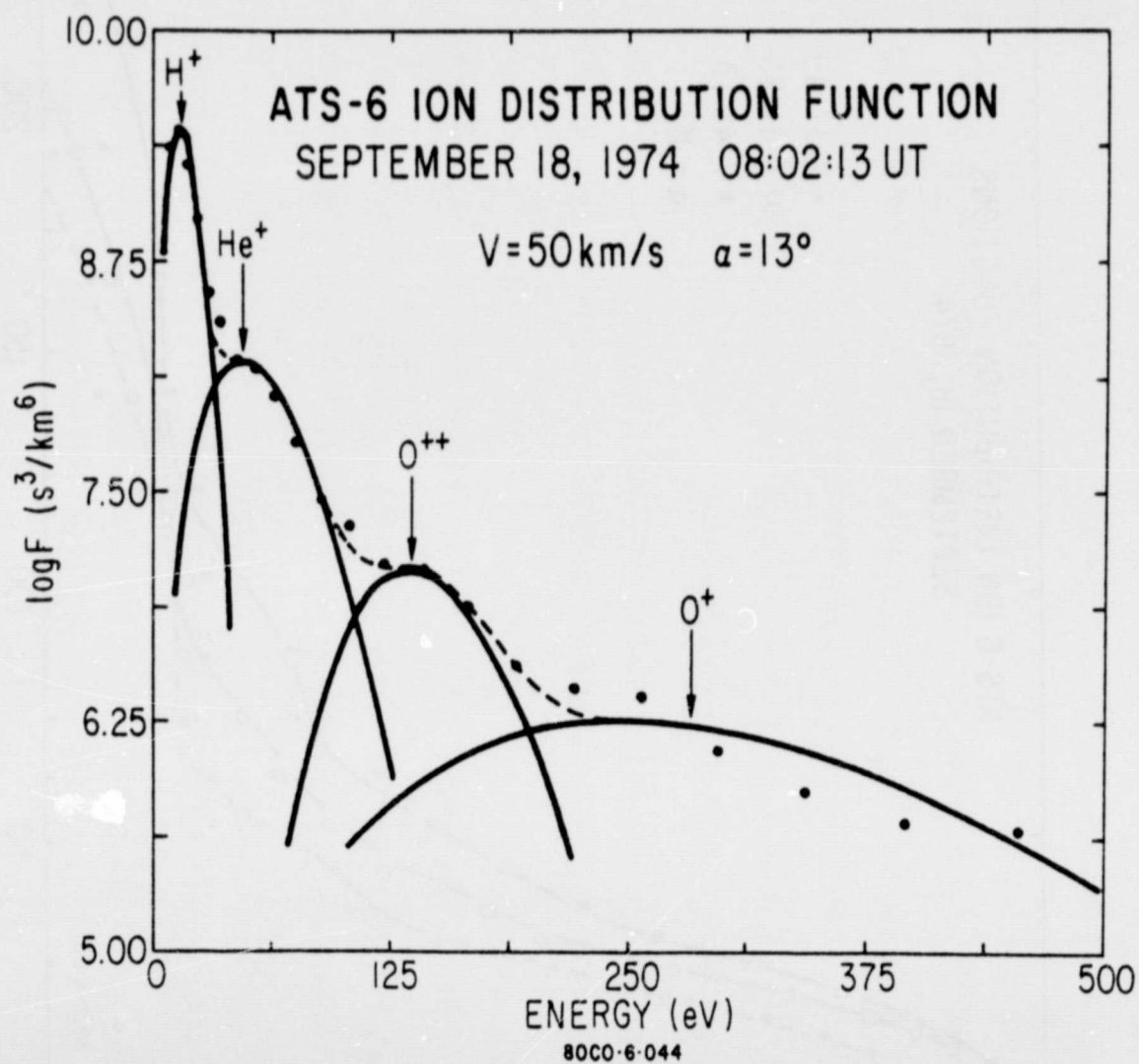


FIGURE 82

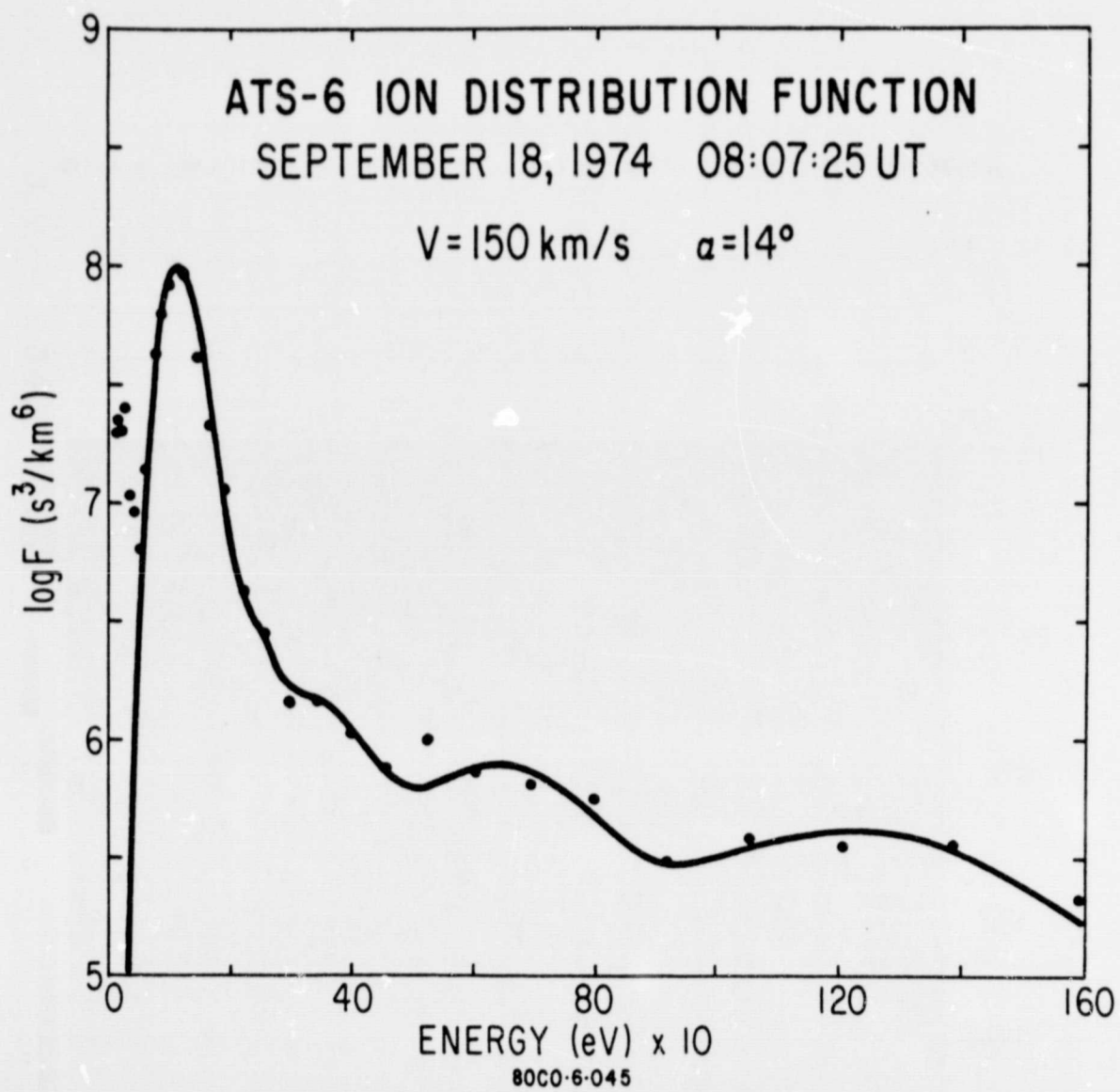


FIGURE 83

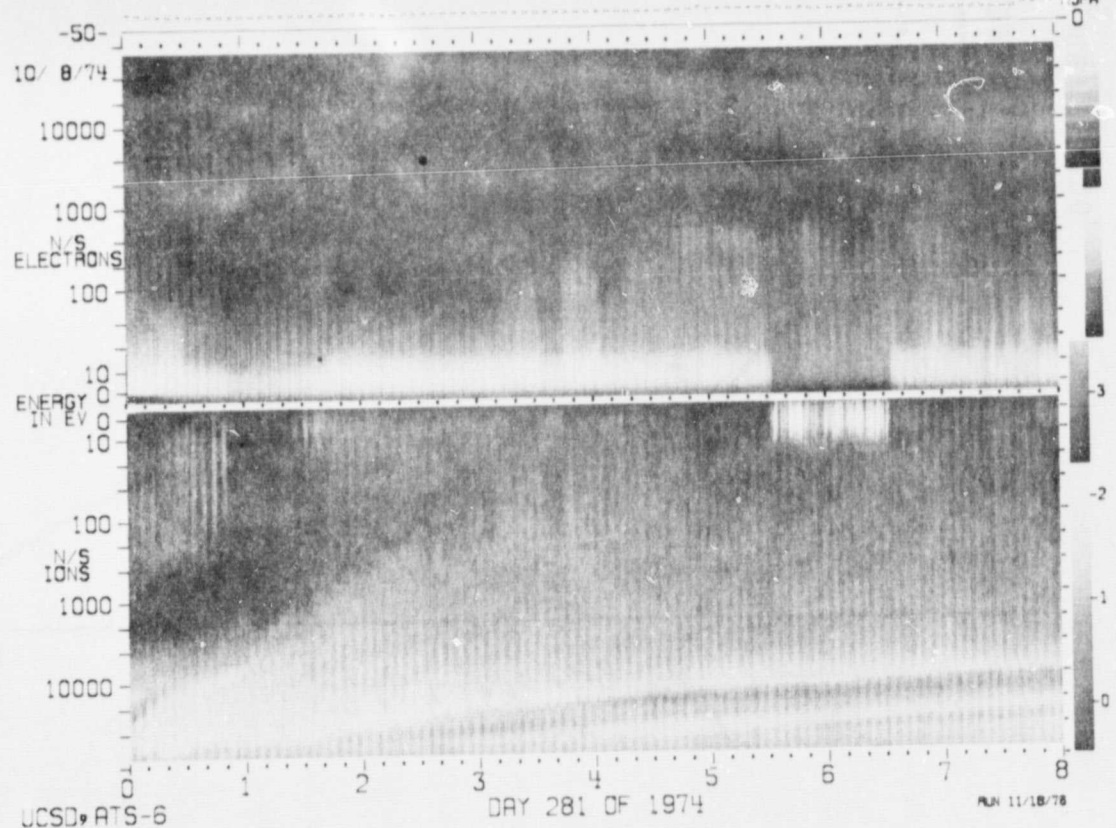


FIGURE 84

ORIGINAL PAGE IS
OF POOR QUALITY

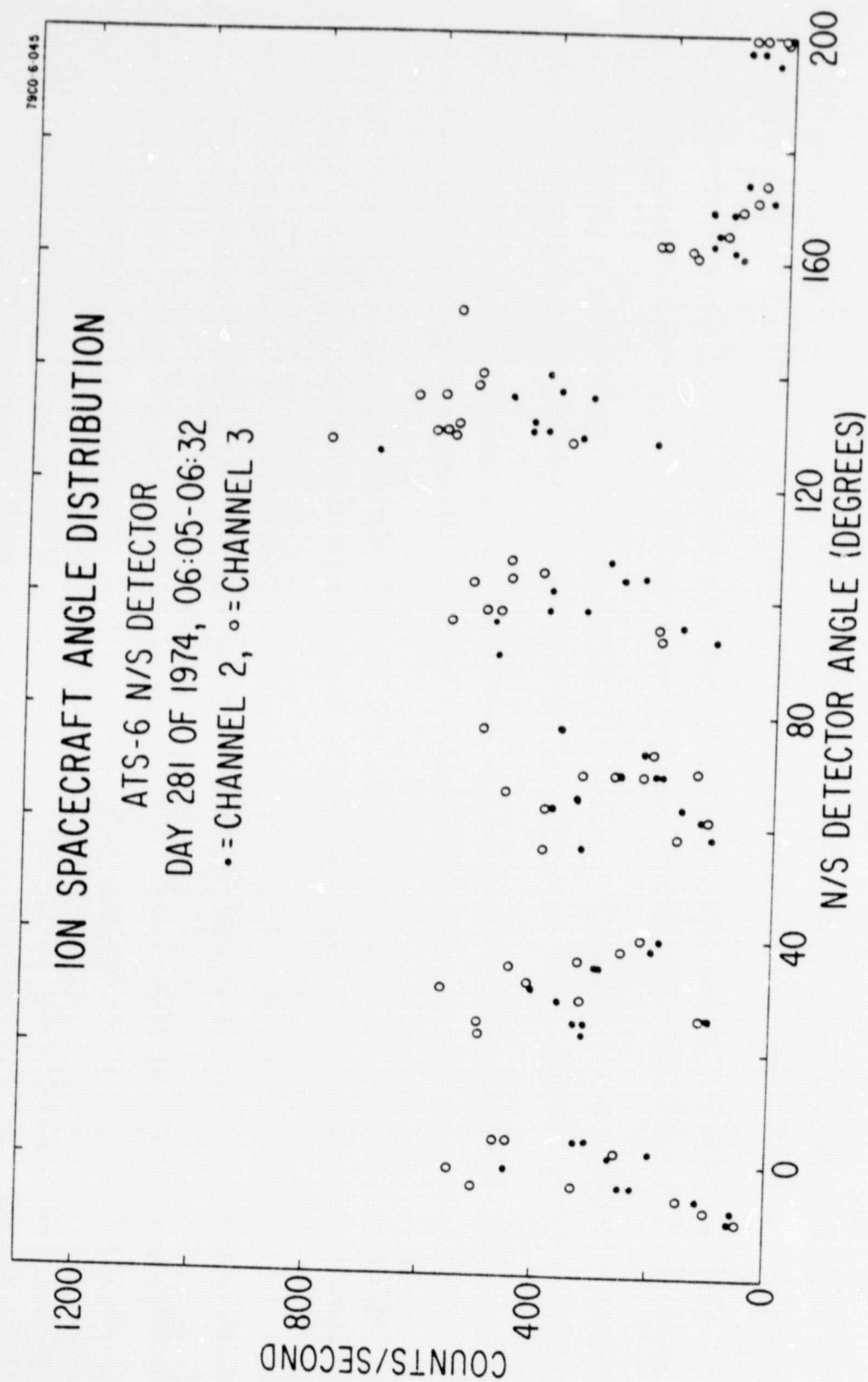


FIGURE 85